August 2020

Experimental Characterization and Biological Assessments of Polymeric Mesh Implants

Xinyue Lu
Clemson University, luxinyue2012@gmail.com

EXPERIMENTAL CHARACTERIZATION AND BIOLOGICAL ASSESSMENTS OF POLYMERIC MESH IMPLANTS

A Dissertation
Presented to
the Graduate School of
Clemson University

In Partial Fulfillment
of the Requirements for the Degree
Doctor of Philosophy
Bioengineering

---

by
Xinyue Lu
August 2020

Accepted by:
Dr. Melinda Harman, Committee Chair
Dr. B. Todd Heniford
Dr. Martin King
Dr. Jiro Nagatomi
Dr. Alexey Vertegel

ABSTRACT

In use since the 1960s, polypropylene (PP) biomaterials are common in commercially available hernia meshes due to their high tensile strength, good flexibility, and chemical resistance. The *in vivo* environment is highly variable, exposing mesh implants to oxidizing species and mechanical strains caused by normal healing, tissue integration, and the immediate and chronic inflammatory responses. As a result, changes in mesh implant materials can occur *in vivo*, including morphological changes, chemical changes and mechanical changes. The broad objective of this dissertation was to explore mechanisms of material changes in polymeric mesh implants after *in vivo* exposure using experimental characterization and biological assessments.

Biological assessments included mesh implants retrieved from patients after hernia repair surgery (mesh explants) to explore potential degradation mechanisms, specifically the impact of clinical characteristics for triggering material changes in pore size, surface chemistry, crystallinity and stiffness consistent with PP degradation. Development of an automated photogrammetric pore size and pore pattern recognition technique provided quantitative measurements of mesh pore size reduction and mesh contraction in mesh explants. Mesh class (pore size) was a factor affecting material changes in normalized crystallinity and reduced stiffness was observed in mesh explants from patients with infection.

Experimental characterization included two studies. *In vitro* simulated PP mesh degradation explored specific mechanisms that potentially contributed to PP material changes. The synergistic effect of reactive oxygen species (ROS) associated with chronic

inflammation/infection and mechanical strains on PP mesh degradation was experimentally simulated. PP mesh degradation was observed in simulated ROS solutions made of 1.63M hydrogen peroxide (H_2O_2)/ 0.05M cobalt chloride ($CoCl_2$), but the synergistic effect was not observed in the same simulated ROS solutions with applied low mechanical strains. A second experimental characterization involved surface modification of polymeric mesh implants for improved hernia mesh fixation with a hydrogel adhesive, called a "bio-adhesive mesh fixation system". The "bio-adhesive mesh fixation system" combined two patented technologies of poly-glycidyl methacrylate/human serum albumin (PGMA/HSA) grafting and a poloxamine hydrogel adhesive. Its experimental maximum adhesive strength was approximately 2 times higher than that of unmodified mesh, which was achieved by mechanical interlock of the hydrogel tissue adhesive into the PP mesh pores and chemical bonding of the grafted albumin.

Mesh explants retrieved from patients were valuable resources to explore material changes and the degradation mechanisms in highly variable *in vivo* conditions. Assessments of mesh explants were challenging due to the unknown mesh material properties before implantation and the uncontrolled nature of patient variables inherent in retrieval analysis. Compared to biological assessments, experimental characterization for *in vitro* simulation and mesh fixation system contributed to understanding mesh behavior in a controlled condition and building the foundation for predicting mesh behavior in physiological conditions.

DEDICATION

To my parents, Jianmin and Ruoqin who have constantly supported me with endless love and sacrifices since day one of my journey of education. To my husband, Chenchen, who brought me so much love, joy, understanding and encouragement during the journey of this accomplishment.

ACKNOWLEDGMENTS

I would like to acknowledge my advisor, Dr. Melinda Harman, for her guidance, mentorship and encouragement to me throughout the journey of my PhD research. I would like to acknowledge my committee, Dr. B.Todd Heniford, Dr. Martin King, Dr. Jiro Nagatomi, Dr. Alexey Vertegel for offering their expertise, guidance and collaboration throughout my research. I would like to acknowledge our collaborators Dr. Amy Lincourt and Dr. Vedra Augenstein at Atrium Health, and Dr. Igor Luzinov at Material Science and Engineering Department to coordinate with the projects. I would like to acknowledge the faculty and staff of Bioengineering Department, especially Chad McMahan, Dr. Agnes Nagy-Mehesz and Dr. Gulya Korneva to provide technical support. I would like to acknowledge staff at Material Science and Engineering Department, especially Kimberly Ivey to assist chemical analysis. I would like to acknowledge Dr. Astha Khanna's contribution to my first published journal article. I would like to acknowledge past and present members of RE-MED lab, especially Brittney Cotton, Mathew Stanford, Lexuan Sun, Megan Hanschke, Chad Eaton, Rithwik Jallepalli, Lauren Jackson and Nicole Meilinger in MeshWatch team to assist in data collection. I would like to acknowledge my family, friends, and roommates for their support and care through the journey.

TABLE OF CONTENTS

Page

Table of Contents (Continued)

Page

Table of Contents (Continued)

Page

LIST OF TABLES

List of Tables (Continued)

Table Page

LIST OF FIGURES

List of Figures (Continued)

Figure Page

List of Figures (Continued)

Figure Page

PREFACE

Broad Objective and Specific Aims

Surgical mesh is a medical device consisting of implantable polymeric materials. It is commonly used for surgical repair of abdominal hernia, which is a widespread health concern that occur secondary to weakened or damaged abdominal wall tissues. In use since the 1960s, polypropylene (PP) biomaterials are common in commercially available hernia meshes due to their high tensile strength, good flexibility, and chemical resistance. However, changes in mesh implant materials can occur *in vivo*, including morphological changes, chemical changes and mechanical changes. The *in vivo* environment is highly variable, exposing mesh implants to oxidizing species and applied mechanical strains caused by normal healing, tissue integration, and the immediate and chronic inflammatory responses. Mesh implants retrieved from patients after hernia repair surgery (hereafter, mesh explants) provide a unique source for investigating mesh material changes, specifically pore size, surface chemistry, crystallinity and stiffness. However, few studies have explored mechanisms that potentially contribute to material changes *in vivo*.

The broad objective of this dissertation is to explore mechanisms of material changes in polymeric mesh implants after *in vivo* exposure using experimental characterization and biological assessments. The following aims are addressed:

Aim 1. Determine material changes of polymeric mesh explants and explore the mechanisms of material changes related to clinical factors. It is hypothesized that 1)

mesh explants have significant material changes compared to mesh implants before implantation; 2) mesh implants with small pore size, retrieved from infected patients, or implanted in intra-peritoneal location have significant material changes compared to mesh implants with large pore size, retrieved from non-infected patients, or implanted in extra-peritoneal location.

Aim 2. Determine the effect of simulated oxidizing agents and applied mechanical strains on initiating polypropylene mesh degradation. It is hypothesized that the synergistic effect of oxidizing agents and mechanical strains significantly induces PP mesh degradation than the individual factors alone.

Aim 3. Determine the effect of surface modification of polymeric mesh implants on fixation and compatibility with a hydrogel adhesive. It is hypothesized that the adhesive strength between the surface modified polymeric mesh implants and hydrogel adhesive is significantly higher than the adhesive strength between unmodified polymeric mesh implants and hydrogel adhesive.

Aim 1 and Aim 2 address gaps for describing specific mechanisms that potentially contribute to mesh material changes after *in vivo* exposure using mesh explants and *in vitro* simulation. Aim 3 addresses a new technology combining two patented technologies that improves clinical outcomes of hernia mesh fixation.

List of Studies

Four studies (Figure P.1) are undertaken to address the three specific aims:

Chapter 2, titled "Pore Size Analysis of Explanted Surgical Mesh Using Photogrammetric Method" will address Aim 1 by comparing explanted mesh and pristine

mesh and relating it to the pore pattern. It describes development of a photogrammetric method using image capture, image processing and image analysis to classify pore pattern and measure pore size and evaluates changes in pore size after physiological loading.

Chapter 3, titled "Analyzing Material Changes Consistent with Degradation of Explanted Surgical Mesh Related to Clinical Characteristics" will address Aim 1 by analyzing material changes of explanted PP mesh that center on potential degradation mechanisms and investigating clinical characteristics that may trigger the material changes consistent with PP degradation.

Chapter 4, titled "Understanding Mechanisms of Polypropylene Hernia Mesh Degradation Using Experimental Simulations" will address Aim 2 by defining a physiological continuum of reactive oxygen species (ROS) concentrations associated with chronic inflammation/infection and estimating the synergistic impact of ROS and mechanical strains on PP mesh degradation using *in vitro* simulation.

Chapter 5, titled "Surface Modification of Polypropylene Surgical Meshes for Improving Adhesion with Poloxamine Hydrogel Adhesive" will address Aim 3 by comparing two different surface modifications of PP mesh to improve the adhesive strength with poloxamine hydrogel adhesive by achieving both mechanical interlock and covalent bonds.

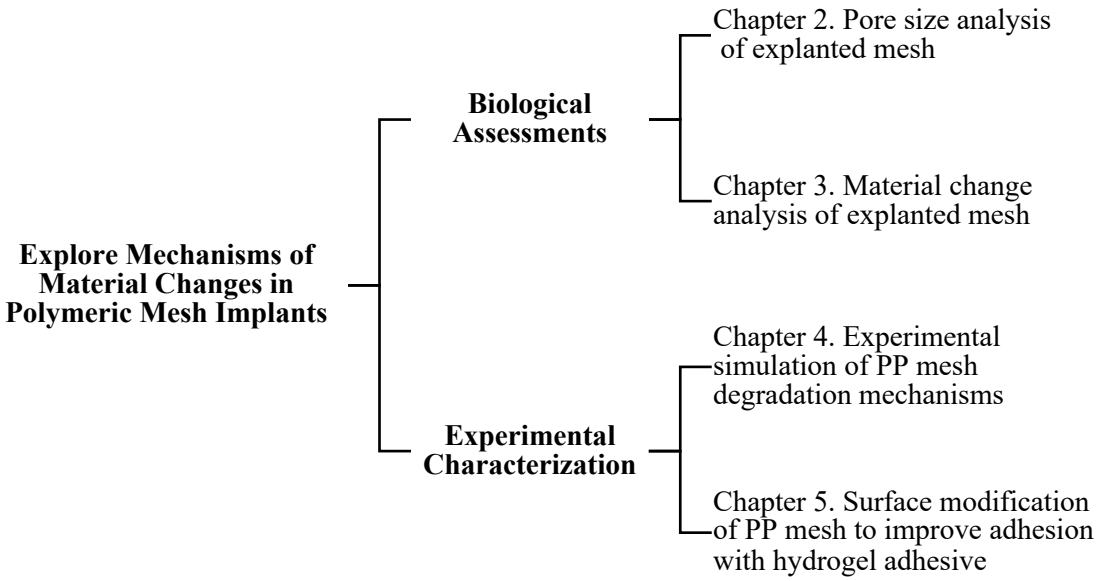

Figure P. 1 Organization of dissertation and relationship with each chapter.

CHAPTER ONE

MESH REGISTRY

Mesh Types in Mesh Registry

Hernia meshes in this dissertation were collected by a surgical team (Atrium Health, Charlotte, NC) through an established registry of mesh explants (MeshWatch) using a protocol approved by the Clemson University Institutional Review Board (IRB2014-161) (1). Meshes from consecutive patients undergoing revision hernia surgery from 2006 to 2014 were archived and stored in 10% formalin until analysis (2). Meshes from 2014 to 2018 were archived and fresh-frozen at -80° C until analysis.

To date, there are 102 formalin fixed and 164 fresh frozen mesh explants of various types in the registry along with documentation of basic patient demographics and clinical history abstracted from available records. Details of mesh structure and type were cataloged for each explanted mesh using a pictorial "MeshWatch" atlas of known mesh types and knitted patterns characterized using gross assessment, optical microscopy, and digital imaging, as described in Chapter 2. Explanted mesh samples were biopsied and cleaned using defined tissue digestion methods to expose the mesh structure for material change characterization, as described in Chapter 3.

The MeshWatch Atlas defines 9 known types of hernia meshes, including Composix™ E/X, Composix® Kugel®, Composix™ L/P, C -QUR® , Physiomesh™, Prolene® Soft, Ultrapro®, Ventralex™ and Ventralight™ (Table 1.1). The expanded polytetrafluoroethylene (ePTFE) components of Composix™ E/X, Composix® Kugel®,

Composix™ L/P and Ventralex™ were removed for experimental characterization of material properties, as described in Chapter 2, Chapter 3, Chapter 4 and Chapter 5. The absorbable components of C-QUR®, Physiomesh™ and Ventralight™ were washed by soaking in 0.01 M phosphate buffer solutions (PBS) at 37 °C on an orbital shaker for 12 hours and rinsed by Millipore water, but they were unable to be completely removed. Pristine meshes in this dissertation are unused meshes removed from original packages within shelf life except Composix® Kugel®, which was recalled in 2006.

Mesh Classification

Most surgical meshes are manufactured using warp-knitting techniques to provide the flexibility and structural stability from the interlacing filament loops (3, 4). The loop structure patterns are normally repeatable because of the warp knitting machine, which makes identical lapping movements of the mesh filaments through guide holes attached to the same guide bar (5). The spaces between mesh filaments are mesh pores, allowing tissue ingrowth for hernia repair. Mesh pore size can be measured using image capture, image processing and image analysis to classify pore pattern and measure pore size, as described in Chapter 2.

Meshes in MeshWatch are classified as Class I (large pore mesh with porosity > 60% or an effective porosity > 0%), Class II (small pore mesh with porosity < 60% and without any effective porosity), and Class III (mesh with additional features) according to textile structures and a published classification scheme (6) (Table 1.1). The effective porosity is the pore size allowing tissue ingrowth instead of "bridging", which occurs when the small pores are completely filled with inflammatory infiltrates or fibrotic scars

(7-10). The minimum pore size for effective porosity is 1 mm for PP mesh (11). Meshes with large pores facilitate tissue ingrowth (10), while meshes with small pores induce greater inflammatory response and increase abdominal wall stiffness (7-10). PP meshes combined with additional features are capable of reducing complications, such as tissue adhesion, foreign body reaction, chronic pain and infection.

Mesh Crystallinity

PP is a semi-crystalline polymer with crystalline and amorphous regions. Its crystallinity affects mechanical (12) and chemical properties (13). PP having increased crystallinity results in increased stiffness (12). However, PP with higher crystallinity has reduced resistance to free radicals than lower crystallinity in case of gamma radiation (12). These radicals are trapped in the crystalline regions, resulting in chain scission or crosslinking and leading to increased brittleness (12).

PP mesh crystallinity can be measured using differential scanning calorimetry (DSC), as described in Chapter 3 and Chapter 4. The crystallinity of the pristine PP meshes in MeshWatch ranges from 41.9% to 48.1% (Table 1.2), compared to referenced PP meshes with crystallinity of 40% to 57% (14-17). Meshes with absorbable layers are not included in Table 1.2. The crystallinity of pristine cleaning controls ranges from 41.9% to 50.0%, as described in in Chapter 3. The crystalline regions disappear at the melting point, determined by the amount of crystallinity. The melting temperature of the pristine PP meshes in MeshWatch ranges from 164.5°C to 169.9 °C (Table 1.2), compared to a perfect isotactic PP with theoretical melting point of 171 °C (12). PP

without additives and with lower crystallinity leads to decreased melting temperature (T_m) (12). The crystallinity and T_m can be altered for PP with additives (18, 19).

Mesh Stiffness

Mesh stiffness is related with clinical outcomes. Meshes with low stiffness can result in mesh failure due to inadequate mechanical support (20) and difficulty in handling during surgery due to excessive flexibility (21). Meshes with high stiffness lead to clinical complications, such as postoperative pain and discomfort (20).

Mesh stiffness can be measured using uniaxial tensile testing (22), biaxial tensile testing (23-26) or ball burst testing (22). Biaxial tensile testing was used in this dissertation using a biaxial tensile tester equipped with orthogonal 23N load cells and a high-resolution CCD imaging system for image-based strain measurement (BioTester, CellScale, Ontario, Canada), as described in Chapter 3 and Chapter 4. Mesh pore size deformation can be minimized in biaxial tensile testing (27), achieving higher measured mesh stiffness (25), compared to uniaxial tensile testing (20, 28, 29). Mesh anisotropy can be evaluated using biaxial tensile testing, compared to ball burst testing (17, 25).

The stiffness of pristine PP meshes in MeshWatch ranges from 149.0 N/cm to 300.4 N/cm in longitudinal direction (S_y) and from 79.0 N/cm to 245.4 N/cm in transverse direction (S_x) (Appendix B) (Table 1.3), compared to referenced PP mesh stiffness ranging from 75.7 N/cm (25) to 191.1 N/cm (24) in S_y and 37.5 N/cm (25) to 177.8 N/cm (25) in S_x. Ventralex™ was not included in Table 1.3 due to the limited mesh dimension available for testing. PP mesh stiffness is much lower than PP fiber stiffness, which is approximately 50,000 to 110, 000 N/cm based on estimates using the surgical

mesh thickness at 0.5 mm (22, 30) and the elastic modulus of PP fiber ranging from 10 to 22 GPa (13). The difference is induced by the loop structures of warp-knitted mesh (31).

Table 1. 1. Mesh structure information

Brand	Material	Structures	Mesh Class	Porosity/Pore size	Ref
Composix™ E/X	PP sewn to ePTFE film	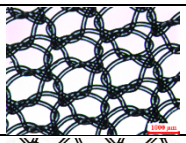	III	0.43 mm^2	(22)
Composix® Kugel®	PP sewn to ePTFE film	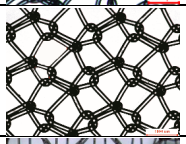	III	57%	(32)
Composix™ L/P	PP sewn to ePTFE film	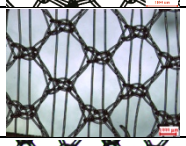	III	64%	(32)
C -QUR®	PP with omega 3 fatty acid layer	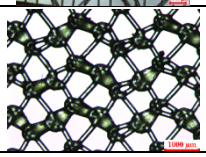	III	0.33 mm^2	(22)
Physiomesh™	PP/polyglecaprone-25 (PG-25)/ polydioxanone (PDS)	Old structure: 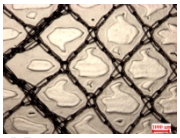 New structure: 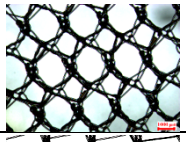	III	6.50 mm^2 63%	(33) Measured as in Chapter 2
Prolene® Soft	PP	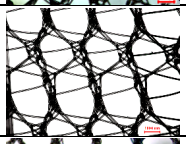	I	67%	(34)
Ultrapro®	PP/PG-25	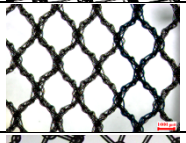	I	67%	(6)
Ventralex™	PP sewn to ePTFE film	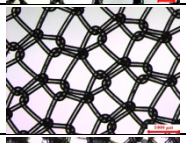	III	57%	Measured as in Chapter 2
Ventralight™	PP/polyglycolic acid (PGA)	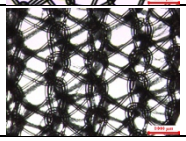	III	43%	(34)

Table 1. 2. Mesh thermal properties

Brand	Measured Crystallinity (%)	Referenced Crystallinity (%)	Ref	Measured T_m (°C)	Referenced T_m (°C)	Ref
Composix™ E/X	46.2	47.0	(14)	165.5	166	(35)
Composix® Kugel®	41.9	-	-	166.9	-	-
Composix™ L/P	48.1	-	-	169.2	-	-
Prolene® Soft	46.9	-	-	168.4	170.2	(36)
Ultrapro®	44.3	42.1	(14)	168.1	166	(14)
Ventralex™	45.0	-	-	164.5	-	-

Table 1. 3. Mesh stiffness

Brand	Measured S_y (N/cm)	Referenced S_y (N/cm)	Ref	Measured S_x (N/cm)	Referenced S_x (N/cm)	Ref
Composix™ E/X	118.7 ± 22.9	-	-	79.0 ± 18.3	-	-
Composix® Kugel®	187.8	-	-	165.9	-	-
Composix™ L/P	194.7 ± 15.1	-	-	122.1 ± 19.1	-	-
C -QUR®	178.7 ± 6.6	177.00 ± 4.94	(25)	180.9 ± 2.8	177.78 ± 14.04	(25)
Physiomesh™ (new structure)	149.0 ± 10.2	-	-	142.4 ± 16.9	-	-
Physiomesh™ (old structure)	-	168.91 ± 26.91	(25)	-	151.62 ± 26.57	(25)
Prolene® Soft	153.8 ± 4.8	-	-	113.0 ± 9.5	-	-
Ultrapro®	152.7 ± 9.2	98.63 ± 6.13 171.2 ± 78.9	(25) (24)	82.2 ± 5.3	53.01 ± 5.41 79.6 ± 11.4	(25) (24)
Ventralight™	300.4 ± 37.1	123.57 ± 10.04	(25)	245.4 ± 22.9	50.82 ± 4.61	(25)

Factors Affecting Mesh Properties in the MeshWatch Registry

Comparing explanted mesh to pristine mesh is challenging due to the elapsed time between implantation and explantation. The *in vivo* duration averaged 2.8 ± 2.8 years (range: 0.3 to 13 years) for mesh explants included in this dissertation. Mesh implant products are ever-changing, and several factors affecting mesh properties are noted, which must be kept in mind for all explanted and pristine mesh comparisons in this dissertation.

Mesh Recalls

Mesh recalls lead manufacturers to modify products, which contributes to changes in mesh properties, such as mesh structures, mesh chemistry and mesh mechanics. Composix® Kugel® was recalled in 2006 and Physiomesh™ Flexible Composite Mesh was recalled in 2016. Composix® Kugel® was not available in the market after 2006 and the mesh design of Physiomesh™ Flexible Composite Mesh was changed after the recall. All Composix® Kugel® used as pristine controls in this dissertation have been expired for at least 10 years. Oxidation may occur on the expired unused mesh due to the long-time exposure to air. All pristine Physiomesh™ meshes within shelf life and used as pristine controls in this dissertation were manufactured in the new mesh structure after the recall (Table 1.1) with different mechanical properties (Table 1.3), which was different from the old structures of most explanted Physiomesh™ retrieved from patients. All explanted Physiomesh™ meshes were implanted in patients no later than 2016, as described in Chapter 3, adding to the differences in material properties between explanted meshes and pristine controls.

Absorbable Components in Class III Mesh

The *in vivo* resorption of absorbable components changes mesh properties, such as mesh structure and mesh stiffness (21, 34, 37). The absorbance of PGA changes pore size of Ventralight™ (Figure 1.1). The absorbance of PDS/oxidized cellulose in Proceed® results in same mesh structure and same chemistry as Prolene® Soft (Figure 1.1), increasing the difficulty of identifying mesh types of explanted mesh retrieved from

patients (16). The *in vivo* resorption of absorbable components leads to notable reduction in mesh stiffness (21, 34, 37).

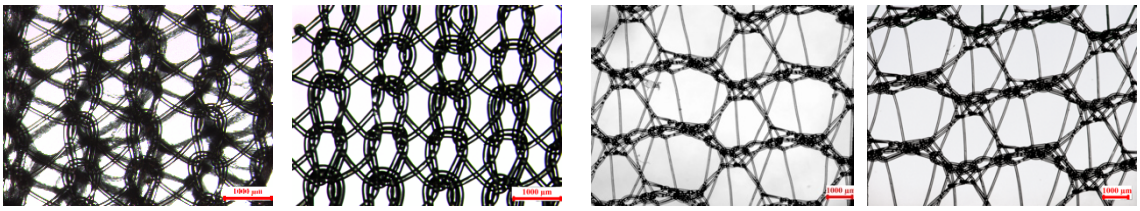

Pristine Ventralight™ Explanted Ventralight™ Pristine Proceed® Pristine Prolene® Soft

Figure 1. 1. Mesh before and after resorption of absorbable components. Different pore size between pristine Ventralight™ and explanted Ventralight™; same mesh structure between Proceed® and Prolene® Soft. Scale bar: 1000µm.

Manufactured Year

Even though a mesh type is assigned the same brand name and is considered the same mesh type, manufacturing in different years can result in different material properties, such as different polymer chemistry and mesh stiffness. As documented in detail in Chapter 3 and Chapter 4 of this dissertation, the measured crystallinity of unused Composix™ E/X manufactured in different years (expiration date on the packages: 2013 – 2019) ranges from 43.1% to 52.4% (Figure 1.2). The measured biaxial tensile stiffness for pristine Ultrapro® (expiration date on package: 2019) is 152.7± 9.2 N/cm in S_y and 82.2 ± 5.3 N/cm in S_x (Figure 1.3), compared to the measured stiffness for expired Ultrapro® (expiration date on package: 2015) of 130.6 ± 9.8 N/cm and 64.7 ± 10.7 N/cm. Those values differ from previous studies (Table 1.3) by Deeken et al. (25) and Cordero et al. (24) using similar testing methods.

In this dissertation, all explanted meshes were originally implanted in patients between 2001 to 2016 but all pristine meshes were manufactured between 2015 to 2019,

possibly leading to different crystallinity and stiffness between pristine mesh implanted in patients before implantation and pristine controls for comparison. The pristine meshes used in this dissertation were manufactured in different years according to the study duration of each chapter: Chapter 2 was accomplished between 2015 to 2017; Chapter 3 was accomplished between 2017 to 2019; Chapter 4 was accomplished in 2019; and Chapter 5 was accomplished between 2016 to 2018.

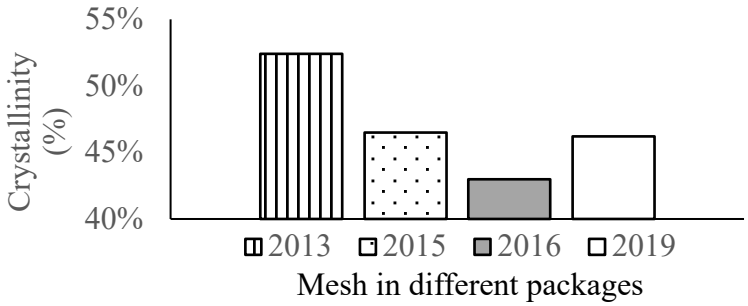

Figure 1. 2. Measured crystallinity of Composix™ E/X manufactured from different years with testing methods documented in detail in Chapter 3 and Chapter 4. Meshes were identified using the expiration date on the packages.

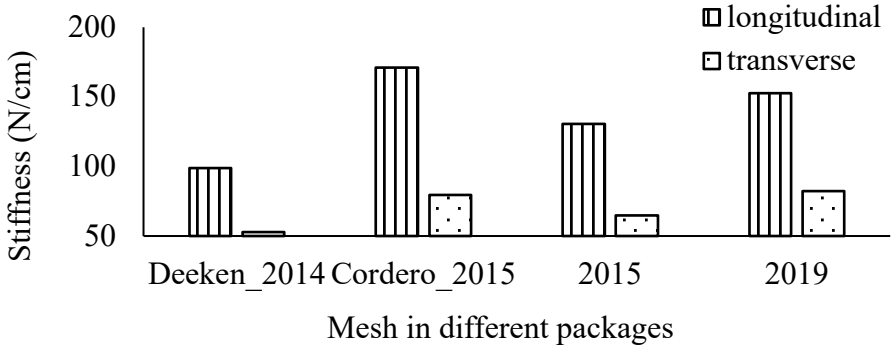

Figure 1. 3. Measured and referenced biaxial stiffness of Ultrapro® manufactured from different years with testing methods documented in detail in Chapter 3 and Chapter 4. Deeken_2014 and Cordero_2015: values from references (25) (24). Measured meshes were identified using the expiration date on the packages.

References

1. Burns-Heffner C. Development of explant registry and mechanical testing of pristine and explanted surgical mesh [dissertation]. ProQuest Dissertations Publishing; 2014.

2. Casey EM. Physical characterization of surgical mesh after function in hernia repair [dissertation]. ProQuest Dissertations Publishing; 2015.

3. Zhu L, Schuster P, Klinge U. Mesh implants: An overview of crucial mesh parameters. World J Gastrointest Surg. 2015;7(10):226.

4. Jiang GM, Miao XH, Lee D. Process of warp knitting mesh for hernia repair and its mechanical properties. Fibres Text East Eur. 2005;13(3):44-6.

5. Spencer DJ. Knitting technology: a comprehensive handbook and practical guide, 3rd ed. Cambridge, UK: Woodhead Publishing; 2001.

6. Klinge U, Klosterhalfen B. Modified classification of surgical meshes for hernia repair based on the analyses of 1,000 explanted meshes. Hernia. 2012;16(3):251-8.

7. Klinge U, Klosterhalfen B, Birkenhauer V, Junge K, Conze J, Schumpelick V. Impact of polymer pore size on the interface scar formation in a rat model. J Surg Res. 2002;103(2):208-14.

8. Klinge U, Dietz U, Fet N, Klosterhalfen B. Characterization of the cellular infiltrate in the foreign body granuloma of textile meshes with its impact on collagen deposition. Hernia. 2014;18(4):571-8.

9. Sanders D, Lambie J, Bond P, Moate R, Steer JA. An *in vitro* study assessing the effect of mesh morphology and suture fixation on bacterial adherence. Hernia. 2013;17(6):779-89.

10. Junge K, Binnebösel M, von Trotha KT, Rosch R, Klinge U, P. Neumann U, Lynen Jansen P. Mesh biocompatibility: effects of cellular inflammation and tissue remodeling. Langenbeck's Arch. Surg. 2012;397(2):255-70.

11. Conze J, Junge K, Weiß C, Anurov M, Oettinger A, Klinge U, Schumpelick V. New polymer for intra-abdominal meshes - PVDF copolymer. J Biomed Mater Res B. 2008;87(2):321-8.

12. Maier C, Calafut T. Polypropylene: the definitive user's guide and databook. Norwich, NY: Plastics Design Library; 1998.

13. Richaud E, Verdu J, Fayolle B. Tensile properties of polypropylene fibres. Woodhead Publishing Series; 2009. p. 315-31.

14. Gil D. Naturally Derived Anti-Inflammatory and Antibacterial Coatings for Surgical Implants [dissertation]. ProQuest Dissertations Publishing; 2017.

15. Afonso JS, Jorge R, Martins PS, Soldi MD, Alves OL, Patricio B, Mascarenhas T, Sartori MG, Girao MJ. Structural and thermal properties of polypropylene mesh used in treatment of stress urinary incontinence. Acta Bioeng Biomech. 2009;11(3):27-33.

16. Soares BM, Guidoin RG, Marois Y, Martin L, King MW, Laroche G, Zhang Z, Charara J, Girard JF. *In vivo* characterization of a fluoropassivated gelatin-impregnated polyester mesh for hernia repair. J Biomed Mater Res. 1996;32(3):293-305.

17. Schoen FJ, Lemons JE, Ratner BD, Hoffman AS. Biomaterials science: an introduction to materials in medicine. Burlington: Academic Press; 2013.

18. Liao J, Brosse N, Pizzi A, Hoppe S, Xi X, Zhou X. Polypropylene blend with polyphenols through dynamic vulcanization: mechanical, rheological, crystalline, thermal, and UV protective property. Polymers. 2019;11(7):1108.

19. Mittal V. Crystallinity, mechanical property and oxygen permeability of polypropylene: Effect of processing conditions, nucleating agent and compatibilizer. J Thermoplast. Compos. Mater. 2013;26(10):1407-23.

20. Maurer MM, Röhrnbauer B, Feola A, Deprest J, Mazza E. Mechanical biocompatibility of prosthetic meshes: A comprehensive protocol for mechanical characterization. J Mech Behav Biomed. 2014;40:42-58.

21. Cobb WS, Kercher KW, Heniford BT. The argument for lightweight polypropylene mesh in hernia repair. Surg Innov. 2005;12(1):63-9.

22. Deeken CR, Abdo MS, Frisella MM, Matthews BD. Physicomechanical evaluation of absorbable and nonabsorbable barrier composite meshes for laparoscopic ventral hernia repair. Surg Endosc. 2011;25(5):1541-52.

23. Sahoo S, DeLozier KR, Erdemir A, Derwin KA. Clinically relevant mechanical testing of hernia graft constructs. J Mech Behav Biomed. 2015;41:177-88.

24. Cordero A, Hernández-Gascón B, Pascual G, Bellón JM, Calvo B, Peña E. Biaxial mechanical evaluation of absorbable and nonabsorbable synthetic surgical meshes used for hernia repair: physiological loads modify anisotropy response. Ann Biomed Eng. 2016;44(7):2181-8.

25. Deeken CR, Thompson J,Dominic M., Castile RM, Lake SP. Biaxial analysis of synthetic scaffolds for hernia repair demonstrates variability in mechanical anisotropy, non-linearity and hysteresis. J Mech Behav Biomed. 2014;38:6-16.

26. Wolf MT, Carruthers CA, Dearth CL, Crapo PM, Huber A, Burnsed OA, Londono R, Johnson SA, Daly KA, Stahl EC, Freund JM, Medberry CJ, Carey LE, Nieponice A, Amoroso NJ, Badylak SF. Polypropylene surgical mesh coated with extracellular matrix mitigates the host foreign body response. J Biomed Mater Res A. 2014;102(1):234-46.

27. Barone WR, PhD, Moalli, Pamela A., MD, PhD, Abramowitch SD, PhD. Textile properties of synthetic prolapse mesh in response to uniaxial loading. Obstet Gynecol. 2016;215(3):326.e1,326.e9.

28. Saberski ER, Saberski ER, Orenstein SB, Orenstein SB, Novitsky YW, Novitsky YW. Anisotropic evaluation of synthetic surgical meshes. Hernia. 2011;15(1):47-52.

29. Pott PP, Schwarz Markus L. R., Gundling R, Nowak K, Hohenberger P, Roessner ED. Mechanical properties of mesh materials used for hernia repair and soft tissue augmentation. Plos One. 2012; 7(10): e46978.

30. Deeken CR, Lake SP. Mechanical properties of the abdominal wall and biomaterials utilized for hernia repair. J Mech Behav Biomed. 2017;74:411-27.

31. Miao L, Wang F, Wang L, Zou T, Brochu G, Guidoin R. Physical characteristics of medical textile prostheses designed for hernia repair: a comprehensive analysis of select commercial devices. Materials. 2015;8(12):8148-68.

32. Lu X, Khanna A, Luzinov I, Nagatomi J, Harman MK. Surface modification of polypropylene surgical meshes for improving adhesion with poloxamine hydrogel adhesive. J Biomed Mater Res B. 2019;107(4): 1047-1055.

33. Jenkins J, Lu X, Hanschke M, Harman M. Assessment of a tissue removal method and its impact on the pore structure of hernia mesh. 2016 July (Clemson University summer 2016 undergraduate research symposium).

34. Ethicon UL. Ethicon tissue-separating mesh: a comparative guide. https://www.jnjmedicaldevices.com/sites/default/files/user_uploaded_assets/pdf_assets/2019-10/PROCEED-Surgical-Mesh-Comparative-Guide-063157-180511.pdf: 2018.

35. Costello CR, Bachman SL, Ramshaw BJ, Grant SA. Materials characterization of explanted polypropylene hernia meshes. J Biomed Mater Res B. 2007;83B(1):44-9.

36. Costello CR, Bachman SL, Grant SA, Cleveland DS, Loy TS, Ramshaw BJ. Characterization of heavyweight and lightweight polypropylene prosthetic mesh explants from a single patient. Surg Innov. 2007;14(3):168-76.

37. Cobb WS, Burns JM, Peindl RD, Carbonell AM, Matthews BD, Kercher KW, Heniford BT. Textile analysis of heavy weight, mid-weight, and light weight polypropylene mesh in a porcine ventral hernia model. J Surg Res. 2006;136(1):1-7.

CHAPTER TWO

PORE SIZE ANALYSIS OF EXPLANTED SURGICAL MESH USING PHOTOGRAMMETRIC METHOD

Introduction

Synthetic surgical mesh is a type of knitted textile polymer material implanted within the body to reinforce body tissues, such as the abdominal wall. Annual global use exceeds 20 million hernia repairs utilizing surgical mesh because of its efficacy in clinical outcomes (1). However, mesh gross contraction and other complications can be caused by tissue integration and by a foreign body response occurring around the mesh (2-5). In addition to the mesh material and mechanical properties, these factors also are influenced by structural characteristics of the mesh, such as pore size. Polypropylene (PP) meshes with small pores can induce a greater inflammatory response and fibrotic tissue adhesion, compared to meshes with large pores (6-8). Therefore, it is clinically relevant to discriminate among pore size in surgical mesh.

Most surgical meshes are manufactured using warp-knitting techniques to provide the flexibility and structural stability from the interlacing filament loops (9, 10). These surgical meshes differ from woven fabrics and weft knitted fabrics, which are formed by crossing of weft yarns and warp yarns and loops in a horizontal direction using a single yarn system, respectively. In warp-knitted meshes, the loop structure patterns are normally repeatable because of the identical lapping movements of the mesh filaments through guide holes attached to the same guide bar, contributing to the characteristic "pore pattern" (11). Pore pattern includes different pore sizes distributed throughout the

mesh (Figure 2.1). Specifically, pore size in warp-knitted mesh is determined by the filament diameter, stitch density (number of stitches/cm), and loop structure, as well as post-treatment processes (12). Altering these parameters results in a varied mesh structure with a repeating pattern of different sized pores (Figure 2.1). Smaller diameter and stitch density can increase maximum pore size (12). Different loop structures result in different pore sizes regardless of the same lapping movements (Figure 2.1).

Linking the analysis of pore size to textile structure is important for understanding the mechanical behavior of mesh, as pore size changes under tensile loads (13, 14). Applying uniaxial tension to a warp-knitted mesh will initially cause movement of the loop knots and straightening of the curved loop filaments along the uniaxial direction, followed by stretching of loop filaments and eventually filament failure (Figure 2.2) (12, 15, 16). For these reasons, changes in pore size in implanted mesh are likely due to mechanical loading during surgical handling and contraction of abdominal wall muscles or other tissues adjacent to the mesh. Evaluation of pore size in different commercially available meshes has not included meshes explanted from patients (12, 17). Analysis of explanted mesh provides a unique opportunity to evaluate pore size after exposure to physiological conditions in humans.

The overall purpose of this study was to evaluate changes in pore size after physiological loading by comparing explanted mesh and pristine mesh and relating it to the pore pattern. This was accomplished using a new automated digital photogrammetric method to measure pore size based on the pore pattern of two different types of

commercially available PP surgical meshes. It was hypothesized that pore sizes in explanted meshes and pristine meshes were similar.

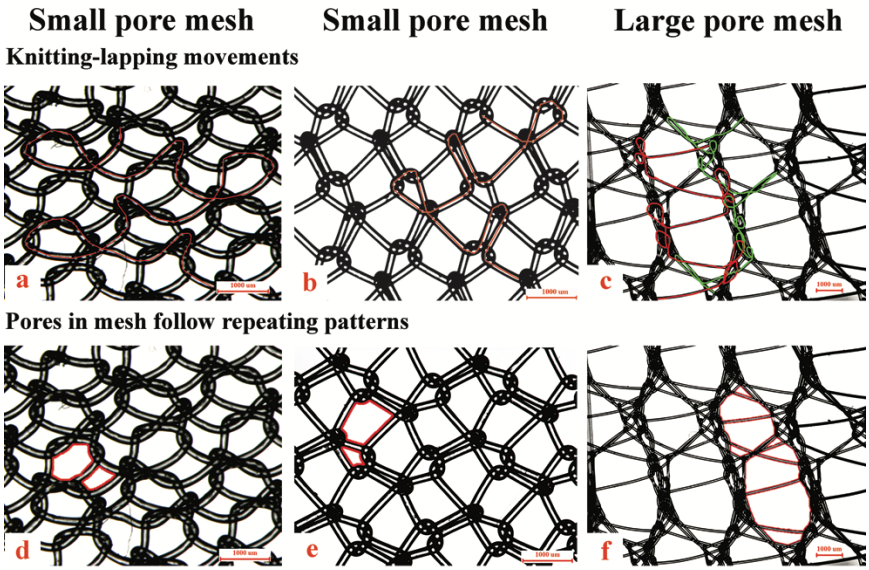

Figure 2. 1. Mesh knitting-lapping movements and pore patterns.
(a-c): warp-knitted mesh with knitting-lapping movements (red line and green line). a&b: mesh with same knitting-lapping movements may have different pore sizes. (d-f): pores in mesh follow repeating patterns (pores with red outlines). Scale bar: 1000 μm.

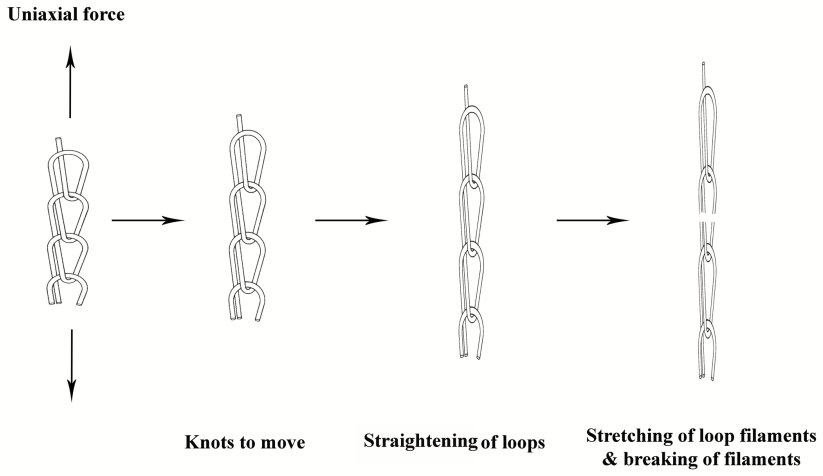

Figure 2. 2. Mechanical behavior of loops under uniaxial force.
Along the uniaxial direction, loop knots start to move and the curved loop filaments are straightened, followed by stretching of loop filaments and eventually filament failure. Figure is adapted from reference (11).

Materials

Two mesh types were selected from an IRB-approved registry of mesh explants: one standard weight small pore mesh and one light weight large pore mesh (Table 2.1) (18, 19). Seventeen small pore meshes and eight large pore meshes were acquired after an average implantation time of 28 ± 19 months and 23 ± 27 months, respectively (Table 2.2). Meshes were retrieved from various locations on the abdominal wall (e.g. upper or lower quadrant and umbilical region). Reasons for mesh removal included hernia recurrence, infection, chronic inflammation, seroma, incarcerated hernia and bowel obstruction (Appendix A). Tissues remaining on the mesh were digested by immersing in 8.25% hypochlorite solution at 37°C for at least 2 hours depending on the amount of tissue. Fat residues were removed with sonication in 5% detergent and 5% distilled water for 5 minutes for each mesh (20). Average reduction in pore size due to the tissue removal process was less than 3%. The dimension of mesh samples for pore size analysis was 2.54 cm × 2.54 cm. Pristine meshes of the same brands were used as control groups.

Table 2. 1. Mesh information

	Small pore mesh	**Large pore mesh**
Brand	Composix® Kugel®	Prolene® Soft
Weight (g/m^2)	95	45
Classification (18,19)	Standard, III	Light, I
Porosity	57%	66%
Structure	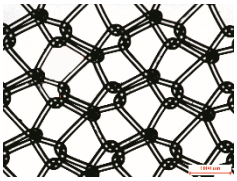	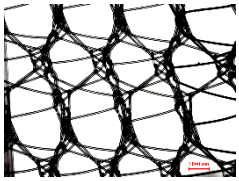
Material	PP sewn to ePTFE film	Lightweight PP

Coda's classification: ultra-light: < 35 g/m^2; light: 35 ~ 70 g/m^2; standard: 70 g/m^2 ~ 140 g/m^2; heavy: ≥ 140 g/m^2.

Table 2. 2. Patient demographics for explanted mesh

Mesh	Number (F/M)	*In vivo* time (months)	Patient age (years)	BMI
Small pore mesh	17 (7/10)	28 ± 19	62 ±13	31 ± 5.2
Large pore mesh	8 (3/5)	23 ± 27	59 ±17	30 ± 3.3

Photogrammetric Method

The photogrammetric method included image capture, image processing and image analysis to classify pore pattern, to measure pore size and to evaluate changes in pore size after physiological loading.

Image Capture

Mesh pore size was measured using a modified digital photogrammetric method based on the work of Mühl et al. (17). Mesh samples (2.54 cm × 2.54 cm) were mounted onto a square mesh holder (2.5 cm length × 3.5 cm height) fabricated from clear acrylic (0.3175 cm thickness) to allow for optimal light transmission. Mesh samples were fixed onto the mesh holder under uniform tension (0.039 N) and illuminated with transmitted light using a stereo optical microscope (SMZ-168, Motic, Richmond, Canada). Calibrated digital images (1392 × 1040 pixels, 96 dpi, RGB, TIFF format) were acquired at magnifications of 6x (0.124 pixel/μm) for large pore mesh and 12x (0.243 pixel/μm) for small pore mesh using the attached digital camera (Infinity 2, Lumenera, Ottawa, Canada). The magnifications and light intensity were selected to provide adequate resolution of the mesh filaments while fully capturing the pore pattern of each mesh type. Using this procedure, the average variance in pore size due to image capture by different operators was controlled within 5% (21).

Image Processing

Automated detection of pores was pursued to minimize human errors and avoid the time-consuming steps required for manual digitization. Image processing algorithms were programmed (Matlab R2016a, Mathworks, Natick, MA) to accomplish three steps: binary image conversion, noise removal and region selection (Figure 2.3). These steps were optimized for a single image of each mesh type and then applied to process the large quantity of acquired images. Final data output included pore sizes scaled for the image magnification using the calibrated pixel parameters.

Binary image conversion was used to compensate for uneven illumination caused by the surface, structure and transparency of the polypropylene fibers. Wolf's algorithm for binarization overcomes global threshold limitations by using local image thresholding in terms of contrast instead of actual gray values of the pixels (22-24). The original RGB color images (3-D arrays) were converted to grayscale images (1-D array) using standard transform coefficients (I = 0.2989 *R + 0.5870 * G + 0.1140 *B, with individual values from 0 to 255 for each pixel). A rectangular window was defined and shifted across the image, with the user optimizing the window size for edge detection of individual fibers defining the pore pattern. Thresholding was accomplished in the rectangular windows and an appropriate local threshold value (T) was calculated using Wolf's algorithm:

$$T = (1 - a)m + aM + a\frac{s}{R}(m - M), \text{ R} = \max(s),$$

where "a" was a gain parameter, "M" was the minimum value of gray level of the entire image, and "R" was set as the maximum standard deviation of all windows of the image (23). This produced binary images with pore areas assigned a value of "1" (white)

and fiber edges assigned a value of “0” (black). It was confirmed that the difference between the original and binarized image resulted in ≤ 5% deviation in fiber diameter.

Noise removal, including random pixels within the pore and within the fiber, was recognized in the initial image by the user and then automatically filtered for subsequent images. The size of random pixels in the noise regions and the ratio between the major and minor axis of noise in fibers appearing in the shape of long thin sticks were set as filter parameters by the user. Such noise was originated from over-exposure, reflection and other contaminants during image acquisition.

Region selection was visually confirmed by the user with appropriate pore inclusion or exclusion according to the pore pattern, and removal of incomplete pores near the image border that lacked a defined circumference of fibers. The user was able to manually add or delete pores as needed, depending on image quality. Final pore size was calculated as the number of pixels in white areas measured in the processed images and converted into square micrometers according to the calibration factor (length/pixel ratio) of the microscope-digital camera system. User inputs for image processing of a given mesh type were saved as a final configuration file and then applied to numerous images of the same type of mesh.

Image Analysis

The number of images per mesh type was determined using an over-sampling approach and evaluating deviations from true pore size due to measurement errors and variations in pore size within each mesh sample (25). This approach determined the minimum number of pores needed to represent the median true pore size within 5% based

on the pore pattern and pore size distribution. Multiple images of pristine mesh type (60 images for large pore mesh, 50 images for small pore mesh) were analyzed, providing for measurement of over 1000 pores per type and calculation of the true pore size. Meshes were assumed to be uniform over all measured areas. The first step to determine the minimum number of pores needed to represent the pore size used

$$n = \frac{(\frac{Z\alpha}{2})^2 \sigma^2}{E^2},$$

where n is the sample number of pores, Z is the critical value for a standard normal distribution at $\alpha = 0.05$, σ is the population variance, and E is the error arbitrarily set to be within 10% of the true pore size. The second step was to increase the calculated sample number (n) of pores gradually (e.g. n+1, n+2, etc.) until the average pore size measured using the sample number of pores was not significantly different compared to the true pore size. Pore size for explanted meshes was measured from the minimum number of pores and compared to the pristine meshes. Differences between the pore size of pristine and explanted meshes was analyzed by t-test and Wilcoxon Signed Rank Sum Test ($\alpha = 0.05$). All statistical analyses were run in OriginLab 9.0 (Northampton, Massachusetts, USA).

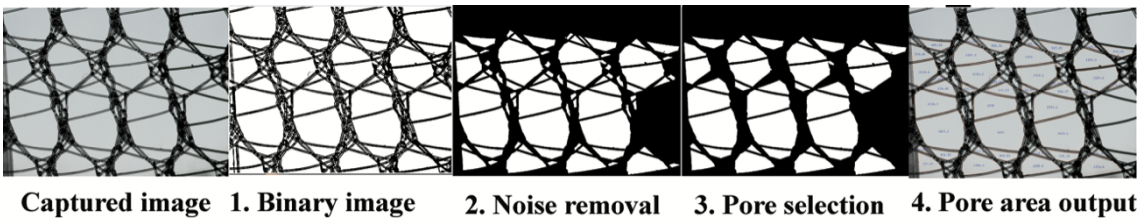

Figure 2. 3. Photogrammetric method.
The captured image was process by step 1. binary image conversion, step 2. noise removal, step 3. region selection, step 4. measured pore size output.

Results

Pore Size Distribution

There was a broad variation in pore sizes within the small pore and large pore meshes, with definitive bin groups easily visualized in histograms of the pristine meshes (Figure 2.4). There were two pore bin groups in the small pore mesh and four pore bin groups in the large pore mesh based on the pore pattern and pore size distribution (Table 2.3). These bins were consistent with the pore pattern and in some cases, different pore shapes had similar pore sizes (Figure 2.4b). The pore pattern in the small pore mesh consisted of two pore shapes with two bin groups of different pore sizes, namely bin 1 (0-0.4 mm^2) and bin 2 (0.4-0.7 mm^2) (Figure 2.4a). The pore pattern in the large pore mesh consisted of nine pore shapes with four bin groups of different pore sizes, namely bin 1 (0-0.3 mm^2), bin 2 (0.3-0.8 mm^2), bin 3 (0.8-2.6 mm^2), and bin 4 (2.6-4.0 mm^2) (Figure 2.4b).

Based on the oversampling approach, the minimum number of pores needed to represent the true pore size varied with pore pattern. Small pore mesh required a minimum of 3 pores in both bin 1 and bin 2 for the measured pore size to be statistically similar to the true pore size (Wilcoxon test, $p > 0.05$). Large pore mesh required a minimum of 60, 11, 22, and 6 pores in bin 1, bin 2, bin 3 and bin 4, respectively for the measured pore size to be statistically similar to the true pore size (Wilcoxon test, $p > 0.05$). These minimum numbers of pores were further used for data collection for explanted meshes.

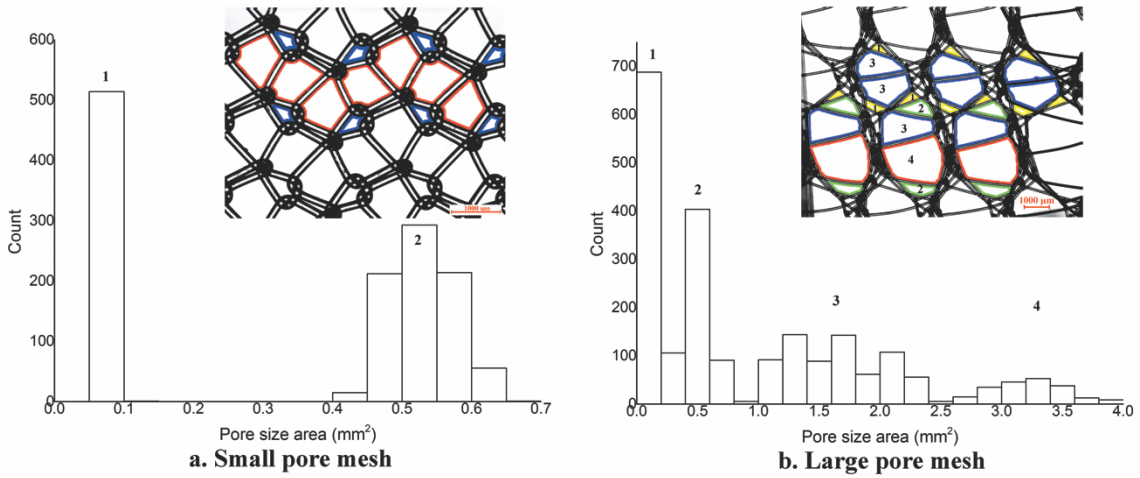

Figure 2. 4. Histogram of pore size distribution in pristine meshes.
a. Two bin groups in small pore mesh: bin 1 (0-0.4 mm^2) included same pore shapes with blue outline; bin 2 (0.4-0.7 mm^2) included same pore shapes with red outline. b. Four bin groups in large pore mesh: bin 1 (0-0.3 mm^2) included pores with yellow outline; bin 2 (0.3-0.8 mm^2) included pores with green outline; bin 3 (0.8-2.6 mm^2) included pores with blue outline; bin 4 (2.6-4.0 mm^2) included same pore shapes with red outline. The pores in bin 1, bin 2 and bin 3 were in different pore shapes. Scale bar: 1000 μm.

Pore Size Change after Implantation

The changes of pore sizes depended on the pore shapes. The changes of pore sizes in bin 1 in both explanted meshes were not significantly different from the pristine controls (t-test, $p > 0.05$) (Table 2.4). However, the explanted meshes in both types had significantly smaller pore sizes in the large bins (bin 2 for small pore mesh, bin 2, 3 & 4 for large pore mesh) compared to the pristine controls (t-test, $p < 0.01$) (Table 2.4). The pore sizes of bin 1 (0-0.4 mm^2) in the individual explanted small pore mesh with 24-month and 38-month implantation time increased, which contributed to the reduction of pore sizes in bin 2 (0.4-0.7 mm^2) due to the flexible knitted structure (Figure 2.5a). This also resulted in the increased pore size of bin 1 (0-0.3 mm^2) in large pore mesh with 13-month implantation time (Figure 2.5b). Nearly all explanted meshes in both types (23 of

25) had significantly smaller pores in the largest bin groups (bin 2 for small pore mesh, bin 4 for large pore mesh) compared with pristine control meshes (Wilcoxon test, $p < 0.05$) (Figure 2.5), including 16 out of 17 explanted small pore mesh had significantly smaller pores (Wilcoxon test, $p < 0.05$) in bin 2 compared to pristine mesh and 7 out of 8 explanted large pore mesh had significantly smaller pores (Wilcoxon test, $p < 0.05$) in bin 4 compared to pristine mesh. The difference between unchanged or increased pore sizes of explanted mesh and pristine mesh was much smaller than the difference between decreased pore sizes and pristine mesh, which indicated the overall reduction of pore size. The difference between pristine and pristine mesh treated by chemicals was smaller than the difference between pristine mesh and explanted mesh, which indicated the shrinkage of pore size occurred during implantation.

Table 2. 3. The pore sizes within the pristine pore bins were normally distributed

Mesh type	Measurements of pores without bins		Measurements of pores based on bins		
	Mean ± SD (mm^2)	Median (mm^2)	Bin # (range) (mm^2)	Mean ± SD (mm^2)	Median (mm^2)
Small pore mesh	0.35 ± 0.22	0.49	1 (0.0-0.4)	0.08 ± 0.01	0.08
			2 (0.4-0.7)	0.53 ±0.04	0.53
Large pore mesh	1.00 ± 0.99	0.54	1 (0.0-0.3)	0.14 ± 0.05	0.13
			2 (0.3-0.8)	0.53 ± 0.09	0.51
			3 (0.8-2.6)	1.64 ± 0.38	1.63
			4 (2.6-4.0)	3.22 ± 0.29	3.26

Table 2. 4. Pore size of explanted meshes and p-values compared with pristine meshes

Mesh type	Bin	Explanted mean ± SD (mm^2)	Pristine mean ± SD (mm^2)	T-test
Small pore mesh	1	0.08 ± 0.01	0.08 ± 0.01	p = 0.49
	2	0.44 ±0.05	0.53 ±0.04	**
Large pore mesh	1	0.13 ± 0.02	0.14 ± 0.05	p = 0.22
	2	0.39 ± 0.04	0.53 ± 0.09	**
	3	1.48 ± 0.12	1.64 ± 0.38	**
	4	2.85 ± 0.28	3.22 ± 0.29	**

*: $p < 0.05$, **: $p < 0.01$

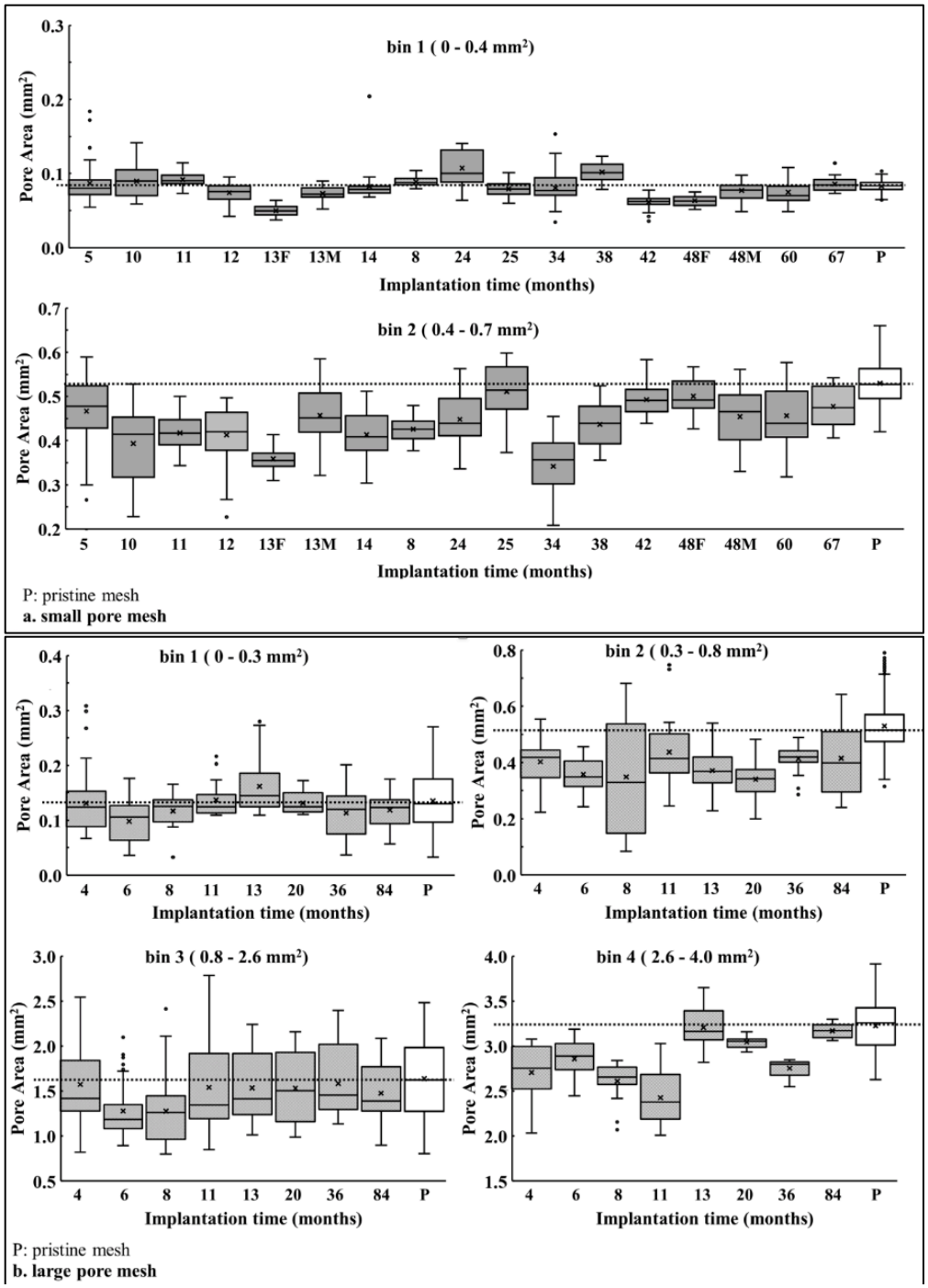

Figure 2. 5. Comparison between pore size in explanted mesh and pristine mesh. Pore area as a function of implantation time for a) small pore mesh and b) large pore mesh. Meshes with same implantation time were distinguished by sex (M/F) of the patient (Appendix A). Explanted mesh had significantly smaller pore sizes compared to pristine mesh for bin 2 in small pore mesh and bin 2, 3, 4 for large pore mesh.

Discussion

This study developed an automated digital photogrammetric method using image capture, image processing and image analysis to measure pore size within the context of different pore patterns for two types of PP surgical mesh. The measurement system used a simple light microscopy set-up and automated detection of pores, which helped to minimize human errors and provide for efficient pore detection. Different pore patterns and pore size distributions were characteristic for different mesh types (Figure 2.4). Applying this method to explanted mesh, same pore sizes in small bins and significantly smaller pore sizes in large bins were detected compared with pristine control meshes (Table 2.4).

Identifying pore pattern before measuring pore size is crucial because knitting structures affect pore shape and the associated pore size. From the view of knitting technology, two-guide bar structures are used to form larger pore sizes and specific net shapes, such as diamonds and hexagons (12). However, these shapes are not always symmetrical, especially when knitting using a single-guide bar structure. The photogrammetric technique in the current study provides for direct measurement of pore size area without assuming a symmetrical pore shape. Other studies approximate pore size using an assumed shape (e.g. square or circle), which can produce errors in pore size area measurements (12, 17). For example, assuming a 1 mm pore size (26), such simplifications assuming a square or circle shape lead to a 0.215 mm^2 difference in pore size. Identifying pore pattern and measuring pore size area based on the actual pore shape within the identified pore pattern avoids this error.

Recognizing pore pattern and measurement of pore size support *in vivo* assessments of mesh shrinkage. *In vivo* mesh shrinkage generally describes changes in overall mesh dimensions, leading to expansion or shrinkage in the overall mesh size and changes in pore size. The observed reduction in pore size of explanted mesh support other studies that have documented changes in mesh size and pore size. Harsløf et al. reported 20% shrinkage in overall mesh change in a small pore mesh having comparable 15% shrinkage, which was estimated by pore pattern and change of pore size in the small pore mesh in the current study (27). Coda et al. reported the alternation of pore size of various types of PP mesh ranged from -40% (shrinkage) to +58.5% (expansion) having comparable alternation of pore sizes in the current study from -19% (shrinkage) to +23% (expansion) (28).

Linking the analysis of pore size to textile structure is important for understanding the mechanical compatibility between mesh and host tissues. When a mesh is implanted in the abdominal wall, the anisotropic host tissues will induce various force, such as biaxial tension on the implanted mesh. Applying biaxial tension on a warp-knitted mesh will induce various changes in mesh pore size due to the anisotropic and nonlinear mesh mechanical properties (29). When the whole pore diameter is less than 1 mm, tissue integration may not occur (6). The mechanical mismatch between implanted mesh and host tissues can result in mesh failure or failure of tissue integration.

Structural stability and chemical composition of mesh can influence the degree of mesh contraction, providing possible mechanisms for the changes in pore size observed in the current study. Injury models of load-bearing tissues (e.g. tendon and muscle)

suggest that the abdominal wall may be dependent on mechanical strains to signal wound repair (30) and induce proliferation and parallel arrangement of fibroblasts and collagen fibers (31), which contribute to the difficulty of mesh recovery to its original pore structure after tissue removal (20, 32). In cases of infection and chronic inflammation, reactive oxygen species (ROS) and myeloperoxidase (MPO) are present around the mesh, capable of oxidizing PP mesh and causing radical scission and changes in crystallinity (33-36). The increased brittleness and loss of flexibility may contribute to the changes in mesh pore size.

Limitations of this study are common to studies of explanted biomaterials, namely the meshes were obtained at the time of revision surgery without controlling for age, implantation time of mesh, or comorbidities of patients. Another limitation is that the imaging method assumes a two-dimensional projection for pore size measurement. The change in the size and shape of the stitches in cross-section view in physiological conditions is still unknown and needs to be studied in the future.

Conclusion

An automated digital photogrammetric method using image capture, image processing and image analysis to measure pore size was developed. Applying this method to explanted mesh, pore sizes in small bins were unchanged and pore sizes in large bins were 17% smaller for small pore mesh and 16% smaller for large pore mesh, on average, compared to pristine meshes. Given that movement of surrounding loops formed by warp knitted mesh filaments during loading can alter pore size in warp knitted mesh, it would

be beneficial to study the movement of mesh filaments in microscale *in vivo* and explore its impact on mesh-tissue interactions.

References

1. Klinge U, Park J, Klosterhalfen B. The Ideal Mesh? Pathobiology. 2013;80(4):169.

2. Klinge U, Klosterhalfen B, Müller M, Schumpelick V. Foreign Body Reaction to Meshes Used for the Repair of Abdominal Wall Hernias. Eur J Surg 1999;165(7):665-73.

3. Orenstein SB, Saberski ER, Kreutzer DL, Novitsky YW. Comparative Analysis of Histopathologic Effects of Synthetic Meshes Based on Material, Weight, and Pore Size in Mice. J Surg Res. 2012;176(2):423-9.

4. Zogbi L, Trindade EN, Trindade MRM. Comparative study of shrinkage, inflammatory response and fibroplasia in heavyweight and lightweight meshes. Hernia. 2013;17(6):765-72.

5. Kuehnert N, Kraemer NA, Otto J, Donker HC, Slabu I, Baumann M, Kuhl CK, Klinge U. *In vivo* MRI visualization of mesh shrinkage using surgical implants loaded with superparamagnetic iron oxides. Surg Endosc. 2011;26(5):1468-75.

6. Klinge U, Klosterhalfen B, Birkenhauer V, Junge K, Conze J, Schumpelicka V. Impact of polymer pore size on the interface scar formation in a rat model. J Surg Res. 2002;103(2):208-14.

7. Klinge U, Dietz U, Fet N, Klosterhalfen B. Characterisation of the cellular infiltrate in the foreign body granuloma of textile meshes with its impact on collagen deposition. Hernia. 2014;18(4):571-8.

8. Sanders D, Lambie J, Bond P, Moate R, Steer JA. An *in vitro* study assessing the effect of mesh morphology and suture fixation on bacterial adherence. Hernia. 2013;17(6):779-89.

9. Zhu L, Schuster P, Klinge U. Mesh implants: An overview of crucial mesh parameters. World J Gastrointest Surg. 2015;7(10):226.

10. Jiang G, Miao X, Lee D. Process of warp knitting mesh for hernia repair and its mechanical properties. Fibres Text East Eur. 2005;13(3):44-6.

11. Spencer DJ, Knitting technology: a comprehensive handbook and practical guide, 3rd ed. Cambridge, UK: Woodhead Publishing; 2001.

12. Miao L, Wang F, Wang L, Zou T, Brochu G, Guidoin R. Physical characteristics of medical textile prostheses designed for hernia repair: a comprehensive analysis of select commercial devices. Materials. 2015;8(12):8148-68.

13. Klinge U, Otto J, Mühl T. High structural stability of textile implants prevents pore collapse and preserves effective porosity at strain. Biomed Res. Int. 2015;2015:1-7.

14. Barone WR, Moalli PA, Abramowitch SD. Textile properties of synthetic prolapse mesh in response to uniaxial loading. Am J Obstet Gynecol. 2016;215(3):326.e1,326.e9.

15. Hashemi N, Asayesh A, Jeddi AAA, Ardakani T. The influence of two bar warp-knitted structure on the fabric tensile stress relaxation Part I: (reverse locknit, sharkskin, queens' cord). J Text I. 2016;107(4):512-13.

16. Ardakani T, Asayesh A, Jeddi AAA. The influence of two bar warp-knitted structure on the fabric tensile stress relaxation Part II: (locknit, satin, loop raised). J Text I. 2016;107(11):1357-1368.

17. Mühl T, Binnebösel M, Klinge U, Goedderz T. New objective measurement to characterize the porosity of textile implants. J Biomed Mater Res B. 2008;84B(1):176-83.

18. Coda A, Lamberti R, Martorana S. Classification of prosthetics used in hernia repair based on weight and biomaterial. Hernia. 2012;16(1):9-20.

19. Klinge U, Klosterhalfen B. Modified classification of surgical meshes for hernia repair based on the analyses of 1,000 explanted meshes. Hernia. 2012 06/01;16(3):251-8.

20. Burns-Heffner C. Development of explant registry and mechanical testing of pristine and explanted surgical mesh [dissertation]. ProQuest Dissertations Publishing; 2014.

21. Lu X, Sun L, Heniford BT, Harman MK. Pore size characterization methods for explanted surgical mesh. World Congress of Biomaterials, Montreal, Canada. 2016.

22. Wu S, Amin A. Automatic thresholding of gray-level using multistage approach. IEEE; 2003.

23. Wolf C, Jolion J M, Chassaing F. Text localization, enhancement and binarization in multimedia documents. IEEE Object recognition supported by user interaction for service robots 2002.

24. Otsu N. A Threshold Selection Method from Gray-Level Histograms. IEEE Transactions on Systems, Man, and Cybernetics. 1979;9(1):62-6.

25. Que L, Topoleski LDT. Surface roughness quantification of CoCrMo implant alloys. J Biomed Mater Res. 1999;48(5):705-11.

26. Conze J, Rosch R, Klinge U, Weiss C, Anurov M, Titkowa S, Oettinge A, Schumpelick V. Polypropylene in the intra-abdominal position: Influence of pore size and surface area. Hernia. 2004;8(4):365-72.

27. Harsløf S, Zinther N, Harsløf T, Danielsen C, Wara P, Friis-Andersen H. Mesh shrinkage depends on mesh properties and anchoring device: an experimental long-term study in sheep. Hernia 2017;21(1):107-13.

28. Coda A, Bendavid R, Botto-Micca F, Bossotti M, Bona A. Structural alterations of prosthetic meshes in humans. Hernia. 2003;7(1):29-34.

29. Deeken CR, Thompson J,Dominic M., Castile RM, Lake SP. Biaxial analysis of synthetic scaffolds for hernia repair demonstrates variability in mechanical anisotropy, non-linearity and hysteresis. J Mech Behav Biomed Mater. 2014;38:6-16.

30. Wang JH, Thampatty BP, Lin J, Im H. Mechanoregulation of gene expression in fibroblasts. Gene. 2007;391(1):1-15.

31. Gould RA, Chin K, Santisakultarm TP, Dropkin A, Richards JM, Schaffer CB, Butcher JT. Cyclic strain anisotropy regulates valvular interstitial cell phenotype and tissue remodeling in three-dimensional culture. Acta Biomater. 2012;8(5):1710-9.

32. Casey EM. Physical characterization of surgical mesh after function in hernia repair [dissertation]. ProQuest Dissertations Publishing; 2015.

33. Ostergard DR. Degradation, infection and heat effects on polypropylene mesh for pelvic implantation: what was known and when it was known. Int Urogynecol J. 2011;22(7):771-4.

34. Iakovlev VV, Guelcher SA, Bendavid R. Degradation of polypropylene *in vivo*: A microscopic analysis of meshes explanted from patients. J Biomed Mater Res B. 2017;105(2):237-48.

35. Wood AJ, Cozad MJ, Grant DA, Ostdiek AM, Bachman SL, Grant SA. Materials characterization and histological analysis of explanted polypropylene, PTFE, and PET hernia meshes from an individual patient. J Mater Sci Mater Med. 2013;24(4):1113-22.

36. Gil D. Naturally derived anti-inflammatory and antibacterial coatings for surgical implants [dissertation]. ProQuest Dissertations Publishing; 2017.

CHAPTER THREE

ANALYZING MATERIAL CHANGES CONSISTENT WITH DEGRADATION OF EXPLANTED SURGICAL MESH RELATED TO CLINICAL CHARACTERISTICS

Introduction

Surgical guidelines recommend hernia mesh implants as the general standard for inguinal hernia repair (1). In use since the 1960s, polypropylene (PP) biomaterials are common in commercially available hernia meshes due to their high tensile strength, good flexibility, and chemical resistance (2). Although *in vivo* biomechanical and biochemical mechanisms have the potential to degrade biomaterials (3-8); the extent of *in vivo* degradation of PP mesh implants is currently under debate (9-11). Some studies of explanted PP mesh implants cite changes in chemical markers (e.g. surface oxidation and crystallinity) and physical markers (e.g. surface cracking and reduced compliance) as evidence of *in vivo* degradation of the PP mesh (6, 12-15). Other studies of explanted PP mesh implants cite an absence of changes in chemical markers, most notably in PP formulated with antioxidant stabilizers, and attribute surface cracking to artifacts from formalin-fixed proteins adhered to the mesh surface (3, 10, 16). Ineffective cleaning of explanted PP mesh (10) and highly variable clinical conditions, such as the presence of acute infection or chronic inflammation, further complicate these seemingly contradictory results (16).

There are several mechanisms that potentially contribute to PP mesh *in vivo* degradation. One proposed mechanism involves reactive oxygen species (ROS) and

myeloperoxidase (MPO) that are present in cases of infection and chronic inflammation in peritoneal fluid (5, 17, 18). These chemicals are capable of oxidizing PP mesh and causing radical scission, and possibly leading to changes in crystallinity (5, 12, 15, 16, 19). Another proposed mechanism involves sustained and cyclic mechanical strains in the mesh that exist during the surgical procedure and healing process and with patient activities after implantation (20-22). Such strains are capable of increasing localized stress, initiating structural cracks in individual fibers, and causing polymer chain scission, which may contribute to PP degradation such as surface cracking, changes in crystallinity, and even mesh failure (7, 12, 20, 21). The degraded PP may increase the inflammatory response around the implanted mesh, potentially increasing the concentrations of ROS and MPO and leading to further PP degradation (12).

Highly variable *in vivo* conditions expose a mesh to a mechanism that potentially contributes to PP mesh degradation and complicates the analysis of explanted PP mesh. Surgical placement of the mesh within the peritoneal cavity (intra-peritoneal location) results in mesh being in contact with peritoneal fluid. The peritoneal fluid actively exchanges leukocytes with blood (23) and contains increased ROS released from leukocytes or macrophages in cases of infection or chronic inflammation (17, 24), thus creating the chemical environment for PP degradation. Surgical injuries or infection are the triggers causing fibrosis or scar formation of the peritoneum, applying increased mechanical strain on implanted mesh for PP degradation (23). Medical comorbidities, such as obesity (25), diabetes (26-28) and tobacco use (26) can alter and delay wound healing. These medical comorbidities can lead to chronic inflammation and abnormal

tension applied on mesh, creating the chemical and mechanical environment for PP degradation.

Mesh selection also potentially contributes to PP mesh degradation. Mesh with small pore sizes has a larger surface contact area with host tissues, inducing higher inflammatory infiltrate to the mesh surface by attracting inflammatory cells, such as macrophages (29-31). These inflammatory cells on the mesh surface release ROS, increasing the amounts of ROS around the mesh and creating the chemical environment for PP degradation. Mesh with small pore sizes also induces less tissue integration but higher fibrous encapsulation, leading to higher tissue contraction (22, 32-34). This contraction applies mechanical strains on the mesh, creating a mechanical environment for PP degradation. Mesh with highly deformable pore shape can behave similarly to mesh with small pores under the biaxial tension caused by abdominal wall distension, healing process or tissue contraction (29, 35).

To date, few studies of explanted PP mesh have explored specific mechanisms that potentially contribute to PP mesh degradation. Evidence of degradation is confounded by contamination from chemical fixatives and adhered biological debris, highly variable *in vivo* conditions that are infrequently documented, and small sample sizes that are not suitable for meaningful statistical analysis. There is need for explant analysis of PP hernia mesh that centers on potential degradation mechanisms and investigates clinical characteristics that may trigger material changes consistent with PP degradation. The purposes of this study were: 1) to evaluate mesh surface oxidation, crystallinity, and mechanical properties of fresh frozen explanted PP meshes; and 2) to

investigate whether material changes consistent with PP degradation are related to infection, mesh placement location, and mesh pore size. The hypothesis were: 1) mesh explanted from patients with infection had more PP material changes than mesh explanted from non-infected patients; 2) mesh implanted in an intra-peritoneal location had more PP material changes than mesh implanted in an extra-peritoneal location; and 3) mesh with small pore size had more PP material changes than mesh with large pore size.

Materials

Hernia meshes were collected by the surgeon co-authors (BTH, VA) through an established registry of explanted meshes (MeshWatch) using a protocol approved by the Clemson University Institutional Review Board (IRB2014-161). Meshes from consecutive patients undergoing revision hernia surgery were archived and stored fresh-frozen at -80° C until analysis. To date, there are 164 explanted hernia meshes of various types in the registry along with documentation of basic patient demographics and clinical history abstracted from available records and details of mesh structure and type. The registry database was queried to identify all meshes meeting five characteristic inclusion criteria. 1) The meshes were explanted by the same surgical team at the same medical center. 2) The mesh material was PP. 3) The meshes were received before the start of this study (December 2017). 4) The mesh structure was in the pictorial "MeshWatch" atlas of known mesh types in the mesh registry (36). 5) The mesh structure was warp knitted. Sixty-three meshes of 10 known mesh structures (9 mesh types, including two different

mesh structures for same mesh type, as described in Chapter 1, Table 1.1) met those inclusion criteria (n = 63) and were selected for further analysis.

The included meshes (n = 63) were explanted from 62 patients after a median implantation time of 24 (range: 5 to 156) months. There were 32 female patients (average age at removal: 58 ± 11 years old) and 30 male patients (average age at removal: 59 ± 10 years old), including two meshes retrieved from one male patient (Table 3.1). Patient records included sex, age at removal, BMI, and mesh implantation time. The year of the mesh implanted (range: 2002 to 2016) into a patient was estimated using the year of the mesh removed (range: 2013 to 2017) and the implantation time. Medical records included history of infection, diabetes, recurrent hernia, smoking and previous hernia repair. Surgical records included mesh placement and reasons for mesh removal. The reasons for mesh removal included infection (n = 8), incarcerated hernia (n = 29, two patients with both infection and incarcerated hernia), bowel obstruction (n = 2), mesh not working (n = 15), chronic pain (n = 3), other individual issues (n =8). Some patients did not have full records: 1) Eight patients did not have records of recurrent hernia. 2) Four patients did not have records of implantation time. 3) Two patients did not have records of infection, including one patient who did not have a recorded history of mesh placement anatomic location, implantation time, diabetes, previous hernia repair, and reasons for removal.

Using the data of medical records, the included meshes were grouped into meshes from infected patients (n = 8) and meshes from non-infected patients (n = 53). Based on the comorbidities, the included meshes were grouped into meshes from patients with diabetes (n = 16) and without diabetes (n = 46), with previous hernia repair (n = 44) and

without previous hernia repair (n = 18), with recurrent hernia (n = 52) and without recurrent hernia (n = 3), and with a history of smoking (n = 4) and without a history of smoking (n = 59).

According to surgical records, the included meshes were grouped into two anatomic locations based on mesh placement before retrieval: intra-peritoneal (Intra) location (n = 24) and extra-peritoneal (Extra) location (n = 38). The extra-peritoneal location included four anatomic locations: onlay (n = 11), inlay (n = 4), underlay (n = 15), and sublay (n = 8) (37).

According to mesh selection, the included meshes were classified into three groups based on modified Klinge's classification: Class I (n = 22) were large pore meshes (textile porosity > 60%); Class II (n = 23) were small pore meshes (textile porosity < 60%); and Class III (n = 18) were meshes with special features, such as barrier layer or surface coating (Table 3.2) (38). For the explanted meshes, the presence of an absorbable surface coating at the time of implantation could not be traced and therefore, only meshes with an e-PTFE layer were classified into Class III. All other meshes were classified into Class I or Class II based on the porosity. Overall, the mesh explants represented 10 mesh structures of 9 different commercially available mesh types.

Table 3. 1. Patient information (Class I)

Mesh #	Mesh Class	Sex (F/M)	Age at removal (yrs)	BMI	Implantation time (mons)	Mesh location
1	I	F	49	29.3	48	onlay
2	I	M	68	33.6	11	onlay
3	I	M	60	45.3	132	onlay
4	I	F	68	28.6	9	onlay
5	I	F	37	37.6	53	onlay
6	I	M	68	28.6	33	onlay
7	I	F	60	45.0	24	inlay
8	I	F	58	30.9	7	inlay
9	I	F	48	39.1	8	underlay
10	I	M	48	19.9	37	underlay
11	I	M	58	28.0	16	underlay
12	I	M	51	33.7	18	underlay
13	I	M	51	33.7	18	underlay
14	I	M	73	28.3	19	sublay
15	I	F	51	40.2	5	intra-peritoneal
16	I	M	50	30.5	25	intra-peritoneal
17	I	F	32	34.0	54	intra-peritoneal
18	I	F	67	30.1	22	intra-peritoneal
19	I	F	78	40.7	96	intra-peritoneal
20	I	M	57	29.9	9	intra-peritoneal
21	I	F	56	32.9	48	intra-peritoneal
22	I	F	41	33.5	12	intra-peritoneal

Mesh #	Infection (Y/N)	Removal reason/ Recurrent hernia (Y/N)	Smoker/Diabetes/Previous hernia repair (Y/N)
1	N	incarcerated hernia/Y	N/N/Y
2	N	seroma/Y	N/N/Y
3	Y	infection/Y	N/N/N
4	N	incarcerated hernia/Y	N/N/Y
5	N	incarcerated hernia/Y	N/Y/Y
6	N	incarcerated hernia/Y	N/N/Y
7	N	mesh not working/Y	N/Y/N
8	N	mesh not working/Y	N/N/Y
9	N	mesh not working/Y	Y/N/Y
10	N	chronic pain/Y	Y/N/N
11	N	incarcerated hernia/Y	N/N/N
12	Y	infection/Y	N/N/N
13	Y	infection/Y	N/N/N
14	N	incarcerated hernia/Y	N/N/Y
15	Y	infection/Y	N/N/Y
16	N	mesh not working/Y	N/N/N
17	N	incarcerated hernia/Y	N/N/Y
18	N	incarcerated hernia/Y	N/N/Y
19	Y	infection/Y	N/N/Y
20	N	incarcerated hernia/Y	N/N/Y
21	N	incarcerated hernia/Y	N/N/N
22	N	mesh not working/Y	N/N/Y

Table 3.1. Patient information (Class II)

Mesh #	Mesh Class	Sex (F/M)	Age at removal (yrs)	BMI	Implantation time (mons)	Mesh location
23	II	M	74	30.1	24	onlay
24	II	F	41	35.3	24	inlay
25	II	M	63	44.3	8	underlay
26	II	M	54	26.9	36	underlay
27	II	M	70	29.2	12	underlay
28	II	M	54	33.1	15	underlay
29	II	F	34	38.1	30	underlay
30	II	M	60	32.3	14	underlay
31	II	F	58	45.9	48	underlay
32	II	F	64	41.6	18	underlay
33	II	M	75	28.8	9	sublay
34	II	M	75	28.8	18	sublay
35	II	M	71	47.3	48	sublay
36	II	F	52	40.3	13	sublay
37	II	F	48	42.2	25	intra-peritoneal
38	II	F	65	36.7	15	intra-peritoneal
44	II	M	57	26.5	5	intra-peritoneal
45	II	F	75	30.8	31	intra-peritoneal
41	II	F	65	26.7	50	intra-peritoneal
42	II	M	71	28.7	13	intra-peritoneal
43	II	F	54	31.0	7	intra-peritoneal
44	II	F	61	29.5	28	intra-peritoneal
45	II	M	50	28.7	NA	NA

Mesh #	Infection (Y/N)	Removal reason/ Recurrent hernia (Y/N)	Smoker/Diabetes/Previous hernia repair (Y/N)
23	N	mesh not working/Y	N/Y/Y
24	Y	incarcerated hernia/Y	N/N/Y
25	N	incarcerated hernia/Y	N/Y/N
26	N	incarcerated hernia/Y	N/N/Y
27	N	incarcerated hernia/Y	N/N/Y
28	N	incarcerated hernia/Y	N/N/Y
29	N	incarcerated hernia/Y	N/N/N
30	N	incarcerated hernia/Y	N/N/Y
31	N	incarcerated hernia/Y	N/N/Y
32	N	incarcerated hernia/Y	N/N/Y
33	N	mesh not working/Y	N/N/Y
34	N	incarcerated hernia/N	N/N/N
35	N	incarcerated hernia/Y	N/Y/Y
36	N	mesh not /Y working/NA	N/Y/Y
37	N	mesh not working/Y	Y/Y/Y
38	N	mesh not working/Y	N/N/Y
44	N	mesh not working/Y	N/N/N
45	N	mesh attachment/Y	N/N/N
41	N	bowel obstruction/N	N/N/N
42	N	diastasis/Y	N/N/Y
43	N	fistula/Y	N/N/Y
44	Y	incarcerated hernia/Y	N/Y/Y
45	NA	NA/NA	Y/NA/NA

Table 3.1. Patient information (Class III)

Mesh #	Mesh Class	Sex (F/M)	Age at removal (yrs)	BMI	Implantation time (mons)	Mesh location
46	III	F	58	35.5	29	onlay
47	III	F	68	31.5	156	onlay
48	III	M	38	34.8	NA	onlay
49	III	M	69	28.0	9	inlay
50	III	M	44	34.4	13	underlay
51	III	F	64	25.0	11	underlay
52	III	M	43	44.4	84	sublay
53	III	F	54	48.9	NA	sublay
54	III	M	65	36.0	34	sublay
55	III	M	75	28.3	15	onlay
56	III	F	69	32.5	133	intra-peritoneal
57	III	F	68	32.8	NA	intra-peritoneal
58	III	M	55	29.0	120	intra-peritoneal
59	III	M	64	28.5	28	intra-peritoneal
60	III	F	42	50.5	96	intra-peritoneal
61	III	F	65	34.3	41	intra-peritoneal
62	III	M	65	27.7	132	intra-peritoneal
63	III	F	58	29.5	84	intra-peritoneal

Mesh #	Infection (Y/N)	Removal reason/ Recurrent hernia (Y/N)	Smoker/Diabetes/Previous hernia repair (Y/N)
46	N	incarcerated hernia/Y	N/Y/Y
47	N	incarcerated hernia/Y	N/N/Y
48	N	mesh not working/NA	N/N/Y
49	N	incarcerated hernia/NA	N/Y/Y
50	N	chronic pain/N	N/N/N
51	N	seroma/NA	N/N/N
52	N	hard mesh/Y	N/Y/Y
53	N	incarcerated hernia/Y	N/N/Y
54	N	incarcerated hernia/Y	N/N/Y
55	Y	Infection/NA	N/Y/N
56	N	mesh not working/Y	N/Y/Y
57	N	incarcerated hernia/Y	N/Y/Y
58	N	incarcerated hernia/Y	N/Y/Y
59	N	chronic pain/NA	N/N/N
60	N	bowel obstruction/NA	N/Y/Y
61	N	mesh not working/Y	N/N/Y
62	N	mesh not working/Y	N/N/Y
63	NA	adhesion/Y	N/N/Y

Table 3. 2. Mesh structures

Class I (n = 22)	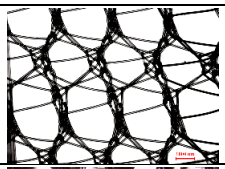	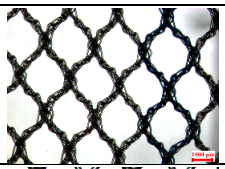	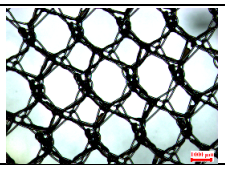	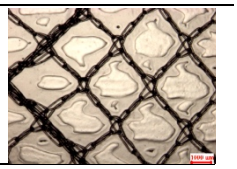
Class II (n = 23)	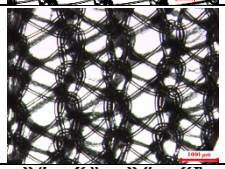	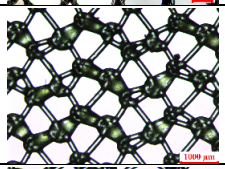		
Class III (n = 18)	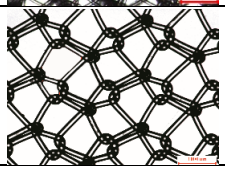	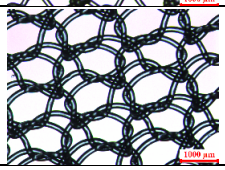	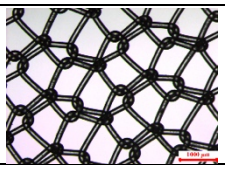	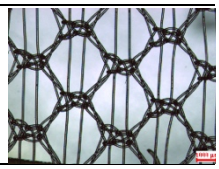

Methods

Explanted Mesh Handling

The explanted meshes were handled carefully. Selected explanted meshes were thawed to room temperature and carefully flattened (Figure 3.1). Four full thickness biopsies of 8 mm diameter (2 biopsies from peripheral location and 2 biopsies from middle location) were collected from each mesh for histological analysis. Two additional 2 cm × 2 cm mesh samples were cut for chemical and mechanical characterization. All biopsies and mesh samples were rinsed with 0.02 M phosphate buffer solution to remove excessive blood. Histological biopsies were fixed in 10% formalin buffer for 24 hours, followed by tissue processing, embedding, sectioning, and staining (39). The histology study is ongoing and will not be reported in this chapter. The adhered tissues on the mesh samples were removed before chemical and mechanical characterization.

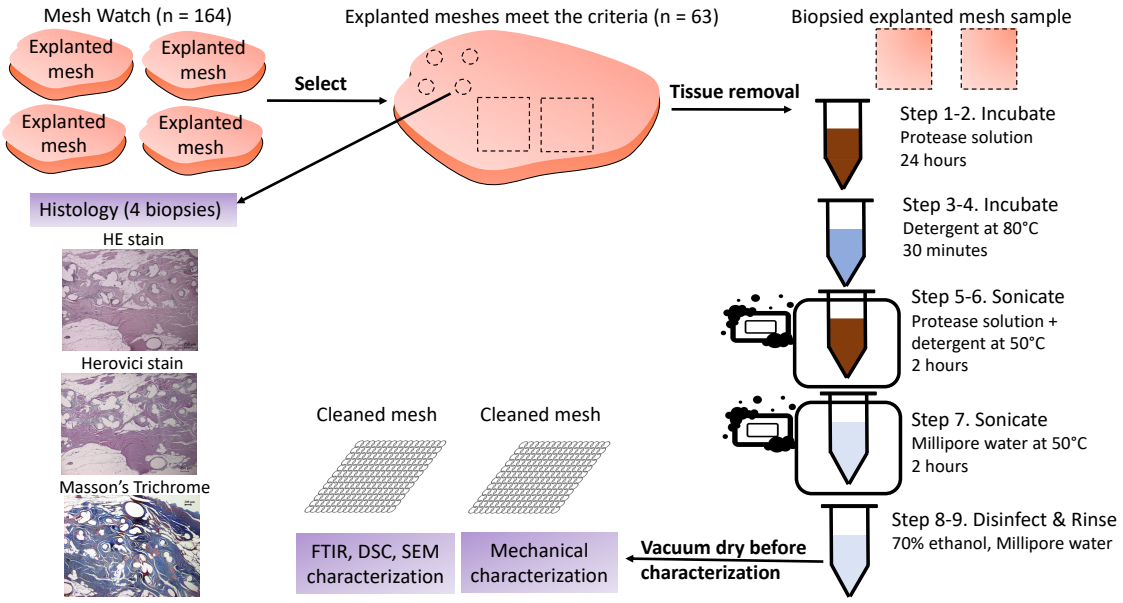

Figure 3. 1. Mesh handling and cleaning.

Mesh Sample Cleaning

The adhered tissues on the mesh samples were carefully removed using a 10-step modified cleaning protocol to avoid interference with subsequent analysis methods (Table 3.3) (10). Tissues were enzymatically removed by immersing in 1.5% NSPO034 protease solution (Novozymes, Bagsværd, Denmark) and 1.5% Alcalase 2.5 L (Novozymes, Bagsværd, Denmark) in 0.02 M phosphate buffer (pH = 7) at 50°C for 24 hours, followed by 0.5% detergent (Novozymes, Bagsværd, Denmark) bath at 80°C for 30 minutes. The tissue residues on mesh samples were further removed using fresh enzymatic solution and then fresh detergent solution for 2 hours respectively at 50°C in ultrasonic bath. The enzyme and detergent residues were rinsed off by Millipore water in ultrasonic bath at 50°C for 2 hours. Mesh samples were disinfected by soaking in 70% ethanol for 1 minute and rinsed in Millipore water and vacuum dried at ambient

temperature for chemical and mechanical characterization. Based on surgical record and visual identification of mesh structures, commercially available pristine meshes were processed as cleaned controls.

Table 3. 3. Mesh sample cleaning protocol

Step 1	Step 2	Step 3	Step 4	Step 5
Remove blood using PBS buffer	Digest tissues using enzyme solution at 50 °C for 24 hours	Check if the tissues are fully removed from the mesh, yes →step 4 no→step 2	Rinse and leave in 0.5% detergent at 80°C for 30 mins	Sonicate using fresh enzyme solution at 50 °C for 2 hours
Step 6	Step 7	Step 8	Step 9	Step 10
Sonicate using fresh detergent solution 50 °C for 2 hours	Rinse and sonicate in Millipore water 50 °C for 2 hours	Disinfect in 70% ethanol for 1 minute	Rinse using Millipore water	Vacuum dry before characterization

Cleaning Validation

Validation of cleaned mesh samples included visual assessment under a stereo optical microscope (SMZ-168, Motic, Richmond, Canada) and chemical assessment with Fourier-transform infrared spectroscopy (FTIR) (IRSpirit FTIR Spectrometer, Shimadzu, Kyoto, Japan), similar to the validation method reported by Thames et al. (10). Mesh samples with remaining adhered tissues were not translucent and had 1600-1690 cm^{-1} spectral peaks in FTIR, whereas clean mesh samples were translucent and the 1600-1690 cm^{-1} spectral peaks were absent. Based on preliminary testing, mesh samples were cleaned using the cleaning protocol (Table 3.3) until little improvement was observed under the microscope (Figure 3.2) and the peak representing proteins in the region of 1600-1690 cm^{-1} (Figure 3.3a, red curve) was not observed under FTIR (Figure 3.3a, blue curve). The peak in the region of 3300 cm^{-1} was not used as protein indicator because the range of 3100 – 3600 cm^{-1} also represented hydroxyl groups (10, 40).

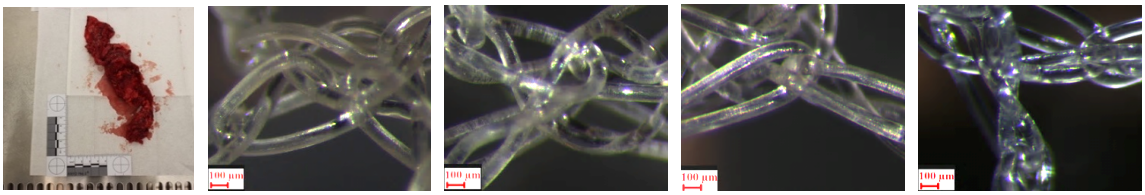

a. mesh explant | **b.** sample cleaned once | **c.** sample cleaned twice | **d.** sample cleaned three times | **e.** pristine cleaned control

Figure 3. 2. Cleaning validation.
The mesh sample was cleaned using the cleaning protocol until little improvement (image c and image d) was observed under light microscope. Mesh sample in image b was not translucent, compared to image c and d.

Change in Surface Chemistry

PP mesh surface degradation was characterized by detection of surface chemical changes on the cleaned mesh samples compared to pristine cleaned controls. Surface chemistry was measured using FTIR (IRSpirit FTIR Spectrometer, Shimadzu, Kyoto, Japan). The mesh surface was scanned in the range of 500 to 4000 cm^{-1} with resolution of 4 cm^{-1}. Compared to pristine PP mesh (Figure 3.3b), the mesh samples without surface chemical changes (Figure 3.3a, blue curve) had similar FTIR peaks, but mesh samples with surface chemical changes (Figure 3.3a, green curve) had evidence of carbonyl groups (1740 cm^{-1}) (12, 19) or hydroxyl groups (3100 – 3600 cm^{-1}) (5, 19). The observation of carbonyl groups confirmed the oxidation of the PP chain. The observation of hydroxyl groups confirmed the cross-linking of the hydrogen bonds to the PP chain (40).

Although some meshes had absorbable films before implantation, such as poliglecaprone (Figure 3.3c), the peaks (580 cm^{-1}, 725 cm^{-1} and 1081 cm^{-1}) representing poliglecaprone film was not observed in explanted mesh samples, confirmed by FTIR

(Figure 3.3d) (41). Explanted mesh sample #2 (Figure 3.3d, red curve) and #7 (Figure 3.3d, blue curve) were the same type mesh with absorbable materials (Figure 3.3c) before implantation. Both mesh samples (Figure 3.3d) were notably different from the pristine mesh samples with the intact absorbable layer (Figure 3.3c) with reduction of peaks of 580 cm^{-1}, 725 cm^{-1} and 1081 cm^{-1}. Both mesh samples (Figure 3.3d) had peaks similar as pristine PP mesh (Figure 3.3b), confirming the observation of carbonyl groups (~1740 cm^{-1}) consistent with oxidative change in the PP surface chemistry.

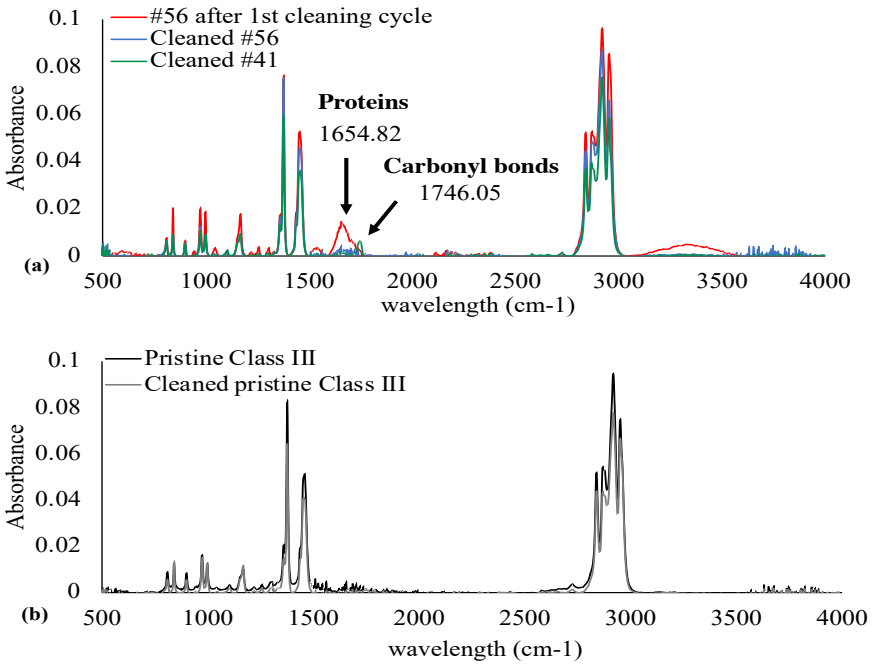

Figure 3. 3. FTIR of pristine and cleaned mesh samples.
(a) FTIR of #56 after 1 cycle of 10-step cleaning (red) and after 2 cycles of cleaning (blue), compared to cleaned #41 (green) (b) FTIR of pristine (black) and cleaned pristine PP mesh (grey).

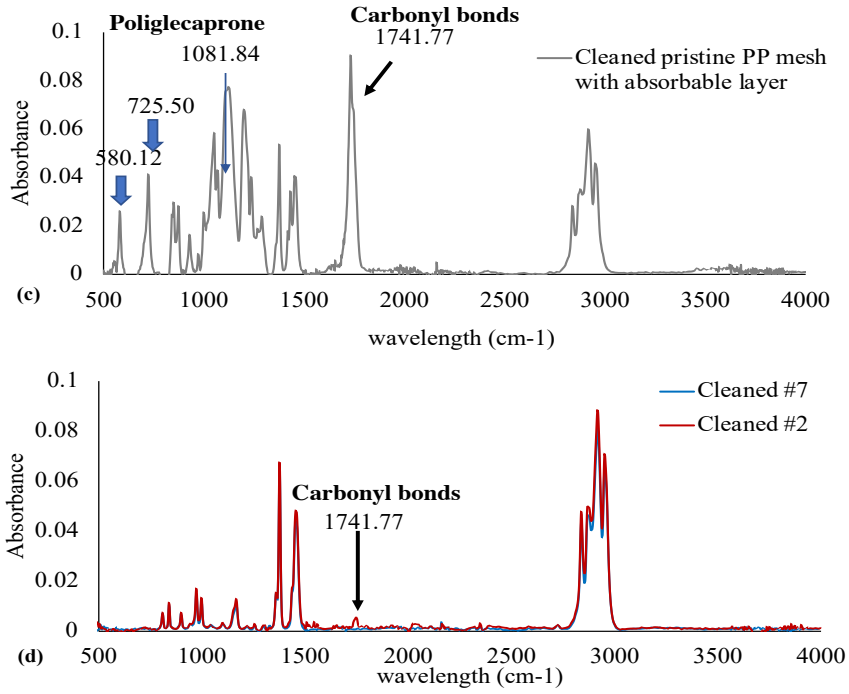

Figure 3.3. FTIR of pristine and cleaned mesh samples. (c) FTIR of cleaned pristine mesh with absorbable layer (grey) (d) FTIR of cleaned mesh samples after absorbance of absorbable layer #7 (blue) and #2 (red) after implantation.

Change in Crystallinity Characterization

PP mesh bulk degradation was characterized as the percent change in crystallinity for the cleaned explanted mesh samples compared to pristine cleaned controls. The degree of crystallinity was measured using differential scanning colorimetry (DSC) (Q1000 DSC Instrument, TA Instruments, New Castle, DE). The mesh samples were heated from 25 °C to 200 °C with heat rate of 20°C/min. The degree of crystallinity (Xc) of the mesh samples was calculated from the tested heat of fusion (H_f) to the heat of fusion of 100% crystalline polypropylene ($H_{f,100}$), which equals 209 J/g (40).

$$\text{Eq. 1: Xc} = \frac{Hf}{Hf,100\ (=209\ J/g)} \times 100\%$$

The change of crystallinity ($X_{c,changed}$) was determined by comparing to pristine cleaned controls ($X_{c,pristine}$).

Eq. 2: $X_{c,changed} = X_{c,explanted} - X_{c,pristine}$

The percent change in crystallinity was normalized relative to the crystallinity of pristine cleaned controls.

Eq. 3: $X_{c,changed}\% = \frac{X_{c,changed}}{X_{c,pristine}} \times 100\%$

Change in Stiffness Characterization

Indirect characterization of PP mesh bulk degradation was evaluated as a change in stiffness for the explanted mesh samples compared to pristine cleaned controls. Mesh stiffness was calculated from mechanical behavior measured using a biaxial tensile test (BioTester, CellScale, Ontario, Canada). The mesh samples were preconditioned by soaking in 1x PBS solution at 37°C for 15 minutes. The hydrated mesh samples were clamped on the biaxial tester equipped with orthogonal 23N load cells and a high-resolution CCD imaging system for image-based strain measurement, leaving a 2cm × 2cm region of interest. Each test sample was preconditioned by 10 cycles of cyclic stretching at a speed of 0.2 mm/s with displacement of 5% tensile strain in both directions, followed by a stretching at the same speed to peak tension (35). Due to the anisotropic behavior of some mesh samples, all tested samples were aligned according to the notable longitudinal (y direction) and transverse directions (x direction) (Appendix B) (35, 42). The mesh stiffness S_x (N/cm) and mesh stiffness S_y (N/cm) were calculated as

the slope of the linear region of the tension-strain curves. The percent change in stiffness ($S_{changed}$ %) was normalized relative to the stiffness of pristine mesh.

$$\text{Eq. 4: } S_{changed}\,\% = \frac{S_{explanted\ mesh\ sample} - S_{pristine\ mesh\ sample}}{S_{pristine\ mesh\ sample}} \times 100\%$$

Due to the limited dimensions of some explanted mesh samples, only 35 explanted meshes underwent mechanical testing and generated stiffness measures.

Statistical Analysis (43)

The patient demographics, medical conditions, surgical location, and mesh classification were independent variables (Table 3.4). The measured results were dependent variables. For patient and medical variables, sex (M/F), diabetes (Y/N), pervious hernia repair (Y/N), recurrent hernia (Y/N), infection (Y/N), and smoking status (Y/N) were dichotomous independent variables. Implantation time (months), estimated year of implantation, age (years), BMI were independent continuous variables. Surgical and mesh variables namely mesh location (intra/extra-peritoneal) and mesh class (Class I, Class II, Class III) were categorical independent variables. The measured surface chemical changes ($C_{Surface}$) (Y/N) were dichotomous dependent variables and the crystallinity changes ($X_{c,changed}$%) and stiffness changes ($S_{changed}$ %) were continuous dependent variables.

The statistical analyses were performed using JMP® Pro 14 (SAS Institute Inc, Cary, NC, USA) with 95% confidence interval for all tests. In the univariate analysis, the dependence between dependent dichotomous variables and independent dichotomous or independent categorical variables were analyzed using Chi square or Fisher's exact

depending on sample size, or Cochran Armitage trend if the categories were more than two. The relation between continuous variables and dichotomous variables were analyzed using T test or Wilcoxon rank depending on the distribution of variables. The relation between dependent continuous and independent categorical variables were tested using T test, Wilcoxon rank or One-way ANOVA with Tukey's post hoc depending on the distribution of variables and the number of categories. The correlation between dependent continuous variables and independent continuous variables were tested using Pearson or Spearman correlation.

Multivariable associations were analyzed using logistic regression models for $C_{Surface}$ and standard least squares for $X_{c,changed}\%$ and $S_{changed}$ %. All characteristics for multivariable associations were selected using a cut-off of $p \leq 0.20$ from estimated model using Adaptive Lasso with AICc Validation of all possible combined predictors.

Table 3. 4. Variables and statistical analysis methods

Independent variables	Dependent variables	Statistical analysis
Patient variables	**Measured results**	
sex (M: n = 31/ F: n = 32)	$C_{Surface}$ (Y/N)	Chi square
	$X_{c,changed}$%	T test or Wilcoxon rank
	$S_{changed}$ %	
implantation time (months) (n = 59)	$C_{Surface}$ (Y/N)	T test or Wilcoxon rank
age at removal (years) (n = 63)	$X_{c,changed}$%	Pearson or Spearman Correlation
BMI (n = 63)	$S_{changed}$ %	
Medical variables	**Measured results**	
diabetes (Y: n = 16 /N: n = 46)	$C_{Surface}$ (Y/N)	Chi square or Fisher's exact
previous hernia repair (Y: n = 44/ N: n = 18)		
infection (Y: n = 8/ N: n = 53)	$X_{c,changed}$%	T test or Wilcoxon rank
smoking (Y: n = 4/ N: n = 59)	$S_{changed}$ %	
Surgical variables	**Measured results**	
mesh location (intra: n = 24 /extra: n = 38)	$C_{Surface}$ (Y/N)	Fisher's exact
	$X_{c,changed}$%	T test or Wilcoxon rank
	$S_{changed}$ %	
Mesh variables	**Measured results**	
mesh class (Class I: n = 22, Class II: n = 23, Class III: n = 18)	$C_{Surface}$ (Y/N)	Cochran Armitage trend
	$X_{c,changed}$%	One Way ANOVA
	$S_{changed}$ %	

Results

Forty-six of the 63 FTIR tested mesh samples (73%) exhibited evidence of surface chemical changes. Twenty-one of the 62 DSC tested mesh samples (34%) exhibited crystallinity above or below the pristine control range. Thirty-five of the 35 mechanically tested mesh samples (100%) exhibited changed stiffness behavior compared to pristine control mesh.

Change in Surface Chemistry

Forty-six of the 63 tested mesh samples (73%) exhibited evidence of surface chemical changes, including 14 of 22 Class I mesh samples (63%), 18 of 23 Class II mesh samples (78%) and 14 of 18 Class III samples (78%). PP mesh surface chemical

changes were independent from mesh class (Cochran Armitage, univariate p > 0.05) and not related with patient, surgical, and medical factors (Chi square or Fisher's exact, Wilcoxon rank or T test, univariate p > 0.05) (Appendix C).

When sublay and intra-peritoneal locations were coded into same group as recoded mesh placement location, $C_{Surface}$ was dependent on recoded mesh placement location (Chi square, univariate p = 0.03) (Figure 3.4). Multivariate associations with $C_{Surface}$ were evaluated for recoded mesh placement location (univariate, p = 0.03) and recurrent hernia (univariate, p = 0.20) based on the estimated model selection from all possible combined predictors. Recoded mesh placement location (multivariate, p = 0.08) or recurrent hernia (multivariate, p = 0.26) did not affect mesh surface degradation (Table 3.5).

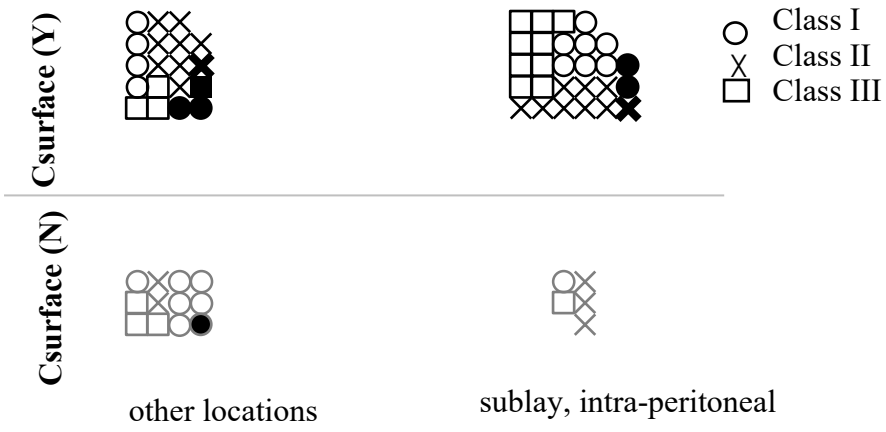

Figure 3. 4. $C_{Surface}$ (Y/N) count distribution (n = 63) based on recoded mesh placement location (sublay and intra-peritoneal vs other locations).
Each mesh was labeled according to mesh class. Eight mesh samples from infected patients were labeled as bold black.

Table 3. 5. Univariate results and multivariable associations for significant factors

Outcome	Univariate Comparison	Mean/Median	p value	Multivariate Associations	p value
$C_{Surface}$	Recoded mesh placement	Dependent	0.03*	Recoded mesh placement	0.26
	Recurrent hernia	Independent	0.20	Recurrent hernia	0.08
$X_{c,changed}$%	Mesh class	Mean $_{\text{class I}}$ = (-2.5 ± 5.1) % Mean $_{\text{class II}}$ = (4.1 ± 6.0) % Mean $_{\text{class III}}$ = (1.8 ± 8.4) %	0.004*	Mesh class	0.008*
	BMI	ρ = -0.20	0.11	BMI	0.24
	Age at removal	r = 0.27	0.03*	Age at removal	0.17
$S_{x,changed}$%	Infection	Mean $_{\text{infected}}$ = (-66.7 ± 13.4) % Mean $_{\text{no}}$ = (-36.6 ± 21.6) %	0.01*		
$S_{y,changed}$%	Infection	Mean $_{\text{infected}}$ = (-64.9 ± 16.1) % Mean $_{\text{no}}$ = (-28.1 ± 25.0) %	0.01*		

*: $p < 0.05$

Change in Crystallinity

Twenty-one of the 62 DSC tested mesh samples (34%) exhibited crystallinity above or below the pristine control range (41.9% to 50.0%) (Figure 3.5a). When normalized relative to the crystallinity of pristine mesh, 8 of the 62 samples (13%) had $X_{c,changed}$% outside 10% (Figure 3.5b), with an average decrease of 2.5% (SD: 5.1%) for Class I, increase of 4.1% (SD: 6.0%) for Class II, and increase of 1.8% (SD: 8.5%) for Class III mesh samples (Table 3.5). Mesh class was a factor affecting changed crystallinity with significantly decreased crystallinity in Class I mesh samples compared to Class II mesh samples (One-way ANOVA with post hoc, univariate $p < 0.01$) (Table 3.5). Changed crystallinity was also correlated with age at removal (Pearson, univariate $p = 0.03$) but not correlated with other patient, surgical or medical factors (T test, Spearman or Pearson, univariate $p > 0.05$).

Multivariate associations with $X_{c,changed}$% were evaluated for mesh class (univariate $p = 0.004$), BMI (univariate $p = 0.11$), and age at removal (univariate p =

0.03) based on the estimated model selection from all possible combined predictors. Mesh class was a factor significantly affecting $X_{c,changed}$% (multivariate, p = 0.008) with controlling for effects of BMI (multivariate, p = 0.24) and age at removal (multivariate, p = 0.17). The fit of the estimated model was at r^2 of 0.23.

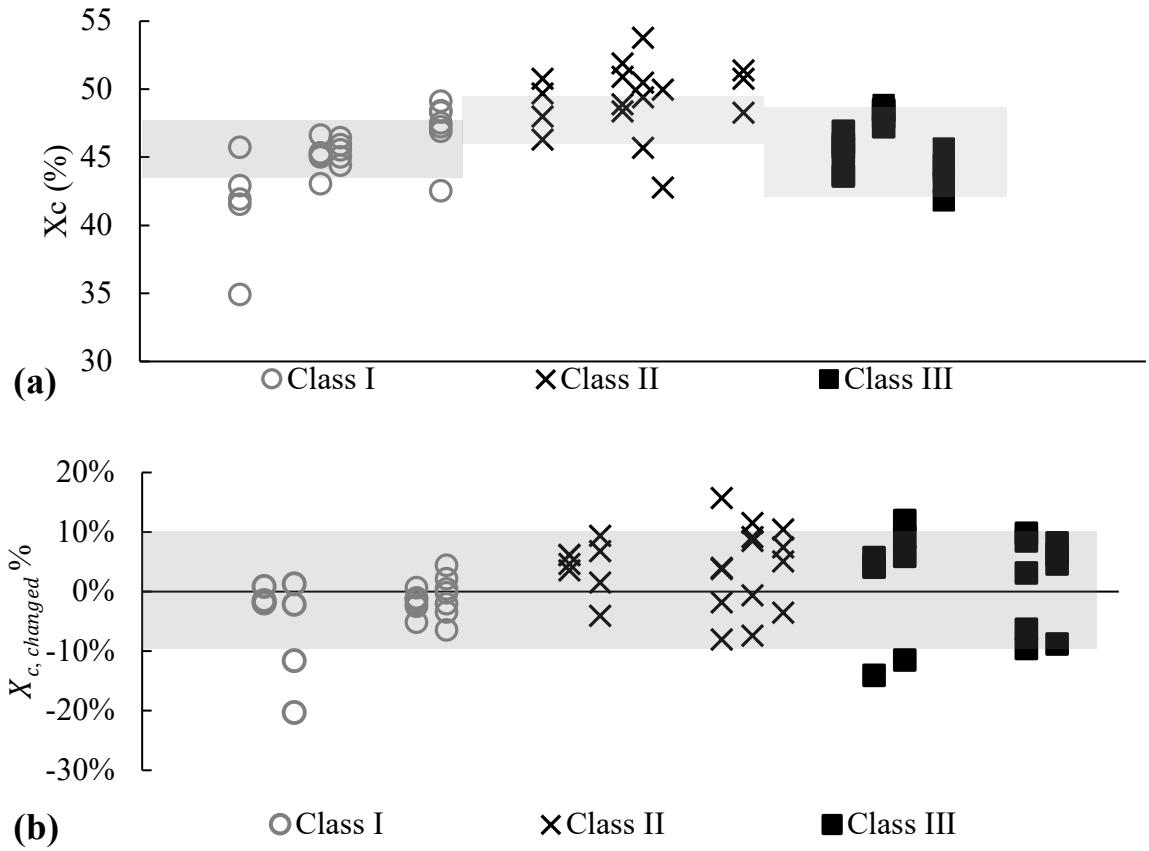

Figure 3. 5. Results of measured crystallinity (%) and calculated $X_{c,changed}$%.
(a) Measured crystallinity of all explanted mesh samples (n = 62) grouped in mesh class, compared to pristine controls (shaded area). (b) Normalized percent change in crystallinity $(X_{c,changed}\%)$ grouped in mesh class, relative to pristine controls. 10% range: shaded area.

Change in Stiffness

Thirty-five of the 35 mechanically tested mesh samples (100%) exhibited changed stiffness behavior compared to pristine control mesh. The measured stiffness of cleaned explanted mesh samples ranged from 16.3 N/cm to 145.0 N/cm in x direction and from 13.7 N/cm to 266.7 N/cm in y direction, compared to the range of pristine controls ranging from 80.7 N/cm to 158.5 N/cm in x direction and 134.9 N/cm to 265.2 N/cm in y direction (Figure 3.6a). When normalized relative to the stiffness of pristine control mesh, $S_{changed}$ % ranged from decreased 86.1% (-86.1%) to decreased 5.5% (-5.5%) in x direction and decreased 89.8% (-89.8%) to increased 4.9% (+4.9%) in y direction (Figure 3.6b). PP mesh stiffness changes in x and y directions were significantly decreased compared to pristine controls (One sample t test, univariate $p < 0.05$).

Mesh samples from infected patients had average $S_{x,changed}$% and $S_{y,changed}$% of -66.7% (SD: 13.4%) and -64.9% (SD: 16.1%), compared to mesh samples from patients without infection averaging $S_{x,changed}$% and $S_{y,changed}$% of -36.6% (SD: 21.6%) and -28.1% (SD: 25.0%) (Figure 3.7). Infection was a factor significantly affecting $S_{changed}$% in both x and y directions (T test, univariate $p = 0.01$) (Table 3.5). Changed stiffness was not related with mesh, patient, surgical and other medical factors (One-way ANOVA, T test, Pearson or Spearman, $p > 0.05$). The estimated model of all possible combined predictors for both $S_{x,changed}$% and $S_{y,changed}$% only selected infection for multivariate associations.

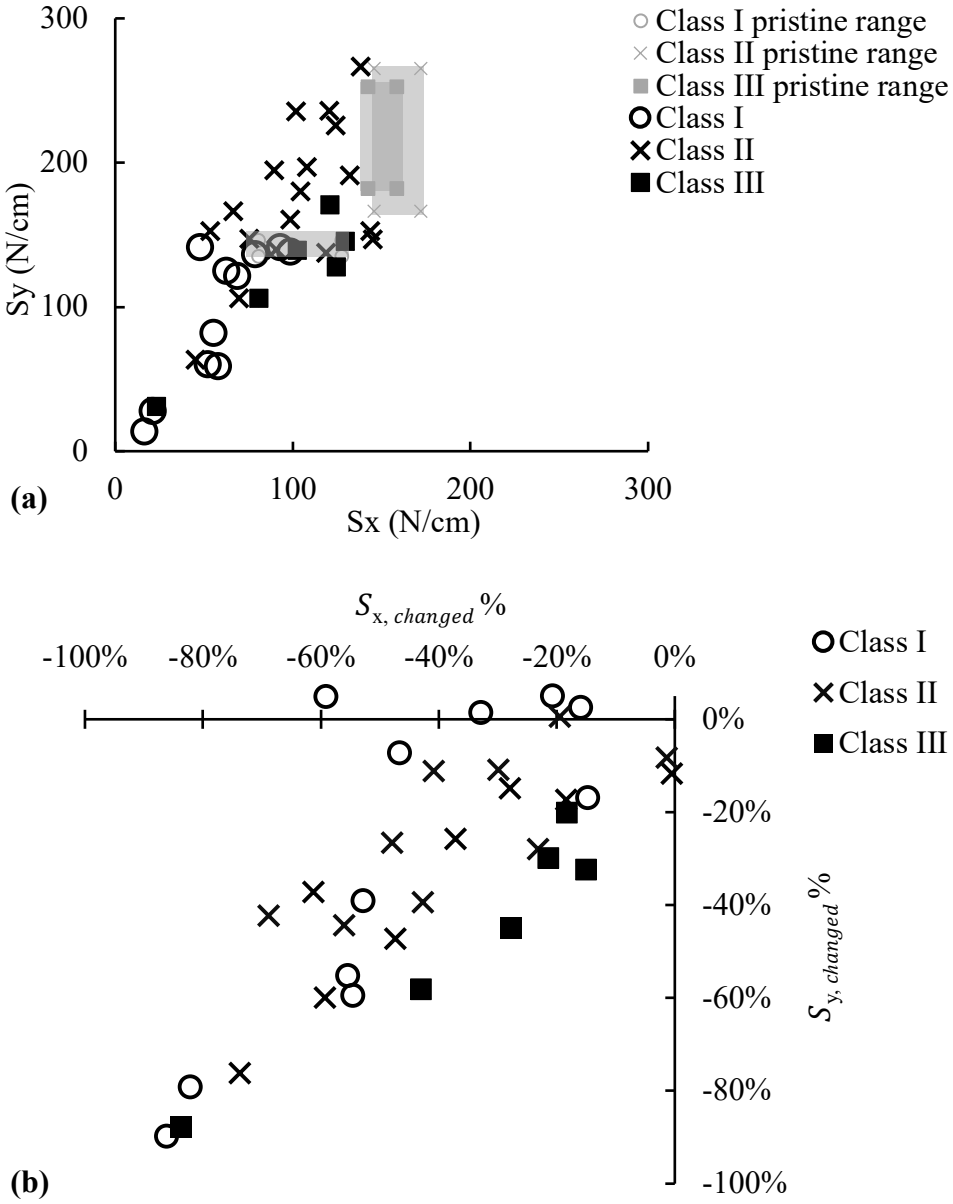

Figure 3. 6. Results of stiffness (N/cm) and calculated $S_{changed}$ %.
(a) Stiffness (S_x and S_y) of all explanted mesh samples (n = 35) grouped by mesh class, compared to pristine controls (shaded area). (b) Normalized percent change in stiffness ($S_{changed}$ %) grouped by mesh class, relative to pristine controls.

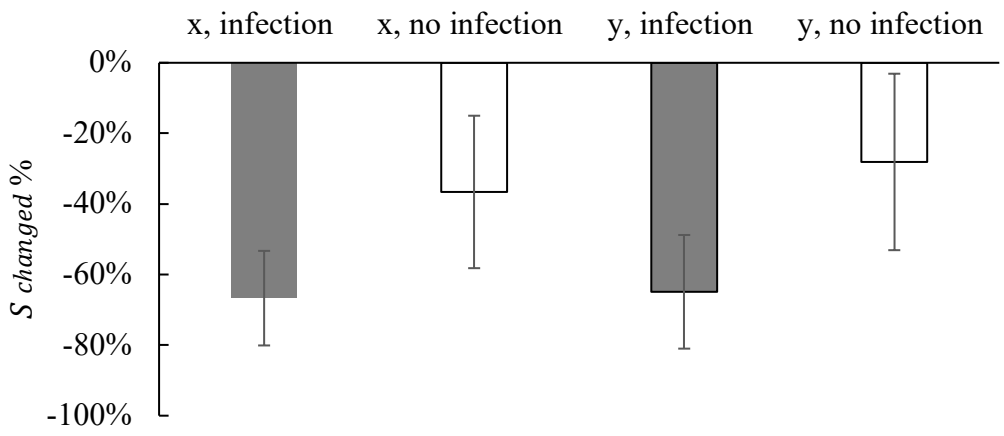

Figure 3. 7. $S_{changed}$ % of mesh samples from infected patients (n = 4) compared to mesh samples from non-infected patients (n = 30) in both x and y directions. Infection was a factor significantly affecting $S_{changed}$ % (T test, univariate p = 0.01).

Relation between Surface and Bulk Degradation

Only 35 explanted mesh samples had data from all three characterization methods (surface chemical change, crystallinity and stiffness). Surface degradation was characterized by detection of surface chemical changes. Bulk degradation was characterized by changes in crystallinity and stiffness. Mesh surface chemical change was not a factor affecting changes of crystallinity or stiffness (T test, $p > 0.05$). Twenty-four of the 35 mesh samples (69%) with surface degradation had median $X_{c,changed}$% of +4.6%, compared to +3.1% of the 11 mesh samples without surface degradation. Mesh samples with surface degradation had average $S_{x,changed}$% and $S_{y,changed}$% of -43.2% (SD: 22.5%) and -36.2% (SD: 24.6%), compared to -35.3% (SD: 23.5%) and -24.7% (SD: 29.6%) of mesh samples without surface degradation. The changed crystallinity was not correlated with the changed stiffness (Pearson, $p > 0.05$).

Discussion

This study explored mechanisms potentially contributing to PP mesh degradation using 63 explanted PP mesh samples with documentation of basic patient demographics, clinical history and details of mesh structures. The mechanisms were explored using evaluation of material changes after mesh samples were sufficiently cleaned, and analysis of multivariate associations between the material changes and clinical characteristics (Table 3.4). The material changes were characterized using surface chemistry changes, crystallinity changes, and stiffness changes consistent with chemical and physical markers cited as evidence of *in vivo* PP degradation in previous studies (6, 12-15). The findings in this study supported the proposed hypotheses that 1) infection was a factor affecting stiffness changes; 2) mesh with small pore size (mesh class) was a factor affecting crystallinity changes normalized to pristine controls. However, the study failed to support the hypotheses that 1) infection was a factor affecting surface chemistry changes and crystallinity changes; 2) mesh class was a factor affecting surface chemistry changes and stiffness changes; 3) mesh placement location was a factor affecting PP material changes.

Multivariable associations used an estimated model to evaluate the significant impact of certain independent predictors on PP mesh material changes when combining all possible predictors (43). This study confirmed the significant impact of mesh class for changes in crystallinity ($X_{c,changed}$%) when combining all possible predictors (Table 3.5), consistent with other *in vitro* and *in vivo* studies (5, 44, 45). Mesh class significantly affected $X_{c,changed}$% in both univariate (One-way ANOVA with post hoc, univariate p =

0.004) and multivariate analysis (multivariate, p = 0.008), indicating crystallinity stability was determined by mesh class even with consideration of all possible predictors. This study used $X_{c,changed}\%$ instead of Xc due to the different measured crystallinity of pristine meshes ranging from 41.9% to 50% (Figure 3.5), determined by manufacturers (5, 44). As to surface oxidation ($C_{Surface}$), although there was a trend for PP mesh surface oxidation when mesh implanted in sublay and intra-peritoneal location (Chi square, univariate p = 0.03) (Figure 3.4), $C_{Surface}$ was independent on mesh implantation location in estimated model (multivariate, p = 0.08) (Table 3.5), indicating $C_{Surface}$ was not associated with any specific predictor when considering all possible predictors. As to changes in mesh stiffness ($S_{changed}$ %), although infection was a significant factor for $S_{x,changed}\%$ and $S_{y,changed}\%$ (T test, univariate p = 0.01), it was unable to be analyzed in multivariate associations (Table 3.5), possibly due to the small sample size of only 4 mesh samples from infected patients, compared to 31 mesh samples from non-infected patients.

Evaluating explanted PP mesh material changes and their associations with clinical characteristics is important to predict the risk factors on PP mesh degradation. In this study, there were 46 of 63 explanted mesh samples (73%) with evidence of PP mesh surface chemistry changes (Figure 3.4), but only 8 of 62 explanted mesh samples (13%) had normalized crystallinity changes greater than 10%, compared to pristine controls (Figure 3.5b). Regardless of the material changes noted, none of the explanted mesh had evidence of gross mesh rupture while in clinical use. Due to the small number of

explanted mesh with evidence of material changes, it was not possible to discern whether the material changes had any impact on the clinical factors.

This study only included PP surgical mesh used for hernia repair in the abdominal wall and the results should not be generalized to represent material changes for PP surgical meshes implanted in the pelvic floor. Evidence of polymer oxidation has occurred in other implanted polymeric biomaterials and is linked to exposure to mechanical stress or an oxidizing environment (46). Different from meshes implanted in the abdomen, pelvic floor surgical meshes are exposed to higher tension and have relatively greater risk of exposure to bacteria from the outside environment (21), resulting in higher mechanical strains and accumulation of ROS due to bacterial adherence. The estimated static loadings on implanted pelvic mesh were 10.5 – 15.5 N/cm, compared to the loadings of 7.5 N/cm for implanted hernia mesh (21). Pelvic surgical mesh degradation tends to occur, due to the polymer chain scission induced by mechanical strains or the infusion of ROS, compared to hernia mesh.

Sufficient mesh cleaning is critical to avoid false observation of mesh surface oxidation associated with ineffective cleaning (10). The current study used a 10-step modified cleaning protocol (Table 3.3) and repeated cleaning cycles (Figure 3.2) to avoid interference with subsequent analysis methods. The use of enzymatic solutions instead of sodium chloride to removal tissues reduced the risk of PP oxidation due to sodium chloride (5, 47). The repeated use of enzymatic solutions assisted removing adhered proteins (10), caused by protein adsorption on the PP mesh surface after implantation (48). The use of fresh frozen explanted PP mesh instead of formalin-fixed explanted PP

mesh eliminated the formalin-fixed proteins strongly adhered to the mesh surface due to the chemical process of fixative crosslinking (3, 10, 16). Formalin-fixed proteins can have a morphology similar to PP surface cracking, which is difficult to distinguish from PP degradation under scanning electron microscopy (SEM) (10). The current study used FTIR to precisely distinguish adhered proteins and PP surface oxidation (Figure 3.3a), avoiding false observation of mesh surface cracking with SEM (9-11).

Several limitations are noted. 1) Due to the nature of implant retrieval analysis after revision surgery (47), patient selection to control the clinical and surgical factors was not possible and it was unknown if these findings can be generalized to a broader population. 2) Due to the relative short implantation time (median 24 months), material changes expected for longer *in vivo* durations should not be extrapolated from the reported data. 3) It was difficult to generalize the relationship between infection and material changes due to the small number of infection cases. 4) There was limited documentation of mesh selection at index surgery and it was unknown whether the PP mesh had absorbable components or fibers containing antioxidants. Antioxidants can alter the surface chemistry changes caused by infection or chemicals in peritoneal fluid, compared to PP monofilaments without antioxidants (3, 10). *In vivo* resorption of absorbable components in PP mesh can reduce mesh stiffness (Figure 3.6) (49) compared to mesh without absorbable component (3, 5, 45), interfering with the observation of monofilament PP mesh stiffness changes in the current study. Such *in vivo* resorption also increased the difficulty of identifying mesh types due to the same mesh structure used for

mesh with and without absorbable component, such as Proceed® and Prolene® Soft, as compared in Chapter 1.

There is a need for direct measurement of ROS *in vivo* to explore the proposed PP mesh degradation mechanism involving ROS accumulation, which are capable of PP radical scission (3, 5). In cases of infection, the immune response triggers ROS release to attack bacteria by reacting with organic molecules (17, 50-52), but ROS also exist in the process of wound healing to induce vascular endothelial growth factor expression (53) and the formation of peritoneal tissue adhesion (54). In the current study, 88% of mesh samples from infected cases and 70% of mesh sample from non-infected patients had surface oxidation (Figure 3.4), which supports the presence of ROS in both patient subsets, according to the results from other *in vitro* studies (5, 19). The direct measurement of ROS (17) assist more precise categorization of the current *in vivo* dataset.

Similarly, there is a need for estimating *in vivo* mechanical strains on mesh to explore the proposed PP mesh degradation mechanism involving mechanical strains in the mesh, which are capable of increasing localized stress and causing polymer chain scission (7, 12, 20, 21). Mechanical strains in mesh can be influenced by fibrous capsulation or scar formation (21), excess abdominal adipose tissues (55), and altered wound healing process due to diabetes or smoking (55). Mechanical strains induced by the same applied tension magnitude can also vary due to mesh knitting structures (35), as confirmed by the different stiffness ranges for pristine control mesh of different mesh classes (Figure 3.6a). Although the current study analyzed the associations between

measured material changes and comorbidities (Table 3.5), such as BMI, diabetes, smoking status, the findings could not reflect the impact of quantified mechanical strains on PP mesh degradation. The direct measurement of mechanical strains (56) could assist analyzing the statistical correlation between mesh degradation and material changes.

Conclusion

High variable *in vivo* conditions expose mesh to mechanisms that alter clinical outcomes and potentially contribute to mesh degradation. These PP mesh explants after 0.5 to 13 years *in vivo* had measurable changes in surface chemistry, crystallinity and mechanical properties, with significant trends associated with factors of mesh placement, mesh class, and infection. Using multivariate statistical approach to control for clinical characteristics, infection was a significant factor affecting mesh stiffness changes and mesh class was a significant factor affecting PP crystallinity changes. However, given the small number of infection cases presumed to represent ROS accumulation, direct measures of ROS concentrations in the peritoneal fluid before retrieval surgery are recommended to generate a direct relationship between ROS concentrations and mesh material changes. This relationship would provide an estimate of the severity of inflammatory response and potential mesh material changes during *in vivo* exposure in patients. Given that mesh structures and mesh materials are commonly modified by manufacturers or removed entirely from the market, it is recommended that material properties for pristine meshes implanted in patients should be regularly measured and reported using standard methods.

References

1. Simons MP, Aufenacker T, Bay-Nielsen M, Bouillot JL, Campanelli G, Conze J, de Lange D, Fortelny R, Heikkinen T, Kingsnorth A, Kukleta J, Morales-Conde S, Nordin P, Schumpelick V, Smedberg S, Smietanski M, Weber G, Miserez M. European Hernia Society guidelines on the treatment of inguinal hernia in adult patients. Hernia. 2009;13(4):343-403.

2. Graham J, Usher FC, Perry JL, Barkley HT. Marlex mesh as a prosthesis in the repair of thoracic wall defects. Ann Surg. 1960;151(4):469-79.

3. Liebert TC, Chartoff RP, Cosgrove SL, Mccuskey RS. Subcutaneous implants of polypropylene filaments. J Biomed Mater Res. 1976;10(6):939-51.

4. Mary C, Marois Y, King MW, Laroche G, Douville Y, Martin L, Guidoin R. Comparison of the *in vivo* behavior of polyvinylidene fluoride and polypropylene sutures used in vascular surgery. Asaio J. 1998;44(3):199-206.

5. Gil D, Rex J, Reukov V, Vertegel A. *In vitro* study on the deterioration of polypropylene hernia repair meshes. J Biomed Mater Res B. 2018;106(6):2225-34.

6. Iakovlev VV, Guelcher SA, Bendavid R. Degradation of polypropylene *in vivo*: A microscopic analysis of meshes explanted from patients. J Biomed Mater Res B. 2017;105(2):237-48.

7. Rynkevic R, Martins P, Pereira F, Ramião N, Fernandes AA. *In vitro* study of the mechanical performance of hernia mesh under cyclic loading. J Mater Sci Mater Med. 2017;28(11):1-7.

8. Imel A, Malmgren T, Dadmun M, Gido S, Mays J. *In vivo* oxidative degradation of polypropylene pelvic mesh. Biomaterials. 2015;73:131-41.

9. Thompson M, Guelcher S, Bendavid R, Iakovlev V, Ostergard DR. *In vivo* polypropylene mesh degradation is hardly a myth. Int Urogynecol J. 2017;28(2):333-5.

10. Thames SF, White JB, Ong KL. The myth: *in vivo* degradation of polypropylene-based meshes. Int Urogynecol J. 2017;28(2):285-97.

11. Thames SF, Thames SF, White JB, White JB, Ong KL, Ong KL. Reply to "*In vivo* polypropylene mesh degradation is hardly a myth". Int Urogynecol J. 2017;28(2):337-8.

12. Wood AJ, Cozad MJ, Grant DA, Ostdiek AM, Bachman SL, Grant SA. Materials characterization and histological analysis of explanted polypropylene, PTFE, and PET hernia meshes from an individual patient. J Mater Sci Mater Med. 2013;24(4):1113-22.

13. Coda A, Bendavid R, Botto-Micca F, Bossotti M, Bona A. Structural alterations of prosthetic meshes in humans. Hernia. 2003;7(1):29-34.

14. Ostergard DR. Degradation, infection and heat effects on polypropylene mesh for pelvic implantation: what was known and when it was known. Int Urogynecol J. 2011;22(7):771-4.

15. Costello CR, Bachman SL, Grant SA, Cleveland DS, Loy TS, Ramshaw BJ. Characterization of heavyweight and lightweight polypropylene prosthetic mesh explants from a single patient. Surg Innov. 2007;14(3):168-76.

16. Clavé A, Yahi H, Hammou J, Montanari S, Gounon P, Clavé H. Polypropylene as a reinforcement in pelvic surgery is not inert: comparative analysis of 100 explants. Int Urogynecol J. 2010;21(3):261-70.

17. Bardon J, Lukaszewicz A, Faivre V, Huot B, Payen D. Reactive oxygen species measure for rapid detection of infection in fluids. Ann. Intensive Care. 2016;6(1):1-8.

18. Schoen FJ, Lemons JE, Ratner BD, Hoffman AS. Biomaterials science: an introduction to materials in medicine. Burlington: Academic Press; 2013.

19. Talley AD, Rogers BR, Iakovlev V, Dunn RF, Guelcher SA. Oxidation and degradation of polypropylene transvaginal mesh. Biomater. Sci Polym Ed. 2017;28(5):444-58.

20. Li X, Kruger JA, Jor JWY, Wong V, Dietz HP, Nash MP, Nielsen PM. Characterizing the ex vivo mechanical properties of synthetic polypropylene surgical mesh. J Mech Behav Biomed Mater. 2014;37:48-55.

21. Taylor D. The failure of polypropylene surgical mesh *in vivo*. J Mech Behav Biomed Mater. 2018;88:370-6.

22. Klinge U, Klosterhalfen B, Müller M, Ottinger AP, Schumpelick V. Shrinking of Polypropylene Mesh *in vivo*: An Experimental Study in Dogs. Eur J Surg. 1998;164(12):965-9.

23. Capobianco A, Cottone L, Monno A, Manfredi AA, Rovere-Querini P. The peritoneum: healing, immunity, and diseases. J Pathol. 2017;243(2):137-47.

24. Bedaiwy MA, Falcone T. Peritoneal fluid environment in endometriosis. Clinicopathological implications. Minerva Ginecol. 2003;55(4):333-45.

25. Schlosser KA, Maloney SR, Gbozah K, Prasad T, Colavita PD, Augenstein VA, Heniford BT. The impact of weight change on intra-abdominal and hernia volumes. Surgery. 2020;167(5):876-82.

26. Cox TC, Blair LJ, Huntington CR, Colavita PD, Prasad T, Lincourt AE, Heniford BT, Augenstein VA. The cost of preventable comorbidities on wound complications in open ventral hernia repair. J Surg Res. 2016;206(1):214-22.

27. Huntington C, Gamble J, Blair L, Cox T, Prasad T, Lincourt A, Augenstein VA, Heniford BT. Quantification of the effect of diabetes mellitus on ventral hernia repair: results from two national registries. Am Surg. 2016;82(8):661-71.

28. Heniford BT, Ross SW, Wormer BA, Walters AL, Lincourt AE, Colavita PD, Kercher KW, Augenstein VA. Preperitoneal ventral hernia repair: a decade long prospective observational study with analysis of 1023 patient outcomes. Ann Surg. 2020;271(2):364-74.

29. Lake SP, Ray S, Zihni AM, Thompson Jr. DM, Gluckstein J, Deeken CR. Pore size and pore shape – but not mesh density – alter the mechanical strength of tissue ingrowth and host tissue response to synthetic mesh materials in a porcine model of ventral hernia repair. J Mech Behav Biomed Mater. 2015;42:186-97.

30. Klinge U, Klosterhalfen B, Birkenhauer V, Junge K, Conze J, Schumpelick V. Impact of Polymer Pore Size on the Interface Scar Formation in a Rat Model. J Surg Res. 2002;103(2):208-14.

31. Klosterhalfen B, Klinge U. Retrieval study at 623 human mesh explants made of polypropylene - impact of mesh class and indication for mesh removal on tissue reaction. J Biomed Mater Res B. 2013;101(8):1393-9.

32. Klosterhalfen B, Junge K, Klinge U. The lightweight and large porous mesh concept for hernia repair. Expert Rev Med Devices. 2005;2(1):103-17.

33. Klinge U, Park J, Klosterhalfen B. The Ideal Mesh? Pathobiology. 2013;80(4):169.

34. Weyhe D, Cobb W, Lecuivre J, Alves A, Ladet S, Lomanto D, Bayon Y. Large pore size and controlled mesh elongation are relevant predictors for mesh integration quality and low shrinkage--Systematic analysis of key parameters of meshes in a novel minipig hernia model. Int J Surg. 2015;22:46-53.

35. Deeken CR, Thompson J,Dominic M., Castile RM, Lake SP. Biaxial analysis of synthetic scaffolds for hernia repair demonstrates variability in mechanical anisotropy, non-linearity and hysteresis. J Mech Behav Biomed. 2014;38:6-16.

36. Casey EM. Physical characterization of surgical mesh after function in hernia repair [dissertation]. ProQuest Dissertations Publishing; 2015.

37. Halligan S, Parker SG, Plumb AA, Alastair C J Windsor. Imaging complex ventral hernias, their surgical repair, and their complications. Eur Radiol. 2018:1-10.

38. Klinge U, Klosterhalfen B. Modified classification of surgical meshes for hernia repair based on the analyses of 1,000 explanted meshes. Hernia. 2012;16(3):251-8.

39. Cotton B. Quantitative histological analysis of fixation points on explanted hernia mesh [dissertation]. ProQuest Dissertations Publishing; 2018.

40. Gil D. Naturally derived anti-inflammatory and antibacterial coatings for surgical implants [dissertation]. ProQuest Dissertations Publishing; 2017.

41. Patel HN, Garcia R, Schindler C, Dean D, Pogwizd SM, Singh R, Vohra YK, Thomas V. Fibro-porous poliglecaprone/polycaprolactone conduits: synergistic effect of composition and *in vitro* degradation on mechanical properties. Polym Int. 2015;64(4):547-55.

42. Eaton C, Lu X, Jallepalli R, Harman M. Characterization of anisotropic behavior and biaxial strain distribution in polymeric surgical mesh. BMES Annual Meeting. 2019 October.

43. Cavallo JA, Roma AA, Jasielec MS, Ousley J, Creamer J, Pichert MD, Baalman S, Frisella MM, Matthews BD, Deeken CR. Remodeling characteristics and collagen distribution in synthetic mesh materials explanted from human subjects after abdominal wall reconstruction: an analysis of remodeling characteristics by patient risk factors and surgical site classifications. Surg Endosc. 2014;28(6):1852-65.

44. Afonso JS, Jorge R, Martins PS, Soldi MD, Alves OL, Patricio B, Mascarenhas T, Sartori MG, Girao MJ. Structural and thermal properties of polypropylene mesh used in treatment of stress urinary incontinence. Acta Bioeng Biomech. 2009;11(3):27-33.

45. Costello CR, Bachman SL, Ramshaw BJ, Grant SA. Materials characterization of explanted polypropylene hernia meshes. J Biomed Mater Res B. 2007;83B(1):44-9.

46. Currier BH, Van Citters DW, Currier JH, Carlson EM, Tibbo ME, Collier JP. *In vivo* oxidation in retrieved highly crosslinked tibial inserts. J Biomed Mater Res B. 2013;101B(3):441-8.

47. Zhang Z, Guidoin R, King MW, How TV, Marois Y, Laroche G. Removing fresh tissue from explanted polyurethane prostheses - which approach facilitates physicochemical analysis. Biomaterials. 1995;16(5):369-80.

48. Hlady V, Buijs J. Protein adsorption on solid surfaces. Curr Opin Biotechnol. 1996;7(1):72-7.

49. Cobb WS, Burns JM, Peindl RD, Carbonell AM, Matthews BD, Kercher KW, Heniford BT. Textile analysis of heavy weight, mid-weight, and light weight polypropylene mesh in a porcine ventral hernia model. J Surg Res. 2006;136(1):1-7.

50. Heinzelmann M, Simmen HP, Battaglia H, Friedl HP, Trentz O. Inflammatory response after abdominal trauma, infection, or intestinal obstruction measured by oxygen radical production in peritoneal fluid. Am. J. Surg. 1997;174(4):445-7.

51. Kolaczkowska E, Kubes P. Neutrophil recruitment and function in health and inflammation. Nat. Rev. Immunol. 2013;13(3):159-75.

52. Segal AW. How neutrophils kill microbes. Annu Rev Immunol. 2005;23(1):197-223.

53. Sen CK, Khanna S, Babior BM, Hunt TK, Ellison EC, Roy S. Oxidant-induced vascular endothelial growth factor expression in human keratinocytes and cutaneous wound healing. J Biol Chem. 2002;277(36):33284-90.

54. Roy S, Clark CJ, Mohebali K, Bhatt U, Wallace WA, Nahman NS, Nahman NS, Ellison EC, Melvin WS, Sen CK. Reactive oxygen species and egr-1 gene expression in surgical postoperative peritoneal adhesions. World J Surg. 2004;28(3):316-20.

55. Novitsky YW, Orenstein SB. Effect of patient and hospital characteristics on outcomes of elective ventral hernia repair in the United States. Hernia. 2013;17(5):639-45.

56. Kuehnert N, Kraemer NA, Otto J, Donker HCW, Slabu I, Baumann M, Kuhl CK, Klinge U. *In vivo* MRI visualization of mesh shrinkage using surgical implants loaded with superparamagnetic iron oxides. Surg Endosc. 2011;26(5):1468-75.

CHAPTER FOUR

UNDERSTANDING MECHANISMS OF POLYPROPYLENE HERNIA MESH DEGRADATION USING EXPERIMENTAL SIMULATIONS

Introduction

Polypropylene (PP) biomaterials are widely implanted as hernia mesh due to their chemical stability, high tensile strength and mechanical flexibility. However, it is debated whether PP mesh degrades *in vivo* (1-4), which identifies a critical need to understand possible mechanisms of PP mesh *in vivo* degradation. Studies suggest that mechanisms of PP mesh *in vivo* degradation may be related to exposure to reactive oxygen species (ROS) and mechanical strains (1, 4, 5).

One proposed mechanism involves highly oxidative chemicals (ROS and myeloperoxidase) that are present in cases of infection and chronic inflammation in tissues adjacent to biomaterials (6) and in peritoneal fluid (5, 7, 8). These chemicals are capable of oxidizing PP, as a result of chain branching or chain scission of the PP, decreasing crystallinity and leading to more surface cracking. Another proposed mechanism involves the constant and cyclic mechanical strains that exist during the surgical procedure and healing process and with patient activities after mesh implantation (1, 9, 10). Mechanical strains *in vivo* caused by abdominal pressure and tissue integration can lead to expansion or shrinkage in the overall mesh size (11-14), changes in pore size (15), and adverse effects due to fibrotic tissue adhesion (16, 17). The applied mechanical strains can initiate cracks (18), resulting in surface cracking, brittleness, and an overall loss of flexibility (4, 19-22), as evidence of PP degradation.

It is unlikely that each mechanism alone will result in severe degradation (1) in a biological environment filled with fluids containing various chemicals (18). PP mesh degradation may be caused by the synergistic effect of ROS and mechanical strains. When exposing mesh to both ROS and mechanical strain, ROS may penetrate into the PP fiber through the free volumes or surface cracking caused by mechanical strains (18), increasing the potential for chain scission and cross-linking by chemical reaction. When considered in the extreme, the synergistic effect of ROS and mechanical strain could eventually lead to PP fiber rupture. However, the concentration of ROS is highly variable in the physiological environment (5) and its impact on PP mesh implants is poorly defined.

There is a critical need to understand possible mechanisms that potentially degrade PP mesh *in vivo*. The purpose of this study was to define a physiological continuum of ROS concentration associated with chronic inflammation/infection and estimate the synergistic impact of varied ROS concentration and mechanical strains on PP mesh degradation using *in vitro* simulation. This study hypothesizes that: 1) higher ROS concentrations would result in greater PP mesh degradation, as evidenced by changes in surface appearance, oxidation, crystallinity, and stiffness; and 2) the synergistic effect of ROS and mechanical strains would lead to greater PP degradation than either mechanism alone.

Materials

Meshes

Unopened packages of unexpired large pore PP mesh (LP) (Prolene® Soft) (2, 23), unexpired composite small pore PP mesh (SP) (5, 23, 24) and expired composite small pore PP mesh (ESP) (Composix™ E/X) (Table 4.1) were acquired. The ePTFE films of SP and ESP were removed, leaving PP meshes for experimental simulation. Meshes were cut into 4 cm × 4 cm samples for *in vitro* studies of soaking in simulated solutions without applied mechanical strains, or 10 cm × 10 cm samples for *in vitro* studies of soaking in simulated solutions with applied mechanical strains. Meshes before soaking in any chemicals were used as pristine controls (PC).

Table 4. 1. Mesh information before soaking

Mesh	Material	Structures	Mesh Class	Porosity	PP crystallinity
LP	PP	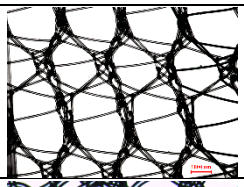	I	67%	48.3%
SP	PP sewn to ePTFE film	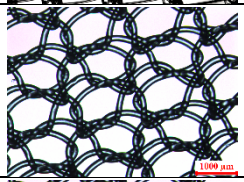	III	46%	47.6%
ESP	PP sewn to ePTFE film	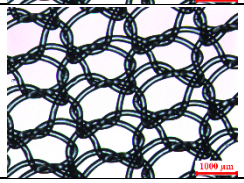	III	46%	49.4%

Simulated Chemical Solutions

The ROS solutions were simulated using 35% hydrogen peroxide (H_2O_2) (ThermoFisher Scientific, Ward Hill, MA) and cobalt chloride ($CoCl_2$) (Sigma-Aldrich,

St. Louis, MO) (25). The control solutions were simulated using phosphate buffer saline (PBS) (ThermoFisher Scientific, Ward Hill, MA). Three different ROS concentrations were simulated: high ROS concentration (HROS), low ROS concentration (LROS), and without ROS (PBS). ROS concentrations in previous studies used to oxidize PP meshes were simulated using 20wt% H_2O_2 (6.29 M H_2O_2) (26-28) or 1.63M H_2O_2 (5). Considering 1.63M H_2O_2 as 1x ROS, 4x ROS was 6.52M H_2O_2, similar to 20wt% H_2O_2. Based on that assumption, the HROS solution was simulated using 6.52M H_2O_2 catalyzed with 0.05 M $CoCl_2$ (6.52M H_2O_2/ 0.05M $CoCl_2$) and the LROS solution was simulated using 1.63M H_2O_2 catalyzed with 0.05M $CoCl_2$ (1.63M H_2O_2/ 0.05M $CoCl_2$) (25). The PBS solution was simulated using 0.01 M PBS at pH 7.4.

Simulated Mechanical Strains

The mechanical strains (MS) on mesh were simulated using abdominal wall simulators (Figure 4.1) (29). A 10 cm × 10 cm mesh sample was placed and secured between two plates above an open circle area of 6.3 cm diameter (Figure 4.1). The open circle was used for mesh movement when air was purged into the system. The open circle was sealed by placing and securing two layers of thin latex resistance bands (Stamina Products, Springfield, MO) at 10 cm (length) × 10 cm (width) × 0.045 cm (thickness) below the inserted mesh sample. When air was purged into the system, mesh movement was achieved due to the movement of the resistance bands with modulus of 2.47 ± 0.09 MPa (29, 30). The applied mechanical strain on each inserted mesh sample was monitored using the pressure gauge (Figure 4.1). The purged air pressure was maintained at 1.6 ± 0.2 psi, resulting in mechanical strains at approximately 5% based on the arc

length of the pressurized resistance bands (66 mm) relative to the original length when unpressurized (63 mm). Silicon grease (Dow Corning®, Midland, MI) was carefully applied to seal the gaps between each simulator component to avoid leaking without contaminating the inserted mesh samples.

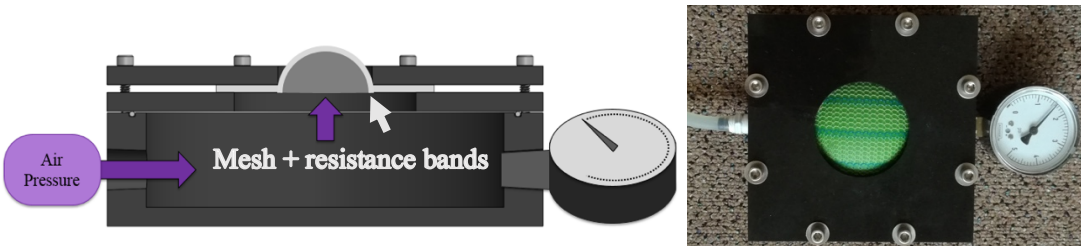

Figure 4. 1. Abdominal wall simulator with constantly purging air into the system (29).

Experimental Design

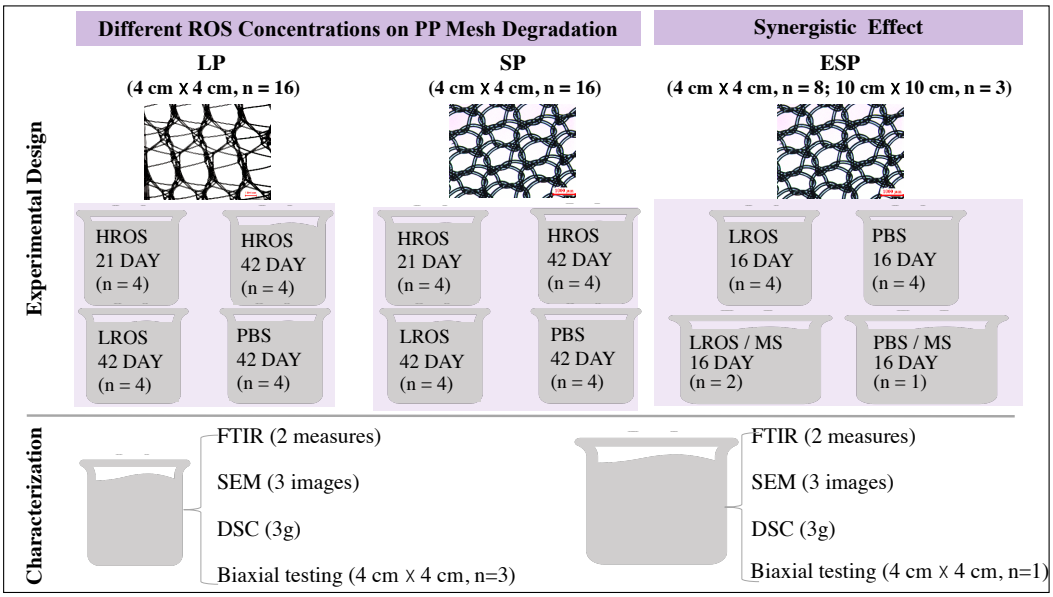

Figure 4. 2. Experimental design overview.

Different ROS Concentrations on PP Mesh Degradation

Four samples of LP and SP were soaked in three different solutions: HROS, LROS and PBS (Figure 4.2). Mesh samples were wrapped inside glass wool (ThermoFisher Scientific, Ward Hill, MA) and then the glass wool was added to the solution to enhance interactions between the solution and the meshes (Figure 4.3) (25). The solutions were kept at 37 °C for 42 days and replaced every 3 to 4 days to maintain H_2O_2 concentrations, and the glass wool was changed every month to maintain the enhancement of interaction. Mesh samples (n = 4 meshes of each type per condition) were rinsed and vacuum dried for material characterization: HROS/21day, HROS/42day, LROS/42day and PBS/42day (Figure 4.2).

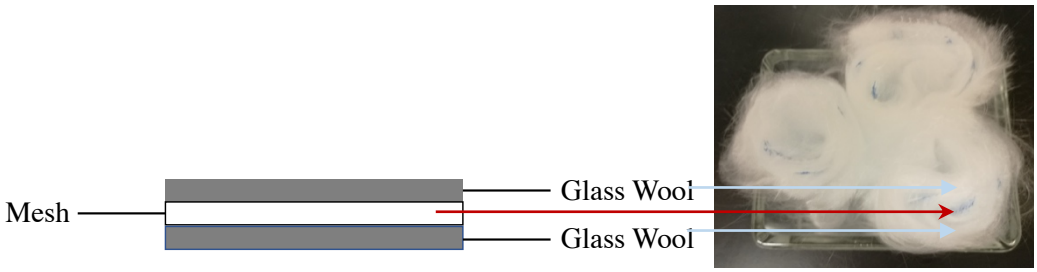

Figure 4. 3. Mesh sample set-up in simulated solutions.

Synergistic Effect of ROS and Mechanical Strains on PP Mesh Degradation

Mesh samples in LROS/MS and PBS/MS were inserted in the abdominal wall simulators (Figure 4.1) in the same orientation. Each simulator was suspended over a glass petri dish containing simulated solution to soak the exposed 6.3 cm diameter mesh sample in the simulated solution (Figure 4.4). Glass wool was added above and below each mesh to enhance interactions between the solution and the mesh (Figure 4.3). The simulators with inserted mesh samples and simulated solutions were kept at 50 °C. The

solutions, latex resistance bands and the glass wool next to the latex resistance bands were replaced every 3 to 4 days to maintain elasticity of the latex resistance bands with at least 75% strength in that timeframe. The high temperature facilitated the PP degradation with surface oxidation observed at Day 16. All mesh samples (LROS/16 day, PBS/16day, LROS/MS and PBS/MS) were rinsed and vacuum dried for material characterization at Day 16.

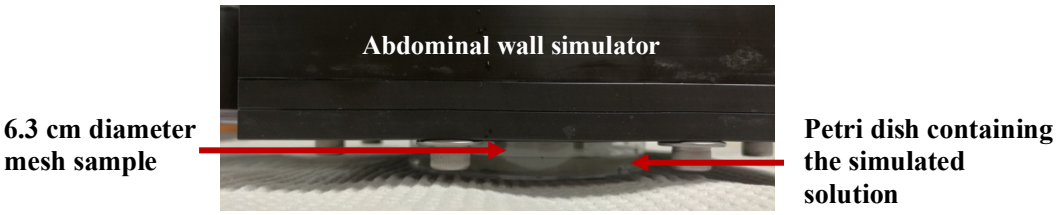

Figure 4. 4. Mesh sample set-up with applied mechanical strains.

Material Characterization

Fourier Transform Infrared Spectroscopy (FTIR)

Surface chemical changes ($C_{surface}$) for LP, SP, ESP mesh samples in their four simulated conditions (Figure 4.2) were characterized and compared to PC mesh samples using FTIR scans from 500 to 4000 cm^{-1} with a resolution of 4 cm^{-1} (Thermo-Nicolet Magna 550, ThermoFisher Scientific, Ward Hill, MA). Two measures were collected using one mesh sample for each simulated condition. Surface oxidation ($C_{surface}$ (Y)) was confirmed by the presence of peaks at 1740 cm^{-1} corresponding to the carbonyl groups (C=O) (19) or 3100 – 3600 cm^{-1} corresponding to hydroxyl groups (–OH) (31). Peaks for carbonyl groups confirmed oxidation of the PP chain and peaks for hydroxyl groups confirmed cross-linking of hydrogen bonds to the PP chain (5).

Scanning electron microscopy (SEM)

Surface defects ($D_{surface}$) on the fibers for LP, SP, ESP mesh samples in their four simulated conditions (Figure 4.2) were characterized and compared to PC mesh samples using SEM (Hitachi S3400, Hitachi, Tokyo, Japan). Three different images were captured using one mesh sample for each condition. Mesh samples were sputter coated with platinum and imaged at an accelerating voltage of 20 kV and magnifications up to 1000x (5). Evidence of surface changes compared to PC mesh samples confirmed the presence of surface defects ($D_{surface}$ (Y)).

Differential Scanning Calorimetry (DSC)

Changes in crystallinity for LP, SP, ESP mesh samples in their four simulated conditions (Figure 4.2) were characterized and compared to PC mesh samples using DSC (Q1000, TA Instruments, New Castle, DE) from room temperature up to 200 °C with a heat rate of 20 °C/min. Approximately 3 grams of one mesh sample from each condition were characterized. The degree of crystallinity (Xc) was calculated from the ratio of the measured heat of fusion ($Hf, 100$) to the heat of fusion of 100% crystalline PP, which equals 209 J/g: $Xc = \frac{Hf}{Hf,100\ (=209\ \mathrm{J/g})} \times 100\%$. The change of crystallinity was compared to PC mesh samples.

Mechanical Testing

Changes in stiffness for LP, SP, ESP mesh samples in their four simulated conditions (Figure 4.2) were characterized and compared to PC mesh samples using a biaxial test rig (BioTester, CellScale, Ontario, Canada), equipped with 23N load cells and

a high-resolution CCD imaging system for image-based strain measurement. Three mesh samples were tested for each condition except LROS/MS and PBS/MS. Due to the limited mesh sample size (6.3cm diameter circle) with mechanical strains, only one tested sample was available for mechanical testing. Two ESP mesh samples for LROS/MS and one ESP mesh sample for PBS/MS were tested. Each tested sample was cut to 3 cm × 3 cm, mounted to produce a 2 cm × 2 cm region of interest, and stretched at a speed of 0.2 mm/s in both directions to 10% strain to protect the load cell (32). Due to the anisotropic behavior of some mesh samples, all tested samples were aligned in the same orientations according to the notable longitudinal and transverse directions (Appendix B) (32, 33) and verified by images captured by Cellscale. The mesh biaxial stiffness S_x (N/cm) and S_y (N/cm) was calculated as the slope of the linear region of the tension-strain curves. The change of stiffness in each direction was compared to PC mesh samples.

Statistical Analysis

The statistical analyses were performed using JMP® Pro 14 (SAS Institute Inc, Cary, NC, USA) with 95% confidence interval for all tests. The simulated conditions were categorical independent variables (HROS/21day, HROS/42day, LROS/42day, PBS/42day; LROS/16 day, PBS/16day, LROS/MS, PBS/MS) (Table 4.2). The measured results were dependent variables. The measured $C_{surface}$ (Y/N) and $D_{surface}$ (Y/N) were dichotomous variables. The measured Xc, S_x and S_y were continuous variables. There was only one Y/N result for the each measured dichotomous variable in each condition, meaning there was no difference between Y and Y, or N and N when different conditions were compared. There was only one measured Xc for each condition and therefore, Xc

was not statistically analyzed. There were three measured S_x and three measured S_y for HROS/21day, HROS/42day, LROS/42day, PBS/42day, LROS/16 day, PBS/16day and PC mesh samples. The impact of the independent variables on S_x and $S_y$were analyzed using One-way ANOVA with Tukey's post hoc.

Table 4. 2. Variables and statistical analysis methods

Mesh	Independent Variables	Dependent Variables	Measures	Statistical Analysis
LP	Different ROS concentrations (HROS/21day, HROS/42day, LROS/42day, PBS/42day)	$C_{surface}$ (Y/N)	2	–
		$D_{surface}$ (Y/N)	3	–
		Xc	1	–
		S	3	One-way ANOVA
SP	Different ROS concentrations (HROS/21day, HROS/42day, LROS/42day, PBS/42day)	$C_{surface}$ (Y/N)	2	–
		$D_{surface}$ (Y/N)	3	–
		Xc	1	–
		S	3	One-way ANOVA
ESP	Synergistic effect (LROS/16 day, PBS/16day, LROS/MS, PBS/MS)	$C_{surface}$ (Y/N)	2	–
		$D_{surface}$ (Y/N)	3	–
		Xc	1	–
	LROS/16 day, PBS/16day, PC	S	3	One-way ANOVA

Results

Higher ROS concentrations did not result in greater PP mesh changes in surface appearance, oxidation, crystallinity, and stiffness (Figure 4.5). The synergistic effect of ROS and mechanical strains did not lead to greater PP mesh changes in surface appearance, oxidation, crystallinity and stiffness than either mechanism alone.

	Different ROS Concentrations on PP Mesh Degradation				Synergistic Effect	
PC	LP		SP		ESP	
Xc	48.3%		47.6%		49.4%	
Sx (N/cm)	130.5 ± 5.5		90.3 ± 3.5		108.2 ± 12.4	
Sy (N/cm)	136.8 ± 4.3		184.0 ± 13.7		176.8 ± 16.2	
	HROS 21 DAY	HROS 42 DAY	HROS 21 DAY	HROS 42 DAY	LROS 16 DAY	PBS 16 DAY
Csurface	**Y**	N	N	N	**Y**	N
Dsurface	**Y**	**Y**	N	**Y**	**Y**	N
Xc	50.3%	50.1%	47.6%	48.4%	54.1%	47.6%
Sx (N/cm)	127.2 ± 6.1	128.8 ± 16.0	86.2 ± 10.4	93.8 ± 10.1	104.2 ± 4.2	102.4 ± 7.1
Sy (N/cm)	141.6 ± 2.1	146.5 ± 12.3	172.5 ± 17.2	184.5 ± 15.0	180.7 ± 2.9	176.9 ± 15.4
	LROS 42 DAY	PBS 42 DAY	LROS 42 DAY	PBS 42 DAY	LROS/MS 16 DAY	PBS/MS 16 DAY
Csurface	**Y**	N	**Y**	N	N	N
Dsurface	**Y**	N	**Y**	N	**Y**	N
Xc	50.3%	48.2%	48.6%	48.0%	46.5%	47.5%
Sx (N/cm)	137. 6 ±14.6	138.4 ± 3.2	93.9 ± 10.9	90.9 ± 14.4	97.9 ± 1.8	108.9
Sy (N/cm)	146.6 ± 11.8	142.6 ± 3.9	183.4 ± 18.1	192.0 ± 31.9	177.8 ± 4.3	212.6

Figure 4. 5. Overview of measured results.

FTIR

Greater PP mesh surface oxidation was not related with higher ROS concentrations, as evidence of $C_{surface}$ (N) for both LP and SP mesh samples in condition of HROS/42day, compared to $C_{surface}$ (Y) in LROS/42day. PP mesh surface oxidation was not related with synergistic effect of ROS and mechanical strains, as evidence of $C_{surface}$ (N) for ESP mesh samples in condition of LROS/MS, compared to $C_{surface}$ (Y) in LROS/16day.

The FTIR spectra for three PC mesh samples was similar. Peaks at 1740 cm^{-1} or in the range of 3100 – 3600 cm^{-1} ($C_{surface}$ (Y)) were observed in LP mesh samples in conditions of HROS/21day and LROS/42day, in SP mesh samples in LROS/42day, and in ESP mesh samples in LROS/16 day compared to PC mesh samples (Figure 4.5). Although $C_{surface}$ (Y) was observed in LP mesh samples in HROS/21day condition,

$C_{surface}$ (N) was observed in HROS/42day, confirming the instability of HROS on PP mesh degradation.

No peaks representing PP degradation was observed for ESP mesh samples in condition of PBS/16day, confirming PP surface was stable at 50 °C (Figure 4.6). Silicon grease was observed for ESP mesh samples in LROS/MS and PBS/MS (Figure 4.6), which was used for sealing the simulators. The contamination was caused by the gravity and high temperature, dissolving the silicon grease into the solution, which interfered the FTIR readings due to its protection on PP surface from being oxidized.

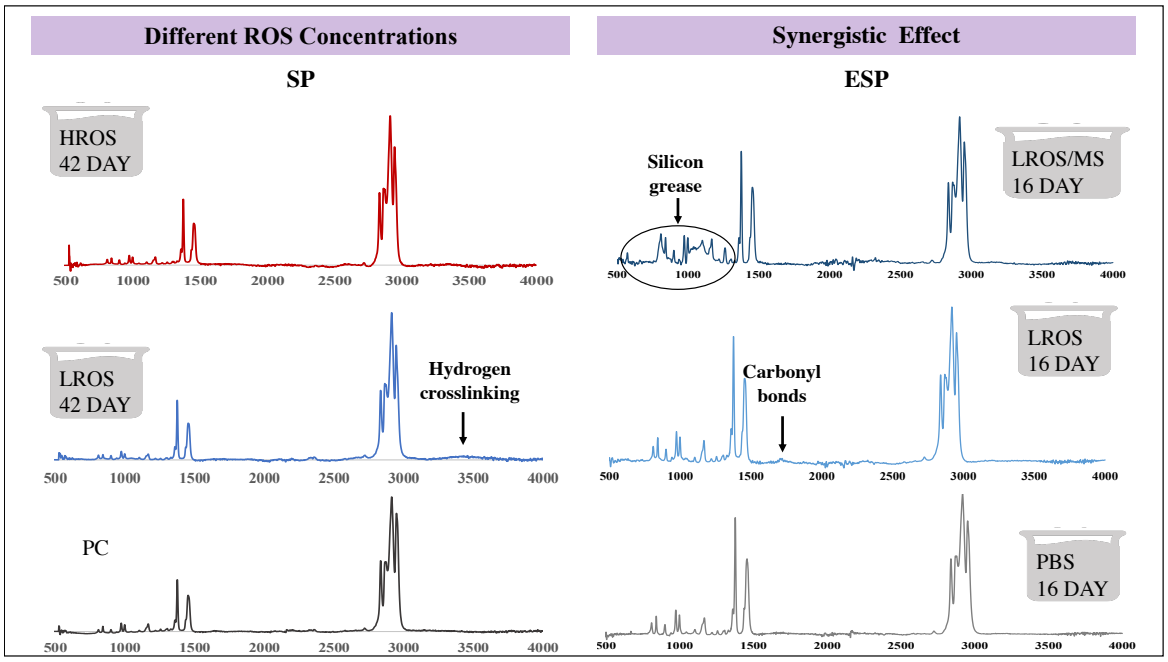

Figure 4. 6. FTIR results of SP and ESP mesh samples in different conditions. The FTIR reuslts for LP mesh samples were not included due to the same spectra as SP results.

SEM

The impact of different ROS concentrations on PP mesh surface appearance change was not detectable, due to the evidence of $D_{surface}$ (Y) for both LP and SP mesh

samples in conditions of HROS/42day and LROS/42day (Figure 4.7). Similarly, the relation between PP mesh surface appearance change and synergistic effect of ROS and mechanical strains was not detectable, due to the evidence of $D_{surface}$ (Y) for ESP mesh samples in both conditions of LROS/MS and LROS/16day (Figure 4.7).

The surface appearance for three PC mesh samples was similar, with lack of surface damage recorded as $D_{surface}$ (N). $D_{surface}$ (Y) was observed for LP mesh samples in conditions of HROS/21day, HROS/42day and LROS/42day, for SP mesh samples in condition of HROS/42day and LROS/42day, and for ESP mesh samples in conditions of LROS/16 day and LROS/MS (Figure 4.5), confirming changes in the PP surface appearance was induced by ROS. $D_{surface}$ (N) was observed for PBS/MS, confirming low mechanical strain (5%) did not affect PP surface appearance.

The $D_{surface}$ (Y) was in the form of small spots scattered on the surface, similar to mesh after reserialization (34), which was possibly induced by the heat released by the chemical reaction of H_2O_2 catalyzed with 0.05 M $CoCl_2$. Although narrow surface cracking along the fiber direction was observed for all mesh samples, the cracking was not induced by oxidizing chemicals. Instead, similar cracking was observed in pristine mesh samples in other studies (24, 34).

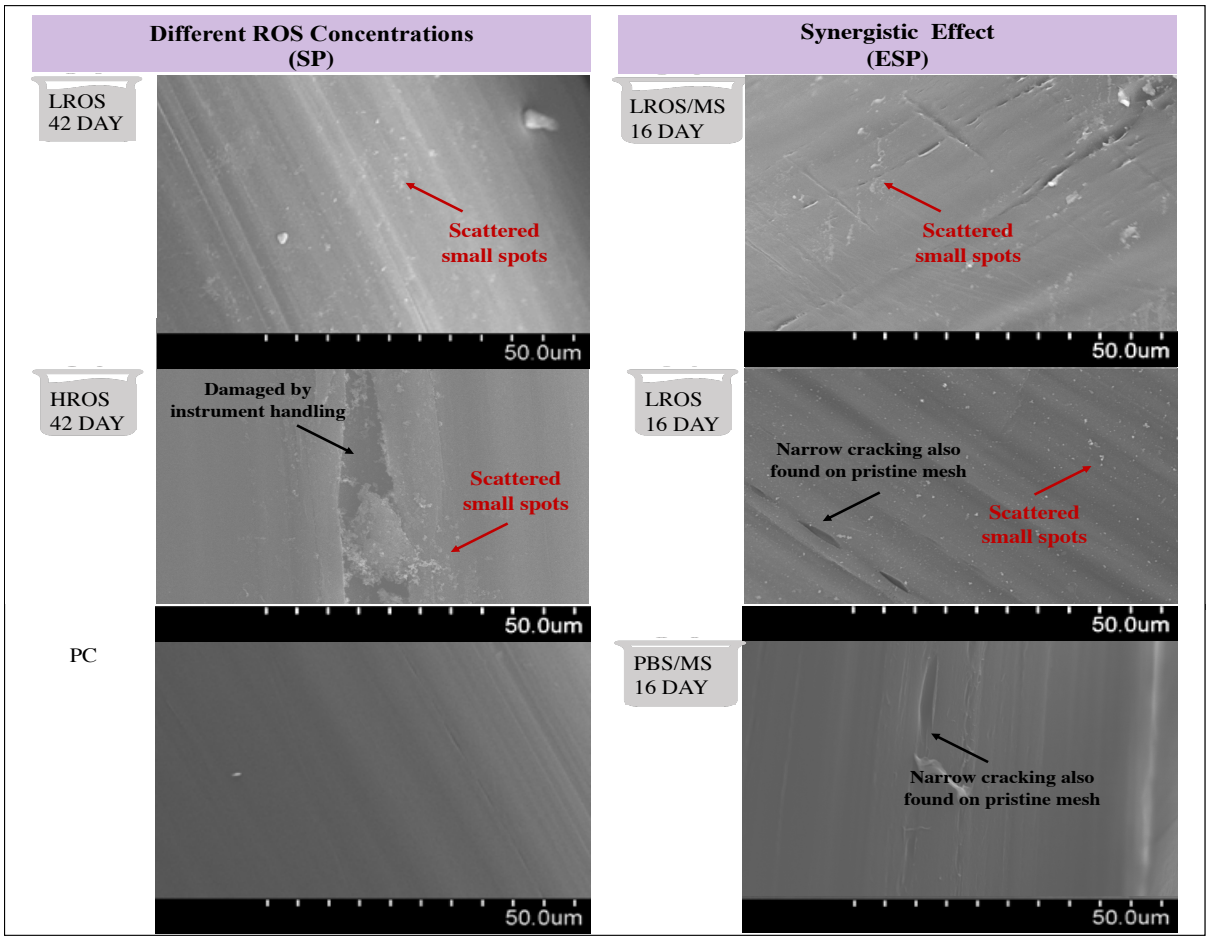

Figure 4. 7. SEM results of SP and ESP mesh samples in different conditions. The SEM results for LP mesh samples were not included due to the same images as SP results.

DSC

PP mesh crystallinity was not related with different ROS concentrations due to the crystallinity of LP and SP mesh samples in all conditions within 5% range variation of PC mesh samples. PP mesh crystallinity was not related with synergistic effect due to the crystallinity of LROS/MS within 3% variation compared to PBS/MS (Figure 4.8).

There was a trend for increased crystallinity for ESP mesh samples exposed to ROS and for decreased crystallinity for ESP mesh samples exposed to mechanical strains.

The crystallinity for ESP mesh samples exposed to LROS/MS (46.4%) was within 3% variation of PBS/MS (47.5%) and around 6% variation of PC mesh samples (49.4%), but more than 14% variation of LROS/16day (54.1%).

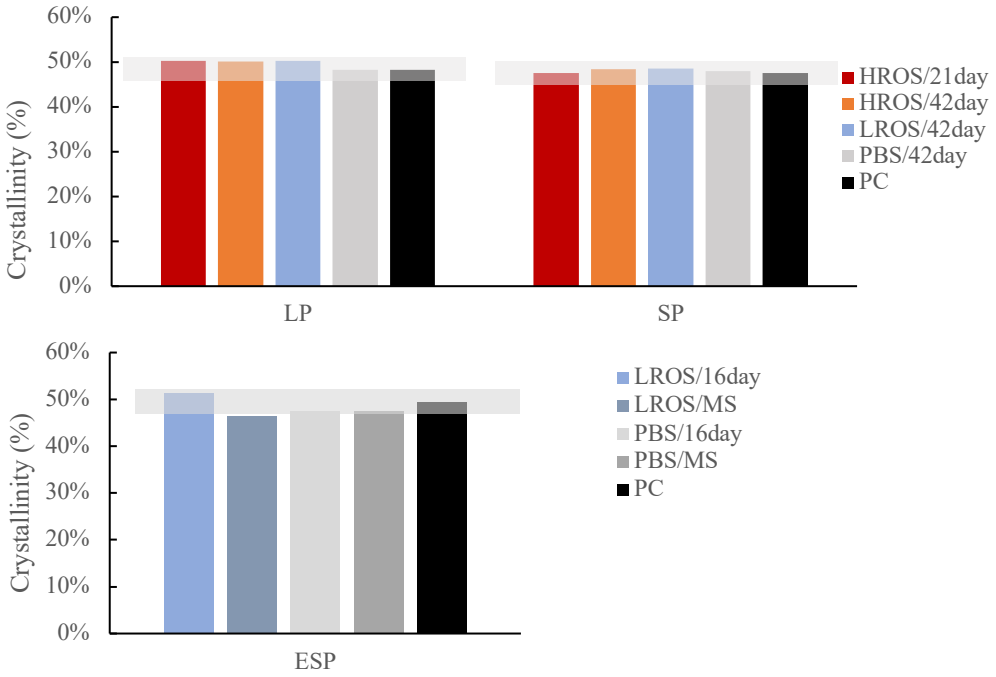

Figure 4. 8. Crystallinity results of all mesh samples in all simulated conditions. Shaded area: within 5% variation compared to PC. There was only one measured Xc for each condition.

Mechanical Testing

ROS concentration was not a factor affecting mesh biaxial stiffness (One Way ANOVA, $p > 0.05$). Biaxial stiffness for both LP and SP mesh samples in conditions of HROS/21day, HROS/42day, LROS/42day and PBS/42day was not significantly different from stiffness for PC mesh samples (One Way ANOVA, $p > 0.05$) (Figure 4.9).

There was a trend for decreased stiffness for ESP mesh exposed to ROS with or without mechanical strains (Figure 4.9). S_y of LROS/MS (97.9 ± 1.8 N/cm) was 10%

lower compared to PC mesh samples (108.2 ± 12.4 N/cm). The S_x of LROS/MS (97.9 ± 1.8 N/cm) was 10% lower than LROS/16day (104.2 ± 4.2 N/cm) and 10% lower than PBS/MS (108.9 N/cm) and the S_y of LROS/MS (177.8 ± 4.3 N/cm) was 2% lower than LROS/16day (180.7 ± 2.9 N/cm) and 14% lower than PBS/MS (212.6 N/cm) and. Biaxial stiffness for ESP mesh samples in condition of LROS/16day and PBS/16day was not significantly different from PC mesh samples (One Way ANOVA, $p > 0.05$), confirming stable mesh stiffness in case of ROS at 50 °C.

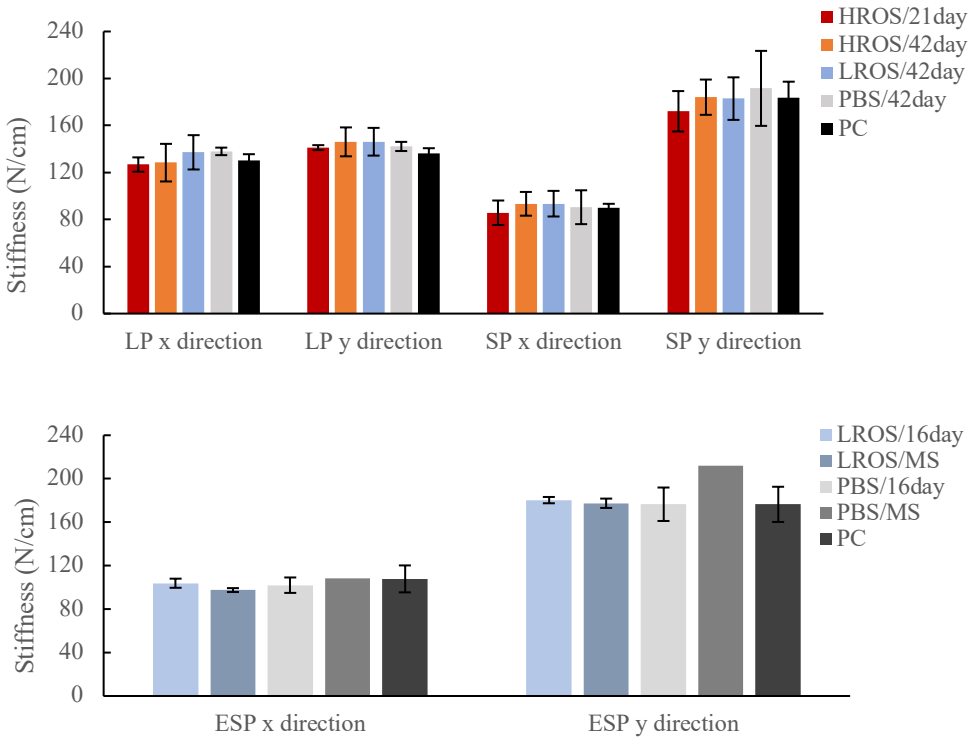

Figure 4. 9. Stiffness results of all mesh samples in all simulated conditions. There was only one measured stiffness for PBS/MS condition.

Discussion

In this study, PP mesh material changes after exposed to different ROS concentrations were compared and the synergistic effect of ROS and mechanical strains

on PP material changes was estimated. PP mesh changes in surface appearance, oxidation, crystallinity, and stiffness were not related with higher ROS concentrations. The synergistic effect of ROS and mechanical strains was not related with greater PP mesh changes in surface appearance, oxidation, crystallinity and stiffness compared to either mechanism alone. The unexpected results were likely due to lower reactive oxygen radicals on the PP mesh surface, low depth of surface oxidation, amorphous region recrystallization, relatively low mechanical strains and insufficient degradation time.

It was suspected that lower reactive oxygen radicals on the PP surface in simulated high ROS solutions limited the PP mesh oxidation. PP oxidation was initiated by hydroxyl radicals and reacted with soluble oxygen to create hydroperoxide radicals, which reacted with C–H bond in PP backbone to form hydroperoxide (–COOH), leading to PP chain scission (26). The reactive hydroxyl radicals and oxygen were created by Haber-Weiss reaction of H_2O_2 and $CoCl_2$ (26, 28). The constant 0.05M $CoCl_2$ was used for high and low ROS solution to avoid decreased oxygen solubility caused by increased $CoCl_2$ due to the salting out effect (35). Although the original solubility of oxygen was the same for both high and low ROS solutions, 6.52 M H_2O_2 reacted more actively than 1.63 M H_2O_2, releasing heat that decreased the oxygen solubility. Without enough oxygen, it can be difficult to create hydroperoxide radicals and the oxidation process was terminated.

There were contradictory results of decreased PP stiffness and increased crystallinity for mesh exposed to ROS and increased PP stiffness and decreased crystallinity for mesh exposed to mechanical strains in the study of the synergistic effect.

One possible explanation is the recrystallization of small fractions and low depth of oxidation on PP mesh surface (28, 36). PP mechanical properties were influenced by the amount of and the orientation of crystalline regions. When PP oxidation due to chain scission occurred in the amorphous region with short chains, the recrystallization of the short chains led to increased crystallinity (36). When chain scission occurred in both amorphous and crystalline regions, there were no changes observed for mesh crystallinity. However, when the recrystallized regions were not along the PP fiber direction, PP stiffness was decreased. The depth of surface oxidation on PP mesh induced by $H_2O_2/CoCl_2$ was controlled by the diffusion rate, concentrations of hydroxyl radicals and oxygen, and duration (28, 37). It was possible that the experimental duration in this study was not long enough to create deep surface cracks for propagating into bulk degradation to achieve both decreased crystallinity and stiffness.

The small mechanical strains (~5%) and short degradation times used for the synergistic effect study were unable to generate greater PP degradation than each factor alone. Previous studies report a synergistic effect on poly (etherurethane urea) or polyurethane degradation within 2 weeks of applied strains up to 300% ~ 400% (25, 27). In the current synergistic effect study, the applied mechanical strains were maintained by air pressure at 1.6 ± 0.2 psi to generate a membrane stiffness within a physiological stiffness range (29). The resulting 5% mechanical strains induced tension in the PP mesh up to 3 N/cm, lower than the estimated static load of 7.5 N/cm for implanted hernia mesh (1). Previous studies also observed a synergistic effect of PLGA degradation with applied

strains up to 0.1% after 5 weeks (38). The degradation duration in the current study was only 16 days, considerably shorter than 5 weeks (26).

An experimental protocol for *in vitro* study of the synergistic effect of ROS and biaxial mechanical strains was developed and validated by these preliminary results. In future studies, it is recommended that the simulated ROS solution concentration should be 1.63 M H_2O_2/ 0.05 M $CoCl_2$ (25) and the recommended mechanical strains should be at least 10% for ESP mesh samples to simulate the static load of 7.5 N/cm for implanted hernia mesh (1). This may not be possible using the current design of the abdominal wall simulator and alternative approaches should be considered. The recommended incubation time for the system is at least 5 weeks before material characterization (26, 38).

Conclusion

A preliminary experimental protocol for *in vitro* simulation of the synergistic effect of ROS and biaxial mechanical strains was developed. The initial simulation did not lead to greater changes in surface appearance, oxidation, crystallinity and stiffness for PP mesh exposed to both mechanisms compared to either mechanism alone. Compared to hernia meshes, implanted pelvic meshes are exposed to higher tension. Additional studies are recommended using increased mechanical strains and longer incubation to further explore these synergistic mechanisms that potentially contribute to the failure of pelvic meshes.

References

1. Taylor D. The failure of polypropylene surgical mesh *in vivo*. J Mech Behav Biomed Mater. 2018;88:370-6.

2. Thames SF, White JB, Ong KL. The myth: *in vivo* degradation of polypropylene-based meshes. Int Urogynecol J. 2017;28(2):285-97.

3. Thompson M, Guelcher S, Bendavid R, Iakovlev V, Ostergard DR. *In vivo* polypropylene mesh degradation is hardly a myth. Int Urogynecol J. 2017;28(2):333-5.

4. Iakovlev VV, Guelcher SA, Bendavid R. Degradation of polypropylene *in vivo*: A microscopic analysis of meshes explanted from patients. J Biomed Mater Res B. 2017;105(2):237-48.

5. Gil D. Naturally derived anti-inflammatory and antibacterial coatings for surgical implants [dissertation]. ProQuest Dissertations Publishing; 2017.

6. Anderson JM, Rodriguez A, Chang DT. Foreign body reaction to biomaterials. Semin Immunol. 2008;20(2):86-100.

7. Bardon J, Lukaszewicz A, Faivre V, Huot B, Payen D. Reactive oxygen species measure for rapid detection of infection in fluids. Ann. Intensive Care. 2016;6(1):1-8.

8. Schoen FJ, Lemons JE, Ratner BD, Hoffman AS. Biomaterials science: an introduction to materials in medicine. Burlington: Academic Press; 2013.

9. Cobb WS, Burns JM, Kercher KW, Matthews BD, James Norton H, Todd Heniford B. Normal intraabdominal pressure in healthy adults. J Surg Res. 2005;129(2):231-5.

10. Maurer MM, Röhrnbauer B, Feola A, Deprest J, Mazza E. Mechanical biocompatibility of prosthetic meshes: A comprehensive protocol for mechanical characterization. J Mech Behav Biomed. 2014;40:42-58.

11. Weyhe D, Cobb W, Lecuivre J, Alves A, Ladet S, Lomanto D, Bayon Y. Large pore size and controlled mesh elongation are relevant predictors for mesh integration quality and low shrinkage--Systematic analysis of key parameters of meshes in a novel minipig hernia model. Int J Surg. 2015;22:46-53.

12. Klinge U, Klosterhalfen B, Müller M, Ottinger AP, Schumpelick V. Shrinking of polypropylene mesh *in vivo*: an experimental study in dogs. Eur J Surg. 1998;164(12):965-9.

13. Kuehnert N, Kraemer NA, Otto J, Donker HCW, Slabu I, Baumann M, Kuhl CK, Klinge U. *In vivo* MRI visualization of mesh shrinkage using surgical implants loaded with superparamagnetic iron oxides. Surg Endosc. 2011;26(5):1468-75.

14. Lowham AS, Filipi CJ, Fitzgibbons R J, Stoppa R, Wantz GE, Felix EL, Crafton WB. Mechanisms of hernia recurrence after preperitoneal mesh repair. Traditional and laparoscopic. Ann Surg. 1997;225(4):422-31.

15. Klinge U, Otto J, Mühl T. High structural stability of textile implants prevents pore collapse and preserves effective porosity at strain. Biomed Res. Int. 2015;2015:1-7.

16. Conze J, Junge K, Weiß C, Anurov M, Oettinger A, Klinge U, Schumpelick V. New polymer for intra-abdominal meshes - PVDF copolymer. J Biomed Mater Res B. 2008;87(2):321-8.

17. Klinge U, Klosterhalfen B, Birkenhauer V, Junge K, Conze J, Schumpelick V. Impact of polymer pore size on the interface scar formation in a rat model. J Surg Res. 2002;103(2):208-14.

18. Wee J, Zhao Y, Choi B. Observation and modeling of environmental stress cracking behaviors of high crystalline polypropylene due to scent oils. Polym Test. 2015;48:206-14.

19. Wood AJ, Cozad MJ, Grant DA, Ostdiek AM, Bachman SL, Grant SA. Materials characterization and histological analysis of explanted polypropylene, PTFE, and PET hernia meshes from an individual patient. J Mater Sci Mater Med. 2013;24(4):1113-22.

20. Ostergard DR. Degradation, infection and heat effects on polypropylene mesh for pelvic implantation: what was known and when it was known. Int Urogynecol J. 2011;22(7):771-4.

21. Rynkevic R, Martins P, Pereira F, Ramião N, Fernandes AA. *In vitro* study of the mechanical performance of hernia mesh under cyclic loading. J Mater Sci Mater Med. 2017;28(11):1-7.

22. Mazza E, Ehret AE. Mechanical biocompatibility of highly deformable biomedical materials. J Mech Behav Biomed. 2015;48:100-24.

23. Costello CR, Bachman SL, Grant SA, Cleveland DS, Loy TS, Ramshaw BJ. Characterization of heavyweight and lightweight polypropylene prosthetic mesh explants from a single patient. Surg Innov. 2007;14(3):168-76.

24. Costello CR, Bachman SL, Ramshaw BJ, Grant SA. Materials characterization of explanted polypropylene hernia meshes. J Biomed Mater Res B. 2007;83B(1):44-9.

25. Zhao Q, Casas-Bejar J, Urbanski P, Stokes K. Glass Wool–H2O2/CoCl2 test system for *in vitro* evaluation of biodegradative stress cracking in polyurethane elastomers. J Biomed Mater Res. 1995;29(4):467-75.

26. Talley AD, Rogers BR, Iakovlev V, Dunn RF, Guelcher SA. Oxidation and degradation of polypropylene transvaginal mesh. Biomater. Sci Polym Ed. 2017;28(5):444-58.

27. Schubert MA, Wiggins MJ, Anderson JM, Hiltner A. The effect of strain state on the biostability of a poly(etherurethane urea) elastomer. J Biomed Mater Res. 1997;35(3):319-29.

28. Schubert MA, Wiggins MJ, Anderson JM, Hiltner A. Role of oxygen in biodegradation of poly(etherurethane urea) elastomers. J Biomed Mater Res. 1997;34(4):519-30.

29. Stanford MM. Mechanical characterization of the mesh-tissue composite using abdominal wall tissue phantoms and experimental simulation. ProQuest Dissertations Publishing; 2018.

30. Santos M, Tavares G, Gasperi G, Bau G. Mechanical evaluation of the resistance of elastic bands. Braz J Phys Ther. 2009;13(6):521-6.

31. Gil D, Rex J, Reukov V, Vertegel A. *In vitro* study on the deterioration of polypropylene hernia repair meshes. J Biomed Mater Res B. 2018;106(6):2225-34.

32. Deeken CR, Thompson J,Dominic M., Castile RM, Lake SP. Biaxial analysis of synthetic scaffolds for hernia repair demonstrates variability in mechanical anisotropy, non-linearity and hysteresis. J Mech Behav Biomed. 2014;38:6-16.

33. Eaton C, Lu X, Jallepalli R, Harman M. Characterization of Anisotropic Behavior and Biaxial Strain Distribution in Polymeric Surgical Mesh. BMES Annual Meeting. 2019 October.

34. Serbetci K, Kulacoglu H, Devay AO, Hasirci N. Effects of reserialization on mechanical properties of polypropylene meshes. Am. J. Surg. 2007;194(3):375-9.

35. Lang W, Zander R. Salting-out of oxygen from aqueous electrolyte solutions: prediction and measurement. Ind. Eng. Chem. Fundam. 1986;25(4):775-82.

36. Alariqi SAS, Kumar AP, Rao BSM, Singh RP. Effect of γ-dose rate on crystallinity and morphological changes of γ-sterilized biomedical polypropylene. Polym Degrad Stab. 2009;94(2):272-7.

37. Cunliffe AV, Davis A. Photo-oxidation of thick polymer samples—Part II: The influence of oxygen diffusion on the natural and artificial weathering of polyolefins. Polym. Degrad. Stab. 1982;4(1):17-37.

38. Guo M, Chu Z, Yao J, Feng W, Wang Y, Wang L, Fan Y. The effects of tensile stress on degradation of biodegradable PLGA membranes: A quantitative study. Polym Degrad Stab. 2016;124:95-100.

CHAPTER FIVE

SURFACE MODIFICATION OF POLYPROPYLENE SURGICAL MESHES FOR IMPROVING ADHESION WITH POLOXAMINE HYDROGEL ADHESIVE

Introduction

Polypropylene (PP) is commonly used as sutures and grafts, such as surgical mesh, due to its long-term structural stability and low tissue response (1). In hernia repair, PP meshes are usually fixed to abdominal tissue by sutures, staples, tacks or tissue adhesive, such as fibrin glue and synthetic adhesive (2, 3). Tissue adhesive has notable clinical benefits compared with other methods (3). However, fibrin glue has inadequate tensile and adhesive strengths compared to sutures or synthetic adhesives (4). In contrast, synthetic adhesives have mechanical properties suitable for repairing defects in tissues exposed to high tensile loads, such as the bladder and abdominal wall (4-9).

Thermosensitive hydrogels are widely used in commercially available medical products, including drug delivery systems, wound dressings, and tissue engineering scaffolds (10-12). They can be fabricated from a variety of common polymers that provide beneficial properties such as biodegradation, flexibility, and fast gelation (12). In the present study, a bifunctional poloxamine hydrogel adhesive that consists of a modified four-arm poly (propylene oxide)-poly (ethylene oxide) (PPO-PEO) block polymer and a thiol crosslinker was selected for testing (7, 8). This hydrogel-based tissue adhesive was previously shown to exhibit adhesive strength that exceeds 70 kPa via mechanical interdigitation and covalent bond formation with tissue amines (7-9). However, when this hydrogel adhesive was tested with different types of PP mesh, the

adhesive strength ranged from 10 kPa to 61 kPa (13), which was lower than the adhesive strength for collagen tissues (7). It was speculated that the adhesive strength was limited by the hydrophobicity of PP monofilaments and lack of covalent bond formation (13). Thus, we hypothesized that surface modifications of PP mesh with introduction of serum proteins might improve the adhesive strength by achieving covalent bonds.

Two surface modification techniques have potential for this application. A common surface modification for PP is protein adsorption achieved through hydrophobic and van der Waals interactions (14). In this manner, hydrophobic regions in the proteins and the PP surfaces interact, which leaves the hydrophilic regions away from the PP surface, and it is suspected that the non-polar surface chemistry of PP monofilament will lead to the poor protein adhesion. Another surface modification technique involves grafting permanent covalent functional groups onto materials to form a protein coating (15, 16). Poly-glycidyl methacrylate (PGMA), which contains an epoxy group in each repeating unit, can be used as an anchoring layer for grafting on the surface of medical devices (15, 17, 18). The PP surfaces of mesh can be activated with plasma to provide radicals and these radicals react with water, forming functional groups for depositing the PGMA layer. The PGMA layer has epoxy functionalities that reacts with human serum albumin (HSA) to form a three-dimensional plastic albumin.

The purpose of the current study was to use two different surface modifications of PP mesh to improve the adhesive strength between poloxamine hydrogel adhesive and PP mesh by achieving both mechanical interlock and covalent bonds. It was hypothesized that the adhesive strength between the poloxamine hydrogel adhesive and modified PP

mesh is stronger than the adhesive strength between the poloxamine hydrogel adhesive and unmodified PP mesh.

Materials and Surface Modification

Mesh Samples

Two commercially available heavyweight (HW) (Bard® Composix® Kugel® Hernia Patch and lightweight (LW) (Bard Composix L/P Mesh, Davol Inc, Warwick, RI, USA) warp knitted meshes were selected (Table 5.1) (19-21). The LW mesh has large pore size to facilitate tissue ingrowth and incorporation. The meshes were composed of two layers: PP warp knitted mesh structure and submicron e-PTFE membrane. PP for surgical mesh is a hydrophobic material with desirable properties of flexibility, chemical resistance and thermal stability. The e-PTFE membrane acts as a barrier layer to minimize the tissue adherence to PP mesh. Since the tissue adhesive is only applied between the PP mesh side and the abdominal wall tissue during surgery, the e-PTFE layers were removed and only the PP meshes were investigated in this study (6, 22, 23). Sample meshes were cut at dimension of 1 cm × 3 cm, to match the aluminum holders used for lap shear testing (ASTM F2255-05).

Table 5. 1. Polypropylene mesh information and surface modification techniques

Mesh Type	Classification	Structure	Weight [g/m^2]	Thickness [mm]	Porosity	Surface Modification
HW	Standard Class III	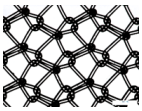	95	0.57	Area: 57% Weight: 83%	PGMA/HSA grafting BSA adsorption None
LW	Light Class III		41	0.48	Area: 64% Weight: 90%	PGMA/HSA grafting BSA adsorption None

Bifunctional Poloxamine Hydrogel Adhesive

Two polymers used for bifunctional poloxamine hydrogel adhesive were synthesized from Tetronic® 1107 (T1107, molecular weight: 15k Da, HLB:18-23) (BASF corporation, Florham Park, NJ) following the published methods (7-9). The polymers were acrylated T1107 and acrylated T1107 with the addition of N-hydroxysuccinimide (NHS). The acrylation (ACR) process was used to chemically crosslink the polymer within the hydrogel and the NHS process facilitated binding to the tissue amines (8). In the ACR process, the hydroxyl groups at the end of each four arms of T1107 were reacted with acryloyl chloride (Sigma-Aldrich) to form T1107-ACR with acrylate end groups (Figure 5.1). In the NHS process, the NHS groups (Sigma-Aldrich, St. Lois, MO, USA) were added to partially acrylated T1107 with 50% acrylation to form T1107-ACR-NHS (Figure 5.1). The composition of T1107-ACR and T1107-ACR-NHS was assessed by Proton NMR in d-chloroform.

The bifunctional poloxamine hydrogel solution was made with the final concentration of 30 wt% mixture of 75 wt% T1107-ACR (ACR conversion: 92%) and 25 wt% T1107-ACR-NHS (ACR conversion: 30%). The bifunctional poloxamine hydrogel adhesive was processed by crosslinking the hydrogel mixture with dithiothreitol (DTT) (Across Organics, NJ, USA). This thiol donor crosslinker, was added using the process of Michel-Type addition reaction in 1x Phosphate Buffer Saline (9). The molar ratio of thiol to acrylate in this adhesive solution was 1:1. Tetronic® 1107 is thermosensitive in water. The thermal gelation temperature of poloxamine hydrogel adhesive was at room temperature (7). When the concentration and/or the temperature is above its critical

micellar concentration and critical micellar temperature, the aqueous solution becomes a hydrogel. Therefore, this bifunctional poloxamine hydrogel adhesive was kept at 4 °C before use.

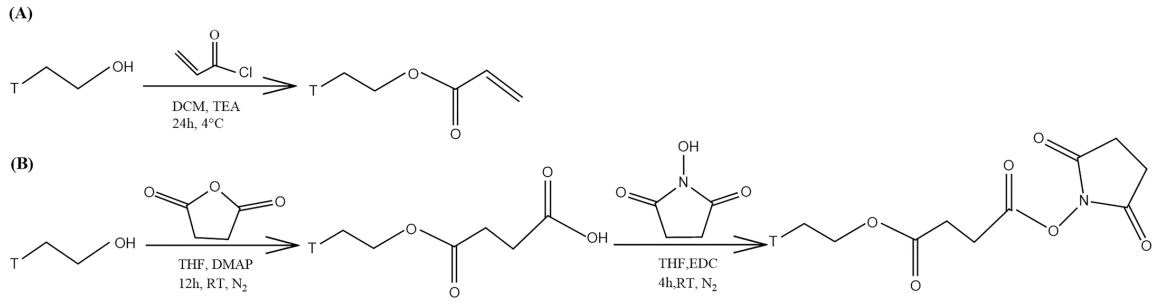

Figure 5. 1. Tetronic® T1107 (A) acrylation reaction (B) N- hydroxysuccinimide (NHS) reaction.
T: Tetronic® T1107, DCM: Dichloromethane (HPLC grade), TEA: trimethylamine, THF: tetrahydrofuran, DMAP: 4-dimethylaminopyridine, EDC: 1-(3-dimethylaminopropyl)-3-ethylcarbodiimide hydrochloride (9).

Surface Modification

PP for surgical mesh is a hydrophobic material with low surface energy and lack of functional groups, which makes it difficult to strongly adhere layered coatings of another material. Two surface modification methods (BSA adsorption and PGMA/HSA grafting) were compared in this study. The BSA adsorption involved immersing PP meshes in 5% (w/v) bovine serum albumin (BSA) (Sigma-Aldrich) (PH = 7.4) in PBS buffer at 37°C for 30 minutes (14, 24). Samples were air dried at room temperature before applying poloxamine hydrogel adhesive. The PGMA/HSA grafting involved fabrication of an albumin coating (15) (Figure 5.2a). Mesh samples were treated under plasma for 10 minutes at 700 V DC, 15mA DC, 10.5 W (Plasma Cleaner / Sterilizer, Harrick, Pleasantville, NY) followed by soaking in water for 30 minutes to activate the

PP surface with hydroxyl, carboxylic acid and nitric oxide functional groups. After 30 minutes, samples were oven dried (~80 °C) and purged under nitrogen until fully dried. Plasma treated PP mesh samples were dip coated (Meyer Fientechnik, Gottingen, Germany; D-3400) in 0.5% (w/v) PGMA (Mn= 176000g/mol) in chloroform at the speed of 300 mm/min. PGMA modified samples were annealed at 120 °C for 10 minutes followed by dip coating in 3% (w/v) human serum albumin (HSA) (Sigma-Aldrich corp., St. Louis, MO; CAS # 7024-90-7) solution in phosphate buffer for 2 hours. The PGMA/HSA grafted samples were dried for 12 hours and followed by annealing for 2 hours at 120 °C. Unmodified PP meshes (HW & LW) were used as control groups (Table 5.1).

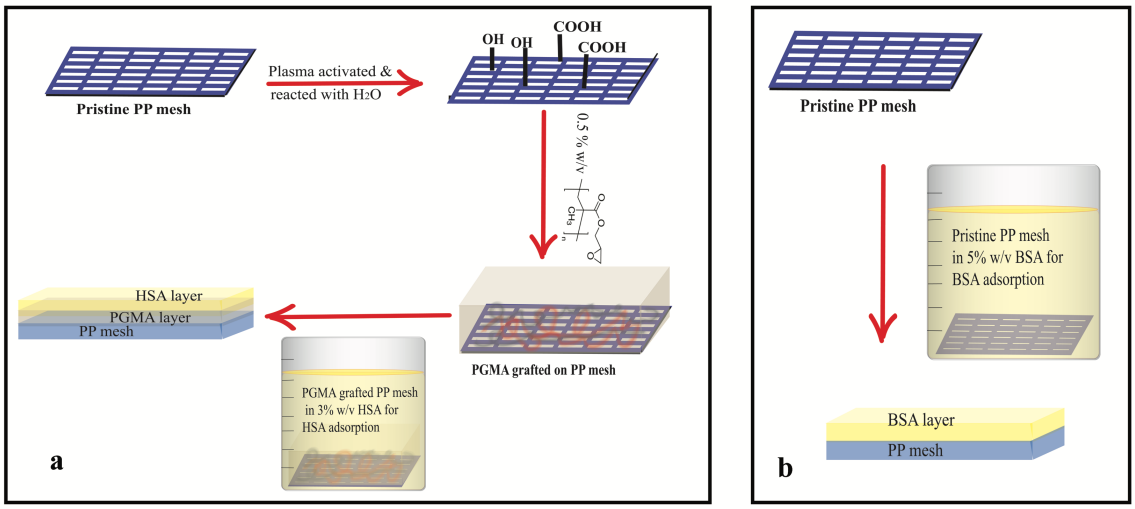

Figure 5. 2. Schematic diagram for surface modification methods. a. PGMA/HSA surface modification method. Modified mesh samples were annealed at 120 °C. b. BSA surface modification.

Testing Methods

Thermo-gravimetric analysis (TGA)

Unmodified LW and HW mesh samples were analyzed for thermal stability using TGA (TGA Q5000 V3.17 Build 265, TA Instruments, New Castle, DE) with a ramp rate of 10 °C/min from 25 °C to 600 °C in nitrogen gas. Samples were equilibrated at room temperature under nitrogen purge for 10 min prior to heating.

Infrared Spectroscopy (FTIR)

The bonding strength between BSA on the BSA modified PP and between the PGMA and HSA on the PGMA/HSA modified PP surface was confirmed by ATR-FTIR analysis (Nicolet Magna 550 FTIR spectrometer equipped with a SpectraTech Endurance Foundation Series Diamond ATR, Thermo, Waltham, MA). Unmodified PP filaments from unmodified meshes were used as control groups. Prior to FTIR, the BSA modified PP and PGMA/HSA modified PP were rinsed in ultrapure water. In order to remove any HSA that was not covalently bonded to the PGMA, the PGMA/HSA modified samples were washed by immersing in phosphate buffer at 37°C and pH7.4 on an orbital shaker for 24 hours.

Contact Angle

Static water contact angle of BSA modified, PGMA/HSA modified, and unmodified meshes was measured using optical contact angle goniometer (DSA-20E, FM40Mk2 EasyDrop, Krüss, Germany) to measure the hydrophilicity of the samples. In a controlled environment (humidity: 35%, temperature: 25.4 °C), droplets of water (2.0 µl) (n = 5) were placed on the edge of meshes. Although the software could automatically

measure the contact angle, the mesh knitting structures led to uneven surface, which decreased the accuracy of the automatic contact angle result. The final contact angle was measured manually using Image J (National Institutes of Health).

Lap Shear Testing

Adhesive strength, defined as the peak load under uniaxial lap shear testing divided by the contact area between the mesh and adhesive, was measured consistent with ASTM F2255-05 completed at 37°C using a 100 N load cell (Synergie 100, MTS, Eden Prairie, MN) at a 10 mm/min loading rate. The testing specimen was formed by two pieces of 1cm × 3cm aluminum holders adhered with collagen sheets (as tissue layers) and PP meshes (n=5 each), separately. A 60 µl volume of poloxamine hydrogel adhesive was applied over a 1cm × 1cm contact area between the mesh and collagen surface (Figure 5.3). The curing time for hydrogel adhesive was 1 hour. Samples were covered by a cloth containing PBS to maintain moisture. Test groups included BSA modified mesh, PGMA/HSA modified mesh, and unmodified meshes and tissue layers as controls.

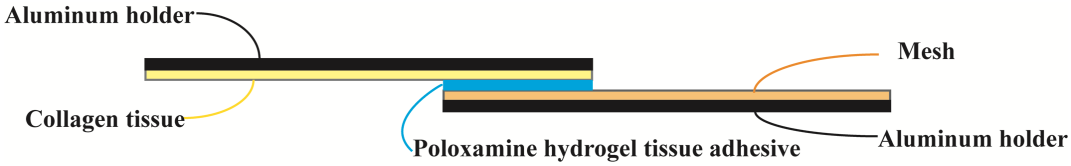

Figure 5. 3. Specimen for lap shear testing.

Optical Microscope Images of Mesh Surface before and after Lap Shear Testing

Individual mesh surfaces before and after lap shear testing were observed under a stereo optical microscope (SMZ-168, Motic, Richmond, Canada) with an attached digital camera (Infinity 2, Lumenera, Ottawa, Canada). Images were captured under 12 x with

0.243 pixel/cm at dimension of 1392 × 1040 with light projecting from bottom. Meshes modified with PGMA/HSA were investigated and unmodified meshes were used as control groups.

Statistical Analyses

The effect of mesh type (LW, HW) and surface modification method (BSA adsorption, PGMA/HSA grafting, unmodified) on adhesive strength was compared with two-way analysis of variance (ANOVA) (α=0.05). The differences between the surface modification techniques and individual mesh types were identified by Tukey's post-hoc multiple comparisons (α=0.05). The effect of surface modification (PGMA/HSA grafting and unmodified) on contact angle was compared with paired t-test (α=0.05). The statistical analyses used OriginLab 9.0 (Northampton, Massachusetts, USA).

Results

TGA

The thermal stability of the LW and HW PP meshes was well above the 120 °C annealing temperature used in the PGMA/HSA grafting process, with similar behavior for both mesh types (Figure 5.4).

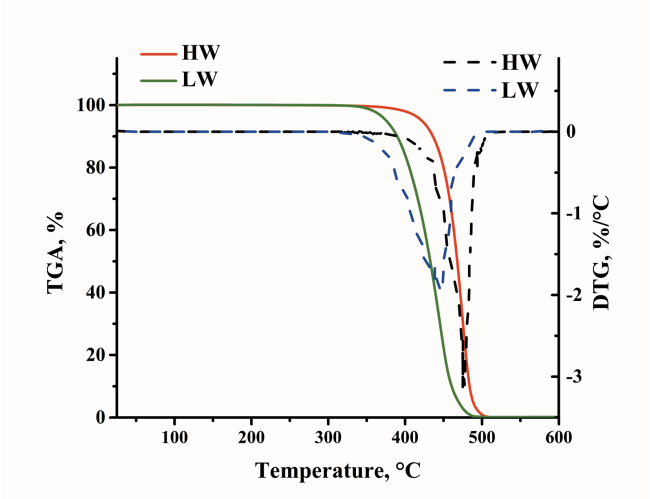

Figure 5. 4. The weight loss (TGA curves, mass %) and the rate of weight loss (derivative thermogravimetry curves (DTG), mass %/°C) of unmodified HW and LW meshes. Green solid line: TGA curve for lightweight mesh, red solid line: TGA curve for heavyweight mesh, blue dashed line: DTG curve for lightweight mesh, black dashed line: DTG curve for heavyweight mesh.

FTIR

Chemical bonding between the albumin and PP was confirmed with FTIR, with PGMA/HSA successfully grafted onto the PP monofilament (Table 5.2). For PP mesh modified by BSA adsorption, the BSA was easily removed during routine rinsing, demonstrating poor protein adhesion on the PP monofilaments. This loss of BSA was confirmed by FTIR spectra having only a weak absorbance signal between 3300–3500 cm^{-1} and around 1600 cm^{-1} (Figure 5.5). In contrast, the epoxy groups in PGMA assisted HSA protein adhesion to the PP. The presence of PGMA is evident by absorbance around 1730 cm^{-1} (stretching of C=O groups) (25). The conversion of epoxy groups in PGMA is evident by the decrease of absorbance around 910 cm^{-1}. The presence of HSA is evident by absorbance at 1541 cm^{-1} (amide II C–H stretching and N–H bending), around 1653 cm^{-1} (bending of N–H groups) and absorbance from 3300–3500 cm^{-1} (stretching of amide

A N–H groups), which was not observed in unmodified PP (26-30). There was no difference in wave number peaks comparing before and after washing in phosphate buffer (Figure 5.6).

Table 5. 2. Functional groups in FTIR wavelength

Bond	Wavenumber (cm^{-1})	References
PP		
C–H_3 and –CH_2–	2990 – 2850	(13)
	1380 – 1370	
	1475 – 1450	
	1465 – 1440	
PGMA		
C=O	1530 – 1830	(22, 27)
C–O	1240,1270	
C–O–C stretching	1189, 1141	
Albumin		
Amide A NH stretching	3300	(24-26)
Amide I band	1600 – 1700	
β sheet	1610 – 1640	
random coil	1640 – 1650	
α helix	1650 – 1658	
β-turn structure	1660 – 1700	
Amide II band	1500 – 1600	
Amide II CH stretching and NH bending	1541	

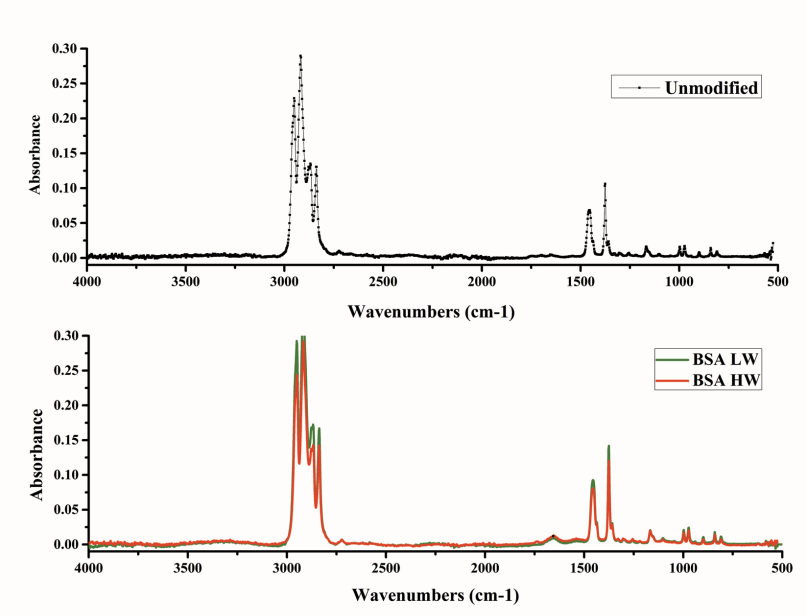

Figure 5. 5. FTIR spectra of heavyweight and lightweight meshes modified by BSA.

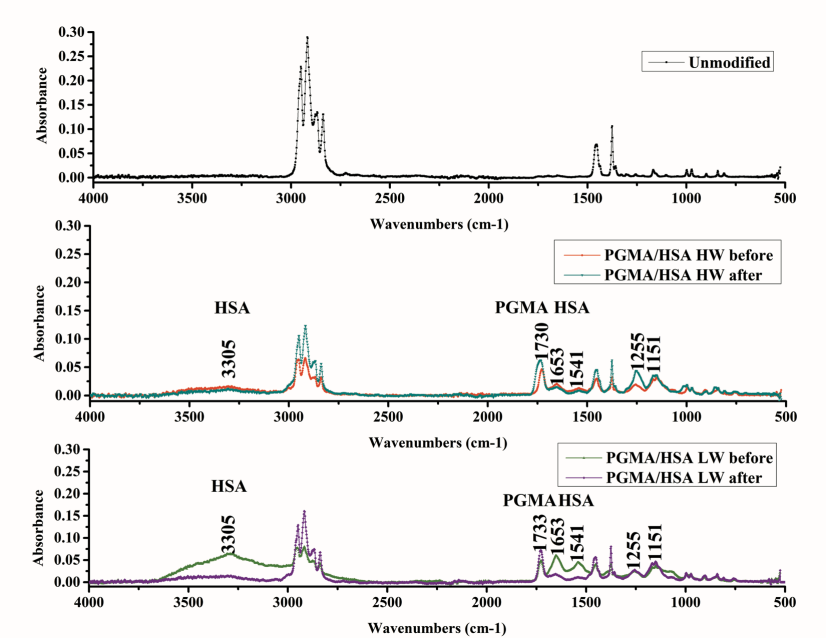

Figure 5. 6. FTIR spectra of unmodified mesh, heavyweight, and lightweight meshes modified by PGMA/HSA before and after phosphate buffer washing.

Contact Angle

The hydrophilicity of meshes after surface modification was unchanged compared to unmodified meshes. The values of contact angles were larger than 110° for all types of meshes, consistent with the hydrophobic properties of the PP monofilaments (Figure 5.7). The meshes modified by PGMA/HSA (113 ± 6.02° for lightweight mesh and 129 ± 5.16° for heavyweight mesh) had smaller contact angles than unmodified meshes (128 ± 9.14° for lightweight mesh and 138 ± 9.01° for heavyweight mesh). However, the difference was not statistically significant (paired t-test, $\alpha = 0.05$).

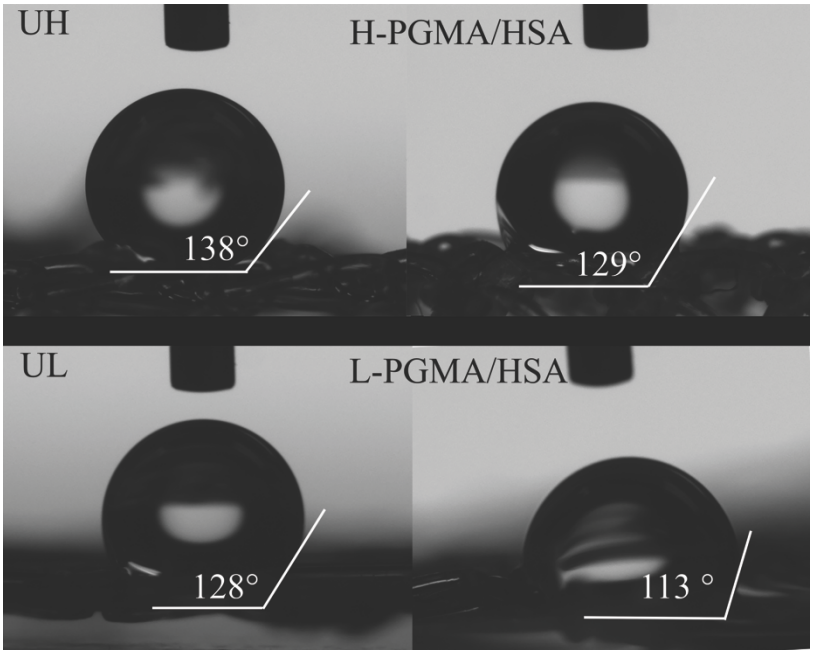

Figure 5. 7. Contact angle images of heavyweight and lightweight meshes before and after PGMA/HSA modification.
U: unmodified, H: heavyweight, L: lightweight
Paired t-test of contact angle before and after surface coating: $p = 0.05$.

Lap Shear Testing

The PGMA/HSA surface modification improved the adhesive strength for HW and LW meshes attached with poloxamine hydrogel tissue adhesive compared to unmodified meshes (Figure 5.8, Table 5.3). Mesh type was not a factor affecting the adhesive strength (two-way ANOVA, $p = 0.075$), but surface modification significantly affected the adhesive strength (two-way ANOVA, $p < 0.01$). The adhesive strength between unmodified meshes (44.95 ± 20.16 kPa for heavyweight mesh, 21.69 ± 8.642 kPa for lightweight mesh) and tissue layers was significantly lower than tissue layers alone (Tukey, $p < 0.05$). The adhesive strength of meshes modified by PGMA/HSA (69.63 ± 30.93 kPa for heavyweight mesh, 65.25 ± 16.30 kPa for lightweight mesh) was

significantly higher compared to unmodified meshes and meshes modified by BSA (Tukey, $p < 0.05$) and equivalent to tissue layers alone (Tukey, $p > 0.05$). Therefore, the PGMA/HSA surface modification significantly improved the adhesive strength for meshes attached with poloxamine hydrogel tissue adhesive.

Table 5. 3. Statistical analysis of lap shear testing strength with factors of mesh type and surface modification method

Adhesive strength (kPa)		**Surface Modification**	**Collagen**	**Unmodified**	**BSA**	**PGMA/HSA**
Collagen	66.59 ± 25.26	Collagen	--	*	*	p > 0.05
UH	44.95 ± 20.16	Unmodified		--	*	*
UL	21.69 ± 8.642					
H-BSA	13.29 ± 4.378	BSA			--	*
L-BSA	4.053 ± 0.8463					
H-PGMA/HSA	69.63 ± 30.93	PGMA/HSA				--
L-PGMA/HSA	65.25 ± 16.30					

*: Tukey's post-hoc, $p < 0.05$

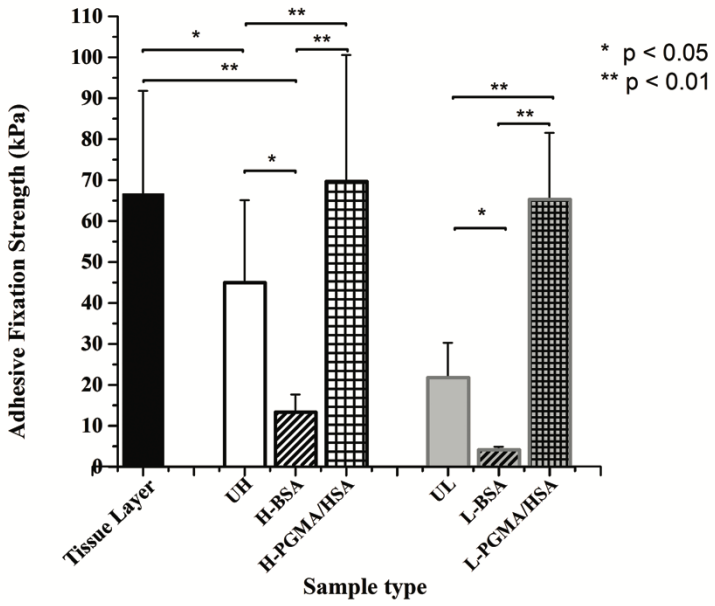

Figure 5. 8. Adhesive strength between mesh and tissue under uniaxial lap shear testing. UH: unmodified heavyweight mesh, UL: unmodified lightweight mesh, H-BSA: heavyweight mesh modified by BSA, L-BSA: lightweight mesh modified by BSA, H-PGMA/HSA: heavyweight mesh modified by PGMA/HSA, L-PGMA/HSA: lightweight mesh modified by PGMA/HSA.

Discussion

This study evaluated two surface modification techniques (BSA adsorption and PGMA/HSA grafting) applied to PP mesh to improve the adhesive strength when attached to tissues using poloxamine hydrogel adhesive. The PGMA/HSA surface modification significantly improved the adhesive strength for meshes attached with poloxamine hydrogel tissue adhesive compared to unmodified meshes and meshes modified by BSA adsorption. The improved adhesive strength was achieved through mechanical interlock of the hydrogel tissue adhesive into the PP mesh pores and chemical bonding of the albumin after successful PGMA/HSA grafting onto the PP monofilament.

Surface modifications of PP surgical mesh, including biologic coating materials such as gelatin, purified collagen and extracellular matrix, are commonly pursued to improve various mesh properties (21, 30-33). The coating should be applied on PP monofilament as a monolayer rather than allowing it to be trapped in mesh pores. A pore size of > 1 mm should be maintained to avoid scar plate formation on mesh instead of tissue ingrowth (34, 35). The spontaneous driving force during coating PP mesh without any other interactions is van der Waals force, which leads to inadequate coating stability. In previous studies, TiMesh light, a PP mesh coated with 30-50 nm hydrophilic titanium coating, tended to achieve better adhesion to tissue without further fixation than other polypropylene mesh (36). In contrast, the adhesive fixation strength of TiMesh with bioadhesive glue was lower than other polypropylene meshes with similar or larger pore size. This may be caused by a weaker interaction between polypropylene and titanium coating than the chemical bonds between titanium coating and the bioadhesive. In our

study, the fixation strength with poloxamine hydrogel adhesive for BSA- modified PP mesh was also lower than unmodified PP mesh. In aqueous solutions, the core of the protein is hydrophobic, whereas the outer edges are hydrophilic. Therefore, the BSA coating was mainly adsorbed onto the PP surface through van der Waals interaction. However, these interactions are notably weak, and adsorbed proteins can be separated from the PP surface when the interaction strength between the hydrophilic regions and the surrounding environment is larger than the hydrophobic and van der Waals interactions.

Key aspects of the PGMA/HSA surface modification provided for strong chemical bonds between the PGMA/HSA coating and the PP surface and helped to prevent disruption of the coating during lap shear testing. In fact, Luzinov et al. (17, 37-43) and others (44-47) clearly demonstrated that PGMA reacts with polymeric surfaces treated by air plasma and that proteins are readily reacting with epoxy groups of PGMA via amino and carboxyl functionalities. For instance, it was demonstrated using XPS that after enzymatic (protease) removal of fibrinogen or bovine serum albumin layers anchored to PGMA significant amount of amino acids remain grafted to the PGMA layer (37). During the surface modification process, the PGMA layer was first strongly chemically bonded through epoxy groups on the plasma activated PP surface. Further chemical bonds were formed between amino and carboxyl groups in albumin and remaining epoxy groups in PGMA, as confirmed by FTIR. The results from the current study support previous research using plasma treatment to improve the adhesion of functional groups and PGMA grafting to achieve strong covalent bonding between

hydrophobic PP mesh surfaces and the hydrophilic coatings (26, 30). Gorgieva, et al. activated PP mesh with O_2 plasma to create functional groups on the PP surface, which further formed covalent bonds with a hydrophilic gelatin containing an antimicrobial-active agent while maintaining the mesh structural and mechanical properties (30). The PGMA/HSA surface modification in the current study involved a "grafting to" method, with PGMA providing a uniform and homogeneous macromolecular anchoring layer (polymer brushes) for grafting polymers or proteins (e.g. HSA) to the PP surface (15-17). The PGMA epoxy groups are relatively stable at elevated temperature, which allowed for heat annealing and denaturation of HSA at 120 °C. PGMA polymer layers also can be deposited on various polymers, such as polyethylene terephthalate (PET), polyethylene (PE), PP, polyvinylidene fluoride (PVDF) and nylon (17).

Adequate adhesive strength for PP mesh fixation is critical for repairing defects in abdominal wall tissues that are exposed to high tensile loads. Adhesive strength should reach the maximum tensile strength of the abdominal wall of 11 N/cm - 27 N/cm and the maximum intra-abdominal pressure of 22.8 kPa in healthy adults (36, 48). Using the approach of Schug-Pass, et al. and assuming a defect size of approximately 1 cm^2 area, an abdominal pressure of 22.8 kPa would generate a force of approximately 2.28 N over the defect area (36). The necessary adhesive strength to resist this physiological force can be calculated by dividing by the contact area between the mesh and adhesive. In the current study, an area of 1 cm^2 adhesive resulted in peak loads of 6.5-7 N during lap shear testing of meshes modified by PGMA/HSA (Figure 5.8), exceeding the maximum physiological levels. The mode of failure for this hydrogel adhesive is adhesive failure, caused by

detachment between adhesive and tissue (8). However, when the adhesive strength between adhesive and mesh is lower than that between adhesive and tissue, detachment occurs between adhesive and mesh. The large pores of PGMA/HSA modified samples after lap shear testing were filled with much more poloxamine hydrogel tissue adhesive than unmodified mesh (Figure 5.9) confirming strong chemical bonding and mechanical interlock are formed between PGMA/HSA modified mesh samples and hydrogel adhesive.

In previous studies, fibrin glue or semi-synthetic adhesives have met the above physiological requirements, but have used much larger areas of adhesive on the mesh surface (6, 26, 36). For example, an area of 134 cm^2 of fibrin glue was used to achieve a 4.6-7.2 kPa adhesive strength for lightweight meshes in a ball burst set-up (36), which is below the 65 kPa average adhesive strength of LW meshes modified by PGMA/HSA in the current study (Figure 5.8). Moreover, the high viscosity of semi-synthetic adhesives prevents application over a large contact area during laparoscopic surgery (6). Synthetic cyanoacrylates adhesives have the advantages of fast fixation and adequate adhesive strength for hernia repair (4, 5), but *in vitro* cytotoxicity due to formaldehyde release and *in vivo* tissue toxicity have been reported (49).

It is recognized that the nature of the abdominal wall affects the mechanical behavior of implanted surgical meshes in biaxial directions. A limitation of this study is that only uniaxial lap shear testing was used to assess adhesive strength. This method was selected because it is a common, highly repeatable method for generating adhesive strength results that are comparable to previous studies of this poloxamine hydrogel

adhesive (7-9). Moreover, existing biaxial testing procedures (e.g. ball burst test, clamp-needle set-up) are insufficient for predicting the *in vivo* three-dimensional behavior of mesh. The ball burst test assumes uniform distribution of tension throughout all fibers within the mesh. However, the knitted structure of surgical mesh always behaves anisotropically (50, 51). Another limitation is the use of collagen to represent the tissue layer, which does not fully capture the complex biological aspects of the abdominal wall. In future studies, *in vivo* applications of PGMA/HSA modified PP mesh and hydrogel adhesive will be explored to characterize adhesion to tissues and any potential negative effects.

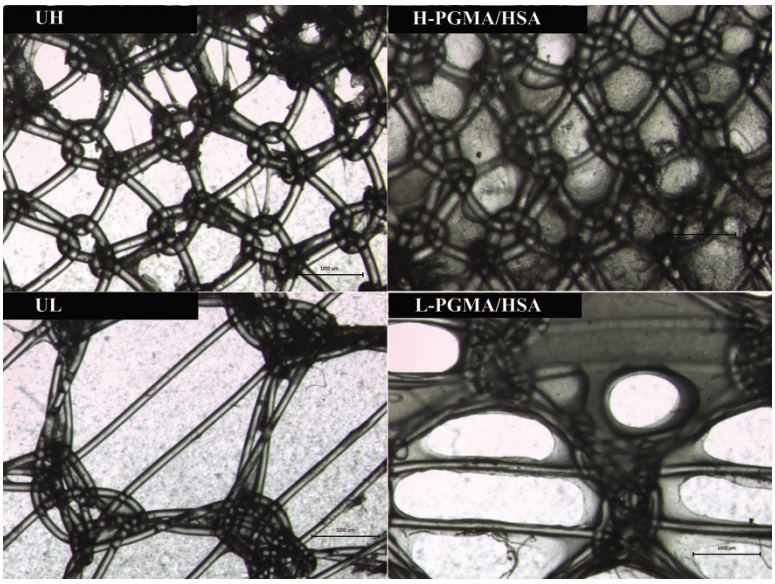

Figure 5. 9. Hydrogel tissue adhesive residue on unmodified and PGMA/HSA modified mesh samples after lap shear testing.
Unmodified mesh with minimal attached adhesive had pores without residue (bright white) and modified mesh with attached adhesive had pores with residue (gray). U: unmodified, L: lightweight mesh, H: heavyweight mesh.

Conclusion

In this study, successful PGMA/HSA grafting on PP mesh significantly improved adhesive strength with poloxamine hydrogel tissue adhesive compared to unmodified meshes and meshes modified by BSA adsorption. The experimental maximum adhesive strength for PGMA/HSA modified mesh was approximately 2 times higher than that of unmodified mesh, which was achieved by mechanical interlock of the hydrogel tissue adhesive into the PP mesh pores and chemical bonding of the grafted HSA. The application of PGMA/HSA grafting and hydrogel tissue adhesive would benefit both surgeons and patients in hernia mesh fixation in laparoscopic surgery. It provides for easy surgical handling due to fast gelation at body temperature and high adhesive strength, with the potential for reducing patient pain due to elimination of tissue penetrating using sutures or staples for mesh fixation.

References

1. Pruitt LA, Chakravartula AM. Mechanics of biomaterials: fundamental principles for implant design. New York: Cambridge University Press; 2011: 120-121.

2. Sajid MS, Ladwa N, Kalra L, McFall M, Baig MK, Sains P. A meta-analysis examining the use of tacker mesh fixation versus glue mesh fixation in laparoscopic inguinal hernia repair. Am. J. Surgery. 2013;206(1):103-111.

3. Shah NS, Fullwood C, Siriwardena AK, Sheen AJ. Mesh fixation at laparoscopic inguinal hernia repair: a meta-analysis comparing tissue glue and tack fixation. World J. of Surg. 2014;38(10):2558-2570.

4. Marcovich R, Williams AL, Rubin MA, Wolf JS Jr. Comparison of 2-octyl cyanoacrylate adhesive, fibrin glue, and suturing for wound closure in the porcine urinary tract. Urology. 2001;57(4):806-810.

5. Dilege E, Deveci U, Erbil Y, Dinççа A, Seven R, Ozarmagan S, Mercan S, Barbaros U. N-butyl cyanoacrylate versus conventional suturing for fixation of meshes in an incisional hernia model. J Invest Surg. 2010;23(5):262-266.

6. Schug-Pass C, Jacob DA, Rittinghausen J, Lippert H, Kockerling F. Biomechanical properties of (semi-) synthetic glues for mesh fixation in endoscopic inguinal hernia repair. Hernia. 2013;17(6):773-7.

7. Sanders LK. Development and characterization of a novel hydrogel adhesive for soft tissue applications. ProQuest Dissertations Publishing; 2015.

8. Sanders L, Stone R, Webb K, Mefford T, Nagatomi J. Mechanical characterization of a bifunctional tetronic hydrogel adhesive for soft tissues. J Biomed Mater Res A 2015;103(3):861-868.

9. Alejos MF. Controlling thermal gelation properties of novel tetronic® hydrogel-based tissue adhesive. All Theses. 2016;2492.

10. Fan Z, Xu Z, Niu H, Gao N, Guan Y, Li C, Dang Y, Cui X, Liu LX, Duan Y, Li H, Zhou X, Lin P, Ma J, Guan J. An injectable oxygen release system to augment cell survival and promote cardiac repair following myocardial infarction. Sci. Rep. 2018; 8:1-22.

11. Fan Z, Fu M, Xu Z, Zhang B, Li Z, Li H, Zhou X, Liu X, Duan Y, Lin PH, Duann P, Xie X, Ma J, Liu Z, Guan J. Sustained release of a peptide-based matrix metalloproteinase-2 inhibitor to attenuate adverse cardiac remodeling and improve cardiac function following myocardial infarction. Biomacromolecules. 2017 09/11;18(9):2820-9.

12. Caló E, Khutoryanskiy VV. Biomedical applications of hydrogels: A review of patents and commercial products. Eur Polym J. 2015 April 2015; 65:252-67.

13. Lu X, Alejos M, Nagatomi J, Harman MK. Mechanical characterization of a novel bifunctional Tetronic® hydrogel adhesive for surgical mesh fixation. Presented at 2017 Annu Mtg SFB; Minneapolis, MN. April 4-8, 2017.

14. Michel SA, Knetsch ML, Koole LH. Adsorption of albumin on flax fibers increases endothelial cell adhesion and blood compatibility *in vitro*. J Biomater Sci Polym Ed. 2014;25(7):698-712.

15. Whatley BR, Wen X, Luzinov I, Sharma S, inventors; Protein Based Materials, Plastic Albumin Devices and Related Methods. US20130325121 A1. 2013 May 30.

16. Goli K, Rojas O, Ozcam A, Genzer J. Generation of functional coatings on hydrophobic surfaces through deposition of denatured proteins followed by grafting from polymerization. Biomacromolecules. 2012;13(5):1371-82.

17. Zdyrko B, Luzinov I. Polymer brushes by the “grafting to” method. Macromol. Rapid Commun. 2011;32(12):859-69.

18. Khanna A, Luzinov I, Burtovvy R, Simionescu A, Langan III EM, Laberge M. Fabrication of Human Serum Albumin films for enhanced hemocompatibility and VascularCompatibility. Presented at 39th Annu Mtg SFB; Charlotte, NC. April 15-18, 2015.

19. Coda A, Lamberti R, Martorana S. Classification of prosthetics used in hernia repair based on weight and biomaterial. Hernia. 2012;16(1):9-20.

20. Klinge U, Klosterhalfen B. Modified classification of surgical meshes for hernia repair based on the analyses of 1,000 explanted meshes. Hernia. 2012;16(3):251-258.

21. Soares BM, Guidoin RG, Marois Y, Martin L, King MW, Laroche G, et al. *In vivo* characterization of a fluoropassivated gelatin-impregnated polyester mesh for hernia repair. J Biomed Mater Res. 1996;32(3):293-305.

22. Schug-Pass C, Jacob DA, Lippert H, Köckerling F. Differences in biomechanical stability using various fibrin glue compositions for mesh fixation in endoscopic inguinal hernia repair. Surg Endosc. 2012;26(11):3282-3286.

23. Schug-Pass C, Lippert H, Köckerling F. Fixation of mesh to the peritoneum using fibrin glue: investigations with a biomechanical model and an experimental laparoscopic porcine model. Surg Endosc. 2009;23(12):2809–2815

24. Grafahrend D, Calvet JL, Klinkhammer K, Salber J, Dalton PD, Möller M, Klee D. Control of protein adsorption on functionalized electrospun fibers. Biotechnol Bioeng. 2008;101(3):609-621.

25. Liu Y, Hu W, Lu Z, Li CM. Photografted poly(methyl methacrylate)-based high performance protein microarray for hepatitis B virus biomarker detection in human serum. Med Chem Comm. 2010;1(2):132-135.

26. Blackman BRK, Guild FJ. Forced air plasma treatment for enhanced adhesion of polypropylene and polyethylene. J Adhes Sci Technol. 2013 12/15;27(24):2714-2726.

27. Raza M, Jiang Y, Wei Y, Ahmad A, Khan A, Qipeng Y. Insights from spectroscopic and in-silico techniques for the exploitation of biomolecular interactions between human serum albumin and paromomycin. Colloids Surf. B. 2017; 157:242-253.

28. Sekar G, Sugumar S, Mukherjee A, Chandrasekaran N. Multiple spectroscopic studies of the structural conformational changes of human serum albumin—Essential oil based nanoemulsions conjugates. JOL.2015;161:187-197.

29. Tang J, Luan F, Chen X. Binding analysis of glycyrrhetinic acid to human serum albumin: Fluorescence spectroscopy, FTIR, and molecular modeling. Bioorganic Med. Chem. 2006;14(9):3210-3217.

30. Gorgieva S, Modic M, Dovgan B, Kaisersberger-Vincek M, Kokol V. Plasma-activated polypropylene mesh-gelatin scaffold composite as potential implant for bioactive hernia treatment. Plasma Process Polym. 2015;12(3):237-251.

31. Wolf MT, Carruthers CA, Dearth CL, Crapo PM, Huber A, Burnsed OA, Londono R, Johnson SA, Daly KA, Stahl EC, Freund JM, Medberry CJ, Carey LE, Nieponice A, Amoroso NJ, Badylak SF. Polypropylene surgical mesh coated with extracellular matrix mitigates the host foreign body response. J Biomed Mater Res A. 2014;102(1):234-246.

32. Riet Mv, Burger JWA, Bonthuis F, Jeekel J, Bonjer HJ. Prevention of adhesion formation to polypropylene mesh by collagen coating: A randomized controlled study in a rat model of ventral hernia repair. Surg Endosc. 2004;18(4):681-685.

33. Poussier M, Denève E, Blanc P, Boulay E, Bertrand M, Nedelcu M, Herrero A, Fabre JM, Nocca D. A review of available prosthetic material for abdominal wall repair. J Visc Surg. 2013 2;150(1):52-59.

34. Junge K, Binnebösel M, von Trotha KT, Rosch R, Klinge U, P. Neumann U, Lynen Jansen P. Mesh biocompatibility: effects of cellular inflammation and tissue remodelling. Langenbeck's Arch. Surg. 2012;397(2):255-270.

35. Klinge U, Klosterhalfen B, Birkenhauer V, Junge K, Conze J, Schumpelick V. Impact of polymer pore size on the interface scar formation in a rat model. J Surg Res. 2002;103(2):208-214.

36. Schug-Pass C, Lippert H, Köckerling F. Mesh fixation with fibrin glue (Tissucol/Tisseel®) in hernia repair dependent on the mesh structure—is there an optimum fibrin–mesh combination—Investigations on a biomechanical model. Langenbeck's Arch. Surg. 2010;395(5):569-574.

37. Zdyrko B, Hoy O, Luzinov I. Toward protein imprinting with polymer brushes. Biointerphases. 2009, 4 (2), FA17-FA21.

38. Kroning A, Furchner A, Aulich D, Bittrich E, Rauch S, Uhlmann P, Eichhorn KJ, Seeber M, Luzinov I, Kilbey SM, Lokitz BS, Minko S, Hinrichs K. In situ infrared

ellipsometry for protein adsorption studies on ultrathin smart polymer brushes in aqueous environment. ACS Appl Mater Interfaces. 2015, 7 (23), 12430-12439.

39. Zdyrko B, Hoy O, Kinnan M. K, Chumanov G, Luzinov I. Nano-patterning with polymer brushes via solvent-assisted polymer grafting. Soft Matter. 2008, 4 (11), 2213-2219.

40. Burtovyy O, Klep V, Chen H. C, Hu R. K, Lin C. C, Luzinov, I. Hydrophobic modification of polymer surfaces via "grafting to" approach. J Macromol Sci B. 2007, 46 (1), 137-154.

41.Singh N, Husson S. M, Zdyrko B, Luzinov I. Surface modification of microporous PVDF membranes by ATRP. J Memb Sci. 2005, 262 (1-2), 81-90.

42. Burtovyy O, Klep V, Turel T, Gowayed Y, Luzinov I. Polymeric membranes: surface modification by “grafting to” method and fabrication of multilayered assemblies, in Nanoscience and Nanotechnology for Chemical and Biological Defense, Editors: Nagarajan, R, Zukas, W, Hatton, T. A, Lee, S. ACS Symposium Series 1016, Washington DC: 2009; p 289-305.

43. Luzinov I. A, Swaminatha Iyer K. L, Klep V. Z, Zdyrko B. V. Surface modification of substrates, US patent 7026014 B2, Apr. 11, 2006.

44. Zemanova I, Turkova J, Capka M, Nakhapetyan L. A, Svec F, Kalal J. Effect of the nature of proteins on their coupling to different epoxide-containing supports. Enzyme Microb Tech. 1981, 3 (3), 229-232.

45. Turkova J, Blaha K, Malanikova M, Vancurova D, Svec F, Kalal J. Methacrylate gels with epoxide groups as supports for immobilization of enzymes in pH range 3-12. Biochim. Biophys. Acta. 1978, 524 (1), 162-169.

46. Drobnik J, Vlasak J, Pilar J, Svec F, Kalal J. Synthetic model polymers in the study of protein immobilization on glycidyl methacrylate carriers. Enzyme Microb Tech. 1979, 1 (2), 107-112.

47. Kalal, J. Epoxy and aldehyde polymers as reagents. J. Polym. Sci., Polym. Symp. 1978, (62), 251-270.

48. Cobb WS, Burns JM, Kercher KW, Matthews BD, James NH, Heniford BT. Normal Intraabdominal Pressure in Healthy Adults. J Surg Res. 2005 12;129(2):231-235.

49. Pascual G, Sotomayor S, Rodríguez M, Pérez-Köhler B, Kühnhardt A, Fernández-Gutiérrez M, San Román J, Bellón JM. Cytotoxicity of cyanoacrylate-based tissue

adhesives and short-term preclinical *in vivo* biocompatibility in abdominal hernia repair. PLoS One. 2016;11(6): e0157920.

50. Hernández-Gascón B, Peña E, Melero H, Pascual G, Doblaré M, Ginebra MP, Bellón JM, Calvo B. Mechanical behaviour of synthetic surgical meshes: Finite element simulation of the herniated abdominal wall. Acta Biomater. 2011;7(11):3905-3913.

51. Hernández-Gascón B, Peña E, Pascual G, Rodríguez M, Bellón JM, Calvo B. Long-term anisotropic mechanical response of surgical meshes used to repair abdominal wall defects. J Mech Behav Biomed Mater. 2012;5(1):257-271.

CHAPTER SIX

CONCLUSIONS AND RECOMMENDATIONS FOR FUTURE STUDIES

The broad objective of this dissertation was to explore mechanisms of material changes in polymeric mesh implants after *in vivo* exposure using experimental characterization and biological assessments. This objective was addressed through completion of three aims by exploring specific mechanisms that potentially contribute to material changes after *in vivo* exposure using mesh explants (Aim 1) and *in vitro* simulation (Aim 2), and developing a new technology combining two patented technologies that improved clinical outcomes of hernia mesh fixation (Aim 3). Chapters 2 and 3 addressed Aim 1, Chapter 4 addressed Aim 2, and Chapter 5 addressed Aim 3.

Aim 1. Determine material changes of polymeric mesh explants and explore the mechanisms of material changes related to clinical factors

Aim 1 was accomplished by comparing material properties of PP mesh explants to mesh implants before implantation to explore the impact of physiological function on potential degradation mechanisms of PP mesh related to clinical factors. Chapter 2 compared pore size of explanted mesh to pristine mesh and related it to the pore pattern using a photogrammetric method. The photogrammetric method was developed using image capture, image processing and image analysis to classify pore pattern, measure pore size and evaluate changes in pore size after physiological loading. Chapter 3 analyzed explanted PP mesh changes in surface chemistry, crystallinity and stiffness after mesh samples were sufficiently cleaned, and investigated clinical characteristics (i.e. mesh class, mesh placement location, patients' infection record) that might trigger the

material changes consistent with PP degradation using analysis of multivariate associations.

Recognizing pore pattern and the observed reduction in pore size in explanted meshes after supported *in vivo* reports of mesh shrinkage (1, 2). In general, smaller pores tend to remain unchanged whereas larger pores become smaller in explanted meshes compared with pristine control meshes. The photogrammetric technique developed in Chapter 2 used a simple light microscopy set-up and automated detection of pores, supporting efficient pore detection, providing for direct measurement of pore size area, minimizing human errors and avoiding errors when a symmetrical pore shape was assumed for a mesh with complicated pore shapes (3, 4).

Evaluating explanted PP mesh material changes and their associations with clinical characteristics was important to explore potential mechanisms for PP mesh degradation when exposed to mechanical contraction or an oxidizing environment (5). The findings in Chapter 3 supported that infection (oxidizing environment) was a factor affecting stiffness changes and mesh class (pore size) was a factor affecting crystallinity changes when compared to pristine mesh, consistent with other *in vitro* and *in vivo* studies (6-8). Material changes were not associated with other clinical characteristics and the observed changes did not contribute to gross mesh failure. The universal application of significant findings in Chapter 3 was limited by the highly variable nature of implant retrieval analysis without controlled clinical and surgical factors for patient selection (9) and the small number of infection cases. The insignificant results were challenged by the

limited documentation of mesh selection at index surgery and it was unknown whether the PP mesh had absorbable components or fibers containing antioxidants.

In future studies, there is a need for direct measurement of *in vivo* ROS (10) and *in vivo* mechanical strains (11) on mesh to help precisely establish the correlation between those factors and mesh degradation mechanisms. The direct measurement can be fulfilled using a controlled animal study with known mesh characteristics, such as antioxidants to modify ROS effects or absorbable components to modify mesh strains. Different from meshes implanted in the abdomen, pelvic floor surgical meshes are exposed to higher tension and have relatively greater risk of exposure to bacteria from the local environment (12), resulting in higher mechanical strains and accumulation of ROS due to the bacterial adherence. In a controlled animal study, different ROS concentrations and mechanical strain levels could be accomplished by implanting meshes in abdominal and pelvic locations. The findings in the controlled animal study can be used to estimate mesh degradation of hernia mesh explants and pelvic mesh explants removed from patients.

Aim 2. Determine the effect of simulated oxidizing agents and applied mechanical strains on initiating polypropylene mesh degradation

Aim 2 was accomplished by establishing the correlation between direct measurement of ROS and mesh degradation and estimating the synergistic impact of ROS and mechanical strains on PP mesh degradation, as evidenced by changes in surface appearance, oxidation, crystallinity, and stiffness using *in vitro* simulation. Chapter 4 compared the PP mesh degradation induced by higher ROS concentrations to low ROS

concentrations and compared the PP mesh degradation induced by the synergistic effect of ROS and mechanical strains to either mechanism alone.

The findings in Chapter 4 confirmed the simulated ROS solutions made of 1.63 M H_2O_2/ 0.05 M $CoCl_2$ induced PP material changes (13) compared to higher ROS concentration. A preliminary experimental protocol for *in vitro* simulation of synergistic effect of ROS and biaxial mechanical strains was developed in Chapter 4. The simulation results rejected the hypothesis that the synergistic effect of oxidizing agents and mechanical strains significantly induced PP mesh degradation than the individual factors alone, which were likely due to low depth of surface oxidation and amorphous region recrystallization in case of inadequate mechanical strains and short degradation time.

In future studies, there is a need to validate the simulation for synergistic effect of ROS and mechanical strains on PP mesh degradation and quantify the biaxial mechanical strains inducing PP mesh degradation. The simulation for synergistic effect can be validated using degradable materials requiring low applied mechanical strains (smaller than 5%) to induce material degradation. Different from degradable polymer materials, PP mesh is difficult to degrade under small mechanical strains (12, 14). The mechanical strains to initiate PP mesh degradation can be quantified using a biaxial tensile testing machine with adequate load cells. For a 2 cm × 2cm biaxial testing mesh sample, 100 N load cells are required to reach the estimated biaxial fatigue loads of 36.3 N/cm (12). A longer degradation duration, at least 5 weeks, should help to initiate PP mesh degradation (15, 16).

Aim 3. Determine the effect of surface modification of polymeric mesh implants on fixation and compatibility with a hydrogel adhesive

Aim 3 was accomplished by comparing BSA adsorption and PGMA/HAS grafting of PP mesh to improve the adhesive strength with poloxamine hydrogel adhesive.

The successful PGMA/HSA grafting onto PP monofilament in Chapter 5 significantly improved adhesive strength through mechanical interlock of the hydrogel tissue adhesive into the PP mesh pores and chemical bonding of the albumin, compared to unmodified meshes and meshes modified by BSA adsorption. The maximum adhesive strength was up to 65–70 kPa for meshes modified by PGMA/HSA, compared to 4–13 kPa for meshes modified by BSA, and 22–45 kPa for unmodified meshes using an area of 1 cm^2 adhesive. These results confirm the strong chemical bonds between the PGMA/HSA coating and the PP surface and helped to prevent disruption of the coating during lap shear testing (17).

In future studies, there is a need for *in vivo* applications of PGMA/HSA modified PP mesh and hydrogel adhesive to characterize adhesion to tissues and any potential negative effects. Furthermore, there is a potential to apply the combined PGMA/HSA surface modification technique and hydrogel adhesive in other biomedical applications, such as “bio-adhesive biomaterial fixation system” in orthopedic applications, peripheral nerve regeneration and more.

References

1. Coda A, Bendavid R, Botto-Micca F, Bossotti M, Bona A. Structural alterations of prosthetic meshes in humans. Hernia. 2003;7(1):29-34.

2. Harsløf S, Zinther N, Harsløf T, Danielsen C, Wara P, Friis-Andersen H. Mesh shrinkage depends on mesh properties and anchoring device: an experimental long-term study in sheep. Hernia. 2017;21(1):107-13.

3. Miao L, Wang F, Wang L, Zou T, Brochu G, Guidoin R. Physical characteristics of medical textile prostheses designed for hernia repair: a comprehensive analysis of select commercial devices. Materials. 2015;8(12):8148-68.

4. Mühl T, Binnebösel M, Klinge U, Goedderz T. New objective measurement to characterize the porosity of textile implants. J Biomed Mater Res B. 2008;84B(1):176-83.

5. Currier BH, Van Citters DW, Currier JH, Carlson EM, Tibbo ME, Collier JP. *In vivo* oxidation in retrieved highly crosslinked tibial inserts. J Biomed Mater Res B. 2013;101B(3):441-8.

6. Gil D, Rex J, Reukov V, Vertegel A. *In vitro* study on the deterioration of polypropylene hernia repair meshes. J Biomed Mater Res B. 2018;106(6):2225-34.

7. Afonso JS, Jorge R, Martins PS, Soldi MD, Alves OL, Patricio B, Mascarenhas T, Sartori MG, Girao MJ. Structural and thermal properties of polypropylene mesh used in treatment of stress urinary incontinence. Acta Bioeng Biomech. 2009;11(3):27-33.

8. Costello CR, Bachman SL, Ramshaw BJ, Grant SA. Materials characterization of explanted polypropylene hernia meshes. J Biomed Mater Res B. 2007;83B(1):44-9.

9. Gajjar CR, King MW, Guidoin R. Biotextiles as medical implants: 8 - Retrieval studies for medical biotextiles. Woodhead Publishing; 2013. p. 182-210.

10. Bardon J, Lukaszewicz A, Faivre V, Huot B, Payen D. Reactive oxygen species measure for rapid detection of infection in fluids. Ann. Intensive Care. 2016;6(1):1-8.

11. Kuehnert N, Kraemer NA, Otto J, Donker HCW, Slabu I, Baumann M, Kuhl CK, Klinge U. *In vivo* MRI visualization of mesh shrinkage using surgical implants loaded with superparamagnetic iron oxides. Surg Endosc. 2011;26(5):1468-75.

12. Taylor D. The failure of polypropylene surgical mesh *in vivo*. J Mech Behav Biomed Mater. 2018;88:370-6.

13. Zhao Q, Casas-Bejar J, Urbanski P, Stokes K. Glass Wool–H2O2/CoCl2 test system for *in vitro* evaluation of biodegradative stress cracking in polyurethane elastomers. J Biomed Mater Res. 1995;29(4):467-75.

14. Li X, Kruger JA, Jor JWY, Wong V, Dietz HP, Nash MP, Nielsen PM. Characterizing the ex vivo mechanical properties of synthetic polypropylene surgical mesh. J Mech Behav Biomed Mater. 2014;37:48-55.

15. Talley AD, Rogers BR, Iakovlev V, Dunn RF, Guelcher SA. Oxidation and degradation of polypropylene transvaginal mesh. Biomater. Sci Polym Ed. 2017;28(5):444-58.

16. Guo M, Chu Z, Yao J, Feng W, Wang Y, Wang L, Fan Y. The effects of tensile stress on degradation of biodegradable PLGA membranes: A quantitative study. Polym Degrad Stab. 2016;124:95-100.

17. Zdyrko B, Luzinov I. Polymer brushes by the “grafting to” method. Macromolecular Rapid Communications. 2011;32(12):859-69.

APPENDICES

Appendix A

Patient Information for Chapter 2

Table A- 1. Patient information (small pore mesh)

Mesh #	Sex (F/M)	Age at removal (years)	BMI	Implantation time (months)	Infection/ Smoker (Y/N)	Removal reason/ Recurrent hernia (Y/N)
M0004_14	M	55	40.7	13	N/N	mesh not working/Y
M0005_14	M	76	34.8	14	Y/N	infection/Y
M0010_14	F	58	24.7	42	N/N	mesh not working/Y
M0018_14	M	52	38.6	48	N/N	mesh not working/Y
M0035_14	M	59	31.8	12	N/N	mesh not working/Y
M0037_14	F	69	29.9	24	N/N	mesh not working/Y
M0039_14	M	65	35.7	60	N/N	mesh not working/Y
M0049_14	F	57	29.6	67	N/N	mesh not working/Y
M0054_14	F	67	36.6	48	N/N	mesh not working/Y
M0056_14	F	76	29.6	34	N/N	mesh not working/Y
M0063_14	M	41	27.4	5	N/N	chronic inflammation, mesh not working/Y
M0071_14	F	50	28.9	25	N/Y	mesh not working/Y
M0072_14	M	79	28.2	38	N/N	bowel obstruction; mesh not working/Y
M0077_14	M	74	23.7	10	N/N	mesh not working/Y
M0086_14	M	70	24.0	18	N/N	mesh not working/Y
M0091_14	M	34	31.6	11	N/N	incarcerated, mesh not working/Y
M0097_14	F	60	36.8	13	N/N	mesh not working/Y

Table A- 2. Patient information (large pore mesh)

Mesh #	Sex (F/M)	Age at removal (years)	BMI	Implantation time (months)	Infection/ Smoker (Y/N)	Removal reason/ Recurrent hernia (Y/N)
M0008_14	M	72	26.9	4	N/N	mesh not working/Y
M0021_14	F	82	27.3	8	N/N	infection/Y
M0038_14	M	59	29.9	6	N/N	mesh not working/Y
M0042_14	M	66	36.6	84	N/N	mesh not working/Y
M0044_14	M	73	26.8	20	N/N	mesh not working/Y
M0047_14	F	41	30.8	36	N/Y	mesh not working/Y
M0062_14	F	47	27.7	13	N/N	seroma, mesh not working/Y
M0091_14	M	34	31.6	11	N/N	incarcerated, mesh not working/Y

Appendix B

Mesh Orientation in Biaxial Tensile Testing

Table B- 1. Mesh orientation in longitudinal (y) direction and transverse (x) direction

Brand	Microscope structure	Orientation for biaxial tensile testing	Brand	Microscope structure	Orientation for biaxial tensile testing
Composix ™ E/X	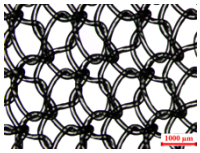	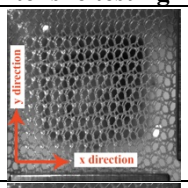	Physiomesh ™ (new structure)	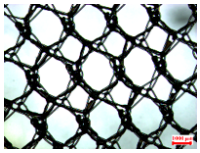	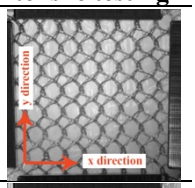
Composix ® Kugel®	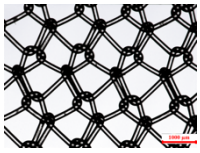	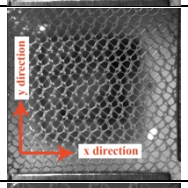	Prolene® Soft		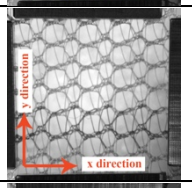
Composix ™ L/P	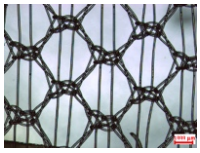	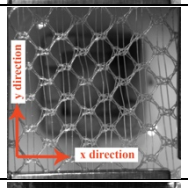	Ultrapro®	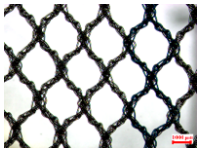	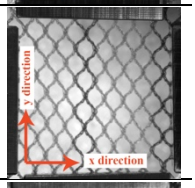
C -QUR®	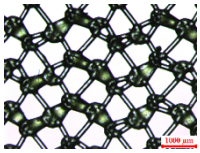	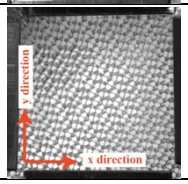	Ventralight™	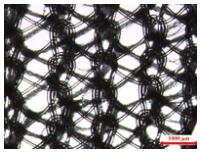	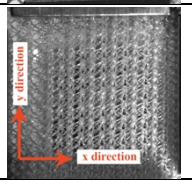

The column of mesh orientation in biaxial tensile testing corresponds to the column of microscope structures

Appendix C

Summary of Statistical Analysis for Chapter 3

Table C- 1. Statistical analysis of mesh class on degradation

Comparison	n	Statistical Test	Result	p value
$C_{Surface}$ and class	63	Cochran-Armitage	Independent	0.30
$X_{c,changed}$% and class	22, 23, 17	One Way ANOVA	Mean $_{\text{class I}}$ = (-2.5 ± 5.1)% Mean $_{\text{class II}}$ = (4.1± 6.0)% Mean $_{\text{class III}}$ = (1.8 ± 8.4)%	0.004*
$S_{x,changed}$% and class	11, 18, 6	One Way ANOVA	Mean $_{\text{x, class I}}$ = -47.4 ± 24.4% Mean $_{\text{x, class II}}$ = -38.7 ± 21.2% Mean $_{\text{x, class III}}$ = -34.9 ± 25.9%	0.49
$S_{y,changed}$% and class			Mean $_{\text{y, class I}}$ = -30.4 ± 35.7% Mean $_{\text{y, class II}}$ = -29.6 ± 19.9% Mean $_{\text{y, class III}}$ = -45.6 ± 24.5%	0.43

mesh class: class
*: $p < 0.05$

Table C- 2. Statistical analysis of patient factors on degradation

Comparison	n	Statistical Test	Result	p value
$C_{Surface}$ and sex	63	Chi square	Independent	0.53
$C_{Surface}$ and $T_{implantation}$	43, 16	Wilcoxon rank	Median $_{Y}$ = 25 Median $_{N}$ = 18	0.57
$C_{Surface}$ and age	46, 17	T test	Mean $_{Y}$ = 59 ± 12 Mean $_{N}$ = 58 ± 11	0.69
$C_{Surface}$ and BMI	46, 17	T test	Mean $_{Y}$ = 33.3 ± 6.7 Mean $_{N}$ = 34.9 ± 5.8	0.39
$X_{c,changed}$% and sex	31, 31	Wilcoxon rank	Median $_{F}$ = 1.6% Median $_{M}$ = 0.6%	0.70
$X_{c,changed}$% and $T_{implantation}$	59	Spearman	ρ = -0.17	0.21
$X_{c,changed}$% and age	62	Spearman	ρ = 0.22	0.08
$X_{c,changed}$% and BMI	62	Spearman	ρ = -0.20	0.11
$S_{x,changed}$% and sex	17, 18	T test	Mean $_{x\ direction\ F}$ = -34.6 ± 20.4% Mean $_{x\ direction\ M}$ = -16.6 ± 24.0%	0.12
$S_{y,changed}$% and sex			Mean $_{y\ direction\ F}$ = -28.9 ± 24.2% Mean $_{y\ direction\ M}$ = -36.1 ± 28.6%	0.43
$S_{x,changed}$% and $T_{implantation}$	32	Pearson	r_x = 0.14	0.44
$S_{y,changed}$% and $T_{implantation}$			r_y = -0.10	0.57
$S_{x,changed}$% and age	35	Pearson	r_x = -0.10	0.57
$S_{y,changed}$% and age			r_y = -0.17	0.33
$S_{x,changed}$% and BMI	35	Pearson	r_x = 0.25	0.15
$S_{y,changed}$% and BMI			r_y = 0.14	0.42

implantation time (months): $T_{implantation}$
age at removal (years): age

Table C- 3. Statistical analysis of medical and surgical factors on degradation

Comparison	n	Statistical Test	Result	p value
Medical factors				
$C_{Surface}$ and diabetes	62	Chi square	Independent	0.92
$C_{Surface}$ and pre_her_re	62	Fisher's exact	Independent	0.76
$C_{Surface}$ and infection	61	Fisher's exact	Independent	0.42
$C_{Surface}$ and smoking	63	Fisher's exact	Independent	0.71
$X_{c,changed}$% and diabetes	16, 45	Wilcoxon rank	Median $_{diabetes}$ = 3.3% Median $_{no\ diabetes}$ = 0.9%	0.33
$X_{c,changed}$% and pre_her_re	43, 18	Wilcoxon rank	Median $_{pre\_her\_re}$ = 2.1% Median $_{no\ pre\_her\_re}$ = -1.2%	0.33
$X_{c,changed}$% and infection	8, 52	Wilcoxon rank	Median $_{infected}$ = -1.6% Median $_{noninfected}$ = 1.5%	0.09
$X_{c,changed}$% and smoking	4, 58	Wilcoxon rank	Median $_{smoker}$ = 2.1% Median $_{nonsmoker}$ = 1.5%	0.27
$S_{x,changed}$% and diabetes	8, 26	T test	Mean $_{x,\ diabetes}$ = -37.2 ± 29.4% Mean $_{x,\ no\ diabetes}$= -41.0 ± 21.1%	0.69
$S_{y,changed}$% and diabetes			Mean $_{y,\ diabetes}$= -32.9 ± 32.6% Mean $_{y,\ no\ diabetes}$ = -32.3 ± 25.5%	0.95
$S_{x,changed}$% and pre_her_re	21, 13	T test	Mean $_{x,\ pre\_her\_re}$ = -37.9 ± 24.4% Mean $_{x,\ pre\_her\_re}$ = -43.8± 20.6%	0.47
$S_{y,changed}$% and pre_her_re			Mean $_{y,\ pre\_her\_re}$ = -31.6 ± 28.7% Mean $_{y,\ pre\_her\_re}$ = -33.8 ± 24.4%	0.82
$S_{x,changed}$% and infection	4, 30	T test	Mean $_{x,\ infection}$ = -66.7 ± 13.4% Mean $_{x,\ no\ infection}$ = -36.6 ± 21.6%	0.01*
$S_{y,changed}$% and infection			Mean $_{y,\ infection}$ = -64.9 ± 16.1% Mean $_{y,\ no\ infection}$ = -28.1 ± 25.0%	0.01*
$S_{x,changed}$% and smoking	3, 32	T test	Mean $_{x,\ smoker}$ = -40.4 ± 20.3% Mean $_{x,\ nonsmoker}$ = -40.7 ± 23.3%	0.98
$S_{y,changed}$% and smoking			Mean $_{y,\ smoker}$ = -21.5± 23.0% Mean $_{y,\ nonsmoker}$ = -33.6 ± 26.8%	0.45
Surgical factors				
$C_{Surface}$ and intra_extra	62	Fisher's exact	Independent	0.16
$X_{c,changed}$% and intra_extra	24, 37	Wilcoxon rank	Median $_{intra}$ = 2.6% Median $_{extra}$ = 0.4%	0.74
$S_{x,changed}$% and intra_extra	17, 17	T test	Mean $_{x,\ intra}$ = -36.5 ± 20.0% Mean $_{x,\ extra}$ = -43.8 ± 25.5%	0.36
$S_{y,changed}$% and intra_extra			Mean $_{y,\ intra}$ = -31.3 ± 24.6% Mean $_{y,\ extra}$ = -33.6 ± 29.5%	0.81

previous hernia repair: pre_her_re
mesh location: intra_extra
*: $p < 0.05$

Appendix D

Summary of Material Properties for Chapter 4

Table D- 1. Summary of material properties

	Prolene® Soft				Composix™ E/X			
	IR	**SEM**	**Crystallinity (%)**	**Stiffness (N/cm)**	**IR**	**SEM**	**Crystallinity (%)**	**Stiffness (N/cm)**
Different ROS Concentrations: 21 DAY								
High ROS	Y	Y	50.3%	x: 127.2 ± 6.1 y: 141.6 ± 2.1	N	N	47.6%	x: 86.2 ± 10.4 y: 172.5 ± 17.2
Different ROS Concentrations: 42 DAY								
High ROS	N	Y	50.1%	x: 128.8 ± 16.0 y: 146.5 ± 12.3	N	Y	48.4%	x: 93.8 ± 10.1 y: 184.5 ± 15.0
Low ROS	Y	Y	50.3%	x: 137. 6 ±14.6 y: 146.6 ± 11.8	Y	Y	48.6%	x: 93.9 ± 10.9 y: 183.4 ± 18.1
PBS	N	N	48.2%	x: 138.4 ± 3.2 y: 142.6 ± 3.9	N	N	48.0%	x: 90.9 ± 14.4 y: 192.0 ± 31.9
Pristine								
			48.3%	x: 130.5 ± 5.5 y: 136.8 ± 4.3			47.6%	x: 90.3 ± 3.5 y: 184.0 ± 13.7
Synergistic Effect: 16 DAY								
Low ROS					Y	Y	51.4%	x: 104.2 ± 4.2 y: 180.7 ± 2.9
Low ROS + Strain					N	Y	46.5%	x: 97.9 ± 1.8 y: 177.8 ± 4.3
PBS					N	N	47.6%	x: 102.4 ± 7.1 y: 176.9 ± 15.4
PBS + Strain					N	N	47.5%	x: 108.9 y: 212.6
Pristine								
							49.4%	x: 108.2 ± 12.4 y: 176.8 ± 16.2